Simulation of Hydraulic Stimulation: Acoustic Wave Emission in Fractured Porous Media Using Local and Global Partition-of-Unity Finite Element

By

Mohammad Komijani

A thesis

presented to the University of Waterloo

in fulfilment of the

thesis requirement for the degree of

Doctor of Philosophy

in

Civil Engineering

Waterloo, Ontario, Canada, 2018

Examining committee membership

The following served on the Examining Committee for this thesis. The decision of the Examining Committee is by majority vote.

External Examiner	Dr. Thomas-Peter Fries Professor and Head of the Institute of Structural Analysis, Graz University of Technology
Supervisor	Dr. Robert Gracie Associate Professor, Department of Civil and Environmental Engineering, University of Waterloo
Internal Member	Dr. Sriram Narasimhan Professor, Department of Civil and Environmental Engineering, University of Waterloo
Internal Member	Dr. Shunde Yin Associate Professor, Department of Civil and Environmental Engineering, University of Waterloo
Internal-external Member	Dr. Maurice Dusseault Professor, Department of Earth and Environmental Sciences, University of Waterloo

Author's declaration

I hereby declare that I am the sole author of this thesis. This is a true copy of the thesis, including any required final revisions, as accepted by my examiners.

I understand that my thesis may be made electronically available to the public.

Abstract

Hydraulic Fracturing (HF) is an effective stimulation process for extracting oil and gas from unconventional low-permeable reservoirs. The process is conducted by injecting high-pressure fluids into the ground to generate fracture networks in rock masses and stimulate natural fractures to increase the permeability of formation and extract oil and gas. Due to the multiple- and coupled-physics involved, hydraulic fracturing is a complex engineering process.

The extent of the induced fractures and stimulated volume and reactivation of natural faults and fractures are some of the practical issues associated with hydraulic fracturing. Acoustic Emission (AE) monitoring and analysis are used to probe the behaviour of solid materials in such applications. The process of elastic wave propagation induced by an abrupt local release of stored strain energy is known as acoustic, microseismic, and seismic emission (depending on the context and the magnitude of the event). These emissions can be triggered by material bifurcation-instabilities like slope slipping, fault-reactivation, pore collapsing, and cracking - processes that are all categorized as localization phenomena.

The microseismic monitoring industry attempts to relate acoustic emissions measured by geophones to the nature of the stimulated volume created during hydraulic fracturing. This process is full of uncertainties and researchers have not yet focused on both explicitly modeling the process of fracture reactivation and the accurate simulation of acoustic wave propagations resulting from the localization. The biggest gap in the modeling literature is that most of the previous works fail to accurately simulate the process of transient acoustic wave propagation through the fractured porous media following the elastic energy release. Instead of explicitly

modeling fracturing and acoustic emission, most previous studies have aimed to relate energy release to seismic moment.

To overcome some of the existing shortcomings in the numerical modeling of the coupled problem of interface localization-acoustic emission, this thesis is focused on developing new computational methods and programs for the simulation of microseismic wave emissions induced by interface slip instability in fractured porous media. As a coupled nonlinear mixed multi-physics problem, simulation of hydraulic stimulation involves several mathematical and computational complexities and difficulties in terms of modeling, stability, and convergence, such as the inf-sup stability problems that arise from mixed formulations due to the hydro-mechanical couplings and contact conditions. In AE modeling, due to the high-frequency transient nature of the problem, additional numerical problems emerging from the Gibbs phenomenon and artificial period elongation and amplitude decay are also involved.

The thesis has three main objectives. The first objective is to develop a numerical model for simulation of wave propagation in discontinuous media, which is fulfilled in Chapter 2 of the thesis. In this chapter a new enriched finite element method is developed for simulation of wave propagation in fractured media. The method combines the advantages of the global Partition-of-Unity Method (PUM) with harmonic enrichment functions via the Generalized Finite Element Method (GFEM) with the local PUM via the Phantom Node Method (PNM). The GFEM enrichments suppress the spurious oscillations that can appear in regular Finite Element Method (FEM) analysis of dynamic/wave propagations due to numerical dispersions and Gibbs phenomenon. The PNM models arbitrary fractures independently of the original mesh. Through several numerical examples it has been demonstrated that the spurious oscillations that appear in propagation pattern of high-frequency waves in PNM simulations can be effectively suppressed by employing the enriched model. This is observed to be especially important in fractured media where both primary waves and the secondary reflected waves are present.

The second objective of the thesis is to develop a mixed numerical model for simulation of wave propagation in discontinuous porous media and interface modeling. This objective is realized in Chapter 3 of the thesis. In this chapter, a new enriched mixed finite element model is introduced for simulation of wave propagation in fractured porous media, based on an extension of the developed numerical method in Chapter 2. Moreover, frictional contact at interfaces is modeled and realized using an augmented Lagrange multiplier scheme. Through various numerical examples, the effectiveness of the developed enriched FE model over conventional approaches is demonstrated. Moreover, it is shown that the most accurate wave results with the least amount of spurious oscillations are achieved when both the displacement and pore pressure fields are enriched with appropriate trigonometric functions.

The third objective of the thesis is to develop computational models for the simulation of acoustic emissions induced by fracture reactivation and shear slip. This objective is realized in Chapter 4 of the thesis. In this chapter, an enriched mixed finite element model (introduced in Chapter 3) is developed to simulate the interface slip instability and the associated induced acoustic wave propagation processes, concurrently. Acoustic events are triggered through a sudden release of strain energy at the fracture interfaces due to shear slip instability. The shear slip is induced via hydraulic stimulation that switches the interface behaviour from a stick to slip condition. The superior capability of the proposed enriched mixed finite element model (i.e., PNM-GFEM-M) in comparison with regular finite element models in inhibiting the spurious oscillations and numerical dispersions of acoustic signals in both velocity and pore pressure fields is demonstrated through several numerical studies. Moreover, the effects of different characteristics of the system, such as permeability, viscous damping, and friction coefficient at the interface are investigated in various examples.

Acknowledgments

I wish to thank my supervisor, Dr. Robert Gracie, for his sincere support and encouragement. I also thank the committee members for reviewing this thesis.

Dedication

To my parents for all their love and sacrifices.

Table of contents

List of figures

List of tables

List of abbreviations

FE- Finite Element

FEM- Finite Element Method

PU- Partition-of-Unity

PUM- Partition-of-Unity Method

PUFEM- Partition-of-Unity Finite Element Method

XFEM- eXtended Finite Element Method

PNM- Phantom Node Method

GFEM- Generalized Finite Element Method

PNM-GFEM- Generalized Finite Element Method-enriched Phantom Node Method

PNM-GFEM-M- Mixed Generalized Finite Element Method-enriched Phantom Node Method

HF- Hydraulic Fracturing

MS- Micro-Seismicity

EDM- Element Deletion Method

BEM- Boundary Element Method

FS- Fundamental Solution

DEM- Discrete Element Method

LEFM- Linear Elastic Fracture Mechanics

SIF- Stress Intensity Factor

List of symbols

x - longitudinal direction

y - lateral direction

u - general displacement

$\dot{u}$ - first order time derivative of general displacement

$\ddot{u}$ - second order time derivative of general displacement

p - pore pressure

ε - general axial strain

γ - general shear strain

σ - general stress

$\boldsymbol{b}$ - body force vector

$\bar{\boldsymbol{t}}$ - external traction vector

δ - variation symbol

$\boldsymbol{C}$ - elastic coefficient tensor

ρ - density of material

n - cutoff number of harmonic enrichment functions in x direction

m - cutoff number of harmonic enrichment functions in y direction

Λ_x - wave length in x direction

Λ_y - wave length in y direction

$\phi^{\gamma}_{(k_x,k_y)}$ - typical enrichment basis function

N_I - regular FE shape function associated with node I

$f(x, y)$ - level set function

σ' - general effective stress

$\dot{w}$ - general relative velocity of pore fluid with respect to solid skeleton

$\nabla\cdot$ - divergence operator

∇ - gradient operator

ρ_f - density of pore fluid

ρ_s - density of solid skeleton

n' - porosity of porous media

α_p - Biot's coefficient

$\boldsymbol{k_f}$ - permeability tensor

Q - incompressibility coefficient

K_s - bulk moduli of solid skeleton

K_f - bulk moduli of pore fluid

$\bar{\boldsymbol{t}}_{\boldsymbol{d}}$ - contact traction vector

μ_1 - viscous damping coefficient of solid skeleton

μ_2 - viscous damping coefficient of solid skeleton

g_N - normal contact inter-penetration

g_T - tangential contact slip

$\bar{\lambda}_N$ - normal contact traction

$\bar{\lambda}_T$ - frictional contact traction

$\bar{\boldsymbol{N}}$ - interface interpolation shape function matrix

μ_f - interface friction coefficient

Chapter 1

Introduction

In this chapter, an overview of hydraulic fracturing and acoustic emission modeling has been provided. Different numerical methods for simulation of discontinuity and propagation of fractures have been briefly introduced and discussed, followed by introduction of different time integration methods for dynamic analysis. Subsequently, different crack instability criteria and simulation methods have been explained along with interface modeling schemes. Numerical methodologies for coupled hydro-mechanical simulation of fractured formations and induced acoustic emissions have been discussed. In the last stage, research motivations, objectives, and methodologies used to carry out the research have been elaborated.

1.1 An introduction to Hydraulic Fracturing and induced Acoustic Emission analysis and simulation

Extracting oil and gas from unconventional low permeable reservoirs has gained a lot of interest for about a decade due to the significant development in the technology, especially the possibility of drilling horizontal wells in formations. In conventional shale reservoirs oil and gas migrate from the main source to more permeable limestone and sandstone formations and therefore they are more convenient to extract. But in unconventional reservoirs oil/gas are trapped in low permeable formation and therefore cracking is required for the extraction.

The natural oil and gas industry has been revolutionized by horizontal well drilling technologies that have significantly contributed to the efficiency and possibility of gas extraction from shale. The natural gas domestic production of the United States has been increase from 65 % to 95 % in 2011 [3]. It is estimated that by 2035 US shale gas production will comprise 46 % of the total natural gas production worldwide [4]. Canada is the third largest producer and the second largest exporter of natural gas according to the Government of Alberta [5].

Due to the complex multiple physics involved, the process of extracting oil and gas from shale rocks is one of the most complicated engineering challenges but offers the prospect of cheap and reliable supply of energy for the next decades [1]. The process of hydraulically stimulating tight formations such as shales by increasing their permeability through making networks of discontinuity (i.e., cracks) in them is called Hydraulic Fracturing (HF) [1]. The production of natural gas and oil can be stimulated by pumping in huge amount of high pressure fluid to increase the permeability of the formation by cracking and thereby easing the transport of the trapped oil and gas.

The development of effective engineering solutions for more efficiently extracting gas and oil from unconventional low permeable reservoirs is partially dependent on availability of reli-

able numerical models and softwares that can simulate the process of hydraulic fracturing from crack network generation to micro-seismicity (MS) emission due to cracking and/or activation of weak discontinuities and reactivation of natural fractures due to pressurizing. Many environmental concerns exist about the process of hydraulic fracturing, including the extent of the development of the induced hydraulic fractures and reactivation of the pre-existing cracks due to pressurizing that can alter the pattern of the in-situ stresses and pore fluid pressure [129]. All the mentioned issues necessitate more detailed investigation of the process of HF through developing more accurate computational programs that can accommodate more of the complicated/coupled mechanics of the problem.

The main problem in developing accurate simulators for HF is the significant amount of uncertainties that are involved. Many models have been introduced for HF over past few decades that either include many remarkable simplifications or focus on few aspect of the problem (toughness or viscosity dominated crack propagation, material inhomogeneity and anisotropy, poroelastic coupling, etc.). Moreover, the scarcity of the field data such as in-situ stress is another complicated limitation [1]. The environmental risks of the shale gas development has been quantified in [2] based on integrated assessment models.

Different coupled mechanics and physics involved in modeling HF in a porous media include: the viscous flow of the driving fluid within the hydraulic fracture, the flow of the pore fluid in the formation, the deformation of solid skeleton of the porous media around the fracture, the leak-off of the hydraulic fluid from the fracture to the surrounding porous media, propagation of the strong discontinuities due to the change of the stress pattern in the form of crack and/or shear band propagation, and microseismic emission due to fracturing and fault reactivation [127]. To define the problem of interest in this research, a schematic picture of a typical fractured formation under hydraulic fracturing/stimulation and induced acoustic emission has been exhibited in figure 1.1.

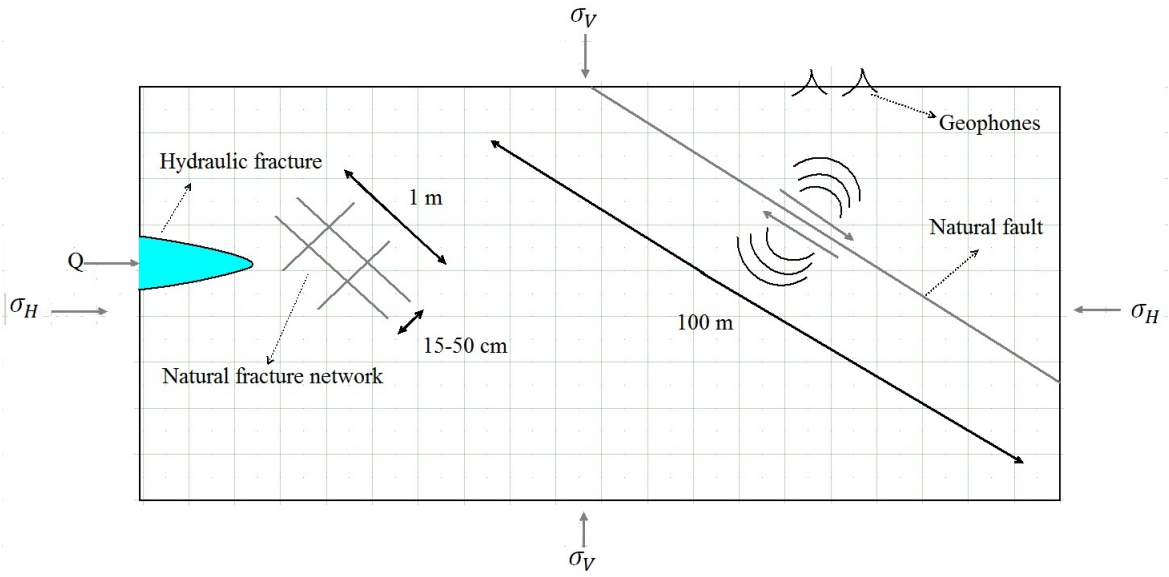

Fig. 1.1: A schematic figure of a typical fractured formation under hydraulic fracturing/stimulation and induced acoustic emission.

One of the biggest challenges in the simulation of hydraulic fracturing is the hydro-mechanical coupling between the fluid flow within the fracture with the pore fluid flow in surrounding media and deformation of the solid skeleton. The prescribed couplings result in a system of fully coupled differential equation from different physics and scales [127]. The convergence, stability, and accuracy of the solution can involve many practical challenges in large scale problems specially when nonlinear effects such as contact forces and complex constitutive relations and deformations are included [43]. Some other phenomena can contribute to the complexity and practical limitations of the problem. For instance, the leak off between the fracturing fluid and the surrounding pore pressure can be very challenging to model as many stochastic events can affect its behaviour [6]. Moreover, the lack of field data typically makes the problem much more complicated. Another challenging aspect is the lag between fluid front and the fracture front in the propagation process and how to model it. Besides, different asymptotic fields and singular behaviours near crack tip need to be accounted for to come up with more accurate results [48].

The problem of microseismic emission due to dynamic fracturing or slope instability (which is attributed to release of strain energy) is of great importance in probing the behaviour of

solids and geological formations. This part of HF stimulation has not been well treated in the open literature to date, and has not been dealt with very clearly, specifically, and accurately from the continuum mechanics and elastodynamics point of view [71].

Transient wave emission happens in the process of shear rupturing and tensile fracturing due to localization and release of strain energy [139]. Although several numerical models have been developed to model failure processes, only a limited number of works investigate acoustic wave emission phenomenon and still most of them suffer from very significant simplifications and assumptions that can result in inaccurate data and loss of important mechanics [71]. In fact acoustic emission is a high-frequency transient mechanical wave that is attributed to the abrupt release of energy due to failure [63]. Seismic (or microseismic) emission in geomaterials is triggered due to localization behaviour, fracturing, and sliding of preexisting natural fractures and fault surfaces along each other. The damage evolution characteristics can be evaluated based on the measurement of wave emission by developing correlations between the source of seismicity (damage behaviour) and the acoustic wave captured at particular points (geophone locations) [132].

Developing a continuum mechanics-based model, that can more realistically and accurately simulate stimulation and propagation of mechanical waves in porous media, can be very promising in prediction and analysis of HF induced seismicity that is deemed a big environmental and safety concern in the fracking industry [1]. Improved simulations can provide great insight into the relationship between MS and HF. Also, seismic and acoustic analysis can be very effective tools for improving understanding about various characteristics of the fracture network evolution through the stimulation processes. Acoustic emissions can be detected and recorded via geophones that are located through the field near the ground surface. Many valuable information about the stimulated zone (e.g., damage evolution and fault reactivation characteristics and location) can be obtained through conducting inverse analysis on the recorded signals [63, 66].

1.2 Numerical Methods for crack modeling

An important portion of HF simulation is to model fractures (both stationary and evolving) in a continuum media. Different numerical schemes can be used to model strong discontinuity (crack) in problems. Here a brief introduction is provided about different numerical methods that have been used in the scope.

1.2.1 The Element Deletion Method

The Element Deletion Method (EDM) is the simplest method of modeling crack propagation in the context of regular/conventional FEM. Some commercial softwares such as LS-DYNA [16]remove the mass of the damaged elements that no longer have load bearing potential. In this method the damaged/fractured area is modeled by deleting elements and there is no need for explicitly representing a strong discontinuity in the domain. In EDM the deleted elements have zero stress and zero material resistance. There is a spurious mesh dependency involved in the nature of this method as the released energy due to deleting an element depends on the element size. In this method, the constitutive damage equation is scaled to reduce the mesh dependency of the energy release due to element deletion [17]. The energy dissipation in the element based on the elastic-softening constitutive model is then equated to the fracture energy required for propagation of the crack through the element. No information about the element orientation and shape is included in the analysis which is a drawback in the method. Nevertheless, the EDM is used in some applications because of the simplicity of the implementation.

1.2.2 Boundary Element Method

The Boundary Element Method (BEM) has been first introduced in the pioneering work of Cruse and Rizzo [13] for elastodynamics problems. The main advantage of BEM over FEM is that the discretization is needed to be implemented only on the boundaries that will result in a reduction in dimensionality of the problem. Besides, in BEM very accurate solutions can be obtained due to including a mathematical representation of the physics involved through a

fundamental solution. However, there is a very important practical setback in using BEM and it is the need of having a Fundamental Solution (FS) that represents the response of infinite domain of material under point force. The application of BEM may be infeasible in problems where the FS is not known. Crack propagation problem has been investigated in the framework of the BEM in [14].The maximum stress is considered as crack tip stability criteria. The cohesive crack models have also been implemented in the context of BEM by consideration of additional boundary elements for cohesive fictitious crack tip region that satisfies the softening constitutive separation-traction law [15]. However, in this method the crack path needs to be known *a priori*.

1.2.3 The Interelement Crack Method

In the interelement crack methods the discontinuity in the domain due to cracks is modeled by displacement jump along element edges. The crack trajectory is restricted to inter-element bounds and therefore the problem of mesh dependence of the solution and/or requirement for continuous remeshing may arise. Two main categories exist based on this approach. In the methodology proposed by Xu & Needleman [18] the elements are considered separated from the beginning. The interelement edges are connected via cohesive traction-separation forces. On the other hand, Ortiz & Camacho [19] introduced a modified approach in which the separation of the elements at edges may happen only when the nucleation criteria is met. After fragmentation an explicit frictional contact model is used to solve the multibody elastodynamics problem. This method has been shown to be adaptable in simulating crack nucleation and branching [17]. However, the main shortcoming of this method is the restriction of the crack path to the interelement edges which contributes to the mesh-dependency of the method. The problem of mesh-dependency can be rectified to some extent by using classical finite element approaches that employ automatic mesh generation, however, the process of continuous re-meshing during crack propagation can be computationally expensive and rather slow.

1.2.4 The eXtended Finite Element Method

To overcome the shortcoming of the conventional finite element methods and to avoid the burden of the need for continuous remeshing in the process of crack propagation, based on the general concept of the Partition-of-Unity Finite Element Method (PUFEM) developed in the pioneering work of Melenk and Babuška [20], the idea of locally enriching the conventional finite element approximation with additional functions for modeling discontinuity within the element has been developed by Belytschko and Black [24] and Moës, Dolbow, and Belytschko [26] setting up the framework of the eXtended Finite Element Method (XFEM). In this method, the elements that are fully cut by a discontinuity are enriched using a step (or Heaviside) function enabling sudden jumps in displacement fields within elements.

To embed the singularity of the stress field at the crack tip zone in the framework of the linear elastic fracture mechanics, and to satisfy the zero-opening/jump condition at the crack tip of the elements that are partially cut by a discontinuity, some asymptotic type enrichment basis functions are used in the displacement interpolation of the elements in which the crack tip is located inside the element [26]. The distinction between the XFEM and the GFEM (Generalized Finite Element Method) is ambiguous in the literature; at their core, both methods are identical as they involve using local and/or global enrichment of a finite element basis [27]. In this research, the term XFEM will be used to refer to a FEM locally enriched with the Heaviside step function to model the discontinuities of fractures and so would include the GFEM model of Gupta et al. [28]. The term GFEM will be reserved for global enrichment using harmonic functions.

1.2.5 Phantom Node Method

Phantom Node Method (PNM) is an XFEM variant in which a cracked element is represented by superposition of two intact elements with original real and additional fictitious/phantom nodes [29], as schematically illustrated in Figure 1.2. PNM formulation can be reached by rear-

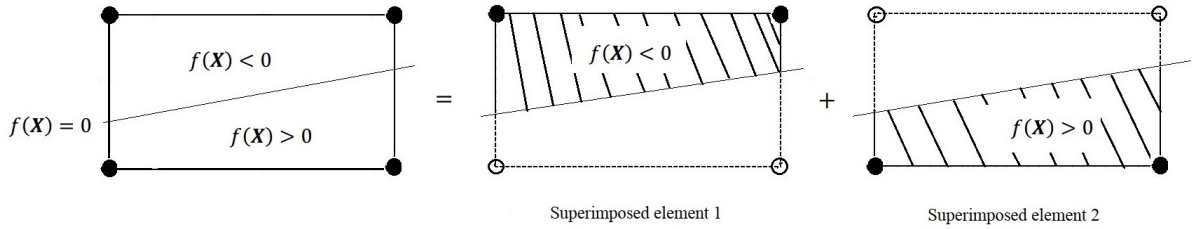

Fig. 1.2: Decomposition of a cracked element into two superimposed paired elements with original real and additional phantom nodes in the PNM. Original real nodes and additional phantom nodes are shown by solid and hollow circles, respectively.

rangement of XFEM element interpolations with step function enrichment [30]. The Phantom Node Method was proposed in [29] to model discontinuities and is essentially the same as the earlier method proposed by Hansbo and Hansbo [31] for modeling strong and weak discontinuities inside an element. Each of the superimposed elements is used to model a different side of the original fractured element, leading to a discontinuous approximation for displacement field. The advantage of the Phantom Node formulation over that of the original XFEM is that an implementation of the PNM requires fewer modifications to an existing FEM code than a comparable XFEM implementation [29]; however, in principle the two formulations should yield equivalent results for small displacement analysis [32]. It is noted that most XFEM codes have also crack-tip enrichment functions. As such, the PNM is similar to an XFEM with pure jump enrichment.

In the context of the PNM, the discontinuous variable (e.g., displacement filed, u) in a cracked element is interpolated through the following distribution function:

$$u(x,y) = H(-f(x,y)) \sum_{I \in S_1} \Big(N_I(x,y) u_I \Big) + H(f(x,y)) \sum_{I \in S_2} \Big(N_I(x,y) u_I \Big) \tag{1.1}$$

where N_I is the shape function for node I and u_I denotes the associated real or phantom degree of freedom. $f(x,y)$ is the level set function to locate the fracture, in the way that $f(x,y) = 0$ specifies the fracture surface. $H(\cdot)$ is the Heaviside function [32], and S_1 and S_2 are the sets of original real and additional phantom nodes associated with the superimposed elements 1 and 2, respectively, as shown in Figure 1.2.

1.2.6 Discrete Element Method

The discrete Element Method (DEM) was first developed for particle-like materials such as rocks. The method is based on modeling the interaction of blocks/elements using contact forces and was proposed by Cundall and Hart [38]. Normal contact stiffness accounts for normal interaction and inter-penetration constraint and shear contact stiffness is introduced into the formulation to allow for rotation of blocks [71]. The main problem that can arise in DEM is the contact detection between all neighboring elements. Inspection of all the elements for the potential contact requires huge amount of calculation and the computational burden can be prohibitive in large scale problems [17]. Body based search is the most common algorithm to search for possible contact conditions in the vicinity of a given discrete element. The search algorithm need to be repeated after a number of iterations to check whether or not the interactive elements are still in contact [1].

After detection of contacts the next step is to determine contact forces. The Penalty Method [43] is usually used to specify the interpenetration and associated contact forces. However, Lagrange Multiplier-based methods [124, 123] are more accurate because they can exactly satisfy the normal geometric penetration constraint through introduction of a new unknown parameter representing contact force between discontinuous faces. Simulation of crack propagation in DEM is very similar to the Interelement Crack Method [19]. In DEM crack growth trajectory is mostly confined to interfaces of elements. Damage evolution is simulated through debonding of links between elements. The main shortcoming of DEM is the mesh dependency of the algorithm [17] and restriction of the crack path to interfaces of elements that can affect the possibility of shear failure modeling [71], shear band propagation simulation and determination of actual crack path.

1.2.7 Phase Field Method

Discrete crack models (e.g., XFEM, interelement method, etc) are very commonly-used in fracture simulations. In all these methods cracks are treated as strong discontinuities in the domain and are modeled through consideration of displacement jump at element edges or introducing step function-type enrichments in the framework of the local PUFEM. Tracking the discrete discontinuities has been proven to be very burdensome and tedious [17], in three-dimension, in particular.

Recently, a new alternative branch has been introduced and developed based on specifying a damaged area in the domain via a phase-field function that denotes the extent of the damaged zone and smooths the boundary of the crack over a small zone [39]. The magnitude of the phase-field functions changes gradually over the domain which implies a spacial variation from fully damaged to undamaged state. Hence, there is no need to specify discontinuity in displacement field of the domain to model crack evolution [40]. In this method the fracture energy is approximated using the phase-field function over the domain and the total Lagrangian energy functional of the system is represented in the form of the contributions of kinetic energy, elastic energy, and fracture energy [41]. The mentioned Lagrangian energy is represented in terms of the displacement field and the phase field. Afterwards, the Euler-Lagrange equations are used to arrive at the strong form equations of motion. Then the developed equations can be solved to obtain the displacement field as well as the phase field. The distribution of the phase-field value over the domain represents the extent/location of the fractures. The value of this phase-field is equal to unity away from the crack and is equal to zero at the core of the crack [41].

1.3 Numerical Time integration methods

In the preceding section different numerical methods and strategies have been introduced and discussed for crack simulation. In the numerical simulation using discrete methods the spatial domain is typically discretized using interpolation functions resulting to semi-discretized algebraic equations as below

$$[M]\left\{\ddot{\Delta}\right\} + [C]\left\{\dot{\Delta}\right\} + [K]\{\Delta\} - \{F\} = 0 \tag{1.2}$$

where $[M]$, $[C]$, and $[K]$ are inertia, damping, and stiffness matrices, and $\{\Delta\}$ and $\{F\}$ are the vector of unknowns and force vector, respectively.

Due to the time dependency of the discrete nodal values a time integration method needs to be implemented. Different methods have been proposed and used over years for time integration. In general, time integration methods can be divided into two categories; Explicit and implicit schemes. A time integration is implicit if its solution process requires a factorization of an 'effective stiffness' [74] and is explicit otherwise.

Each type of integration has its own advantages and disadvantages. The main advantage of explicit time integration is that in general less computational effort is needed compared to implicit methods especially when diagonal mass, i.e. lumped mass, is considered in which the coupled system of algebraic equations reduce to fully decoupled one-by-one equations that does not require any matrix inversion in the solution process [82]. Besides, in nonlinear problems, explicit methods do not require iterative schemes, such as Picard or Newton-Raphson method for each time step, and the converged solution of the *vector of unknowns* in each time step can be concluded in only one iteration by explicitly integrating the second-order time derivative of the vector of unknowns [74].

It is noted that the accuracy of the nonlinear solution in explicit methods is another issue that

needs to be considered separately. However, explicit time integrations always requires a specific maximum amount for time step size for the solution to be stable [83]. In general, the biggest advantage of implicit time integration is its unconditionally stable characteristic. However, in some cases (especially in the problems that involve steep gradients, such as wave propagation) very small time steps are needed for accuracy [32]. In those problems, because of the necessity of small time increments from physical point of view, implicit time integrations are not worth their computational cost. Therefore, in wave propagation problems explicit time integration are of more interest.

Here, for the sake of completeness, we represent some of the commonly used time integration methods:

1.3.1 Temporal element method

Finite difference-based time integration methods are based on truncation of Taylor series expansion for displacement, velocity, and acceleration and finding the results using time marching. The finite element approach has been used for discretization over time in a similar fashion as spatial discretization [87]. Different approaches have been used for finite element discretization over time using different types of interpolation functions. Here, a weighted residual temporal element method is explained based on the finite element discretization.

The semi-discretized finite element equations can be developed based on finite element analysis over spatial domain [87]. To discretize the mentioned equations (Eq. 1.2) over time using temporal finite elements the weighted residual method is employed as below:

$$\int_{t_{i-1}}^{t_{i+1}} W \left([M] \left\{ \ddot{\Delta} \right\} + [K] \{\Delta\} - \{F\} \right) dt = 0 \tag{1.3}$$

where W is a weight function.

A three-node one-dimensional temporal element with quadratic shape functions is used to interpolate the variables and forces over time. The mentioned parameters are interpolated over

time using the nodal values of the preceding, current, and the next time step. The nodal values and force vector are interpolated as:

$$\{\Delta\} = N_{i-1}\{\Delta_{i-1}\} + N_i\{\Delta_i\} + N_{i+1}\{\Delta_{i+1}\} \tag{1.4}$$

$$\{F\} = N_{i-1}\{F_{i-1}\} + N_i\{F_i\} + N_{i+1}\{F_{i+1}\} \tag{1.5}$$

where the subscripts $i-1$, i, and $i+1$ represent the previous, current, and next time step, respectively.

The quadratic finite element interpolation functions are:

$$N_{i-1} = -0.5(r)(r-1),\ N_i = (r+1)(r-1),\ N_{i+1} = 0.5(r)(r+1) \tag{1.6}$$

where

$$r = \frac{t - t_i}{\Delta t},\ \ t_{i-1} \le t \le t_{i+1} \tag{1.7}$$

Using the chain rule, the second order derivative of the vector of unknowns can be obtained according to (1.4):

$$\left\{\ddot{\Delta}\right\} = \frac{1}{(\Delta t)^2}(\Delta_{i-1} - 2\Delta_i + \Delta_{i+1}) \tag{1.8}$$

Substituting (1.4) and (1.8) into the element level weighted residual form of the semi-discretized motion equation (i.e., Eq. (1.3)) and integrating over time, one can come up with the fully discretized motion equation as:

$$[M + \lambda K\Delta T^2]\{\Delta_{i+1}\} = [2M - (0.5 - 2\lambda + \gamma)K\Delta T^2]\{\Delta_i\} +$$

$$[-M - (0.5 + \lambda - \gamma)K\Delta T^2]\{\Delta_{i-1}\} - (0.5 + \lambda - \gamma)\Delta T^2\{F_{i-1}\} -$$

$$(0.5 - 2\lambda + \gamma)\Delta T^2\{F_i\} - \lambda\Delta T^2\{F_{i+1}\} \tag{1.9}$$

where

$$\lambda = \frac{\int_{-1}^{1} 0.5Wr(r+1)dr}{\int_{-1}^{1} Wdr},\ \gamma = \frac{\int_{-1}^{1} 0.5W(r+0.5)dr}{\int_{-1}^{1} Wdr} \tag{1.10}$$

As can be seen in (1.9), the fully-discretized equation of motion is developed in the form of a factorization of an effective stiffness. Therefore, the temporal element method is basically an implicit time integration scheme, and the nodal values of the next time step can be determined through the solution of a linear system of equations based on the converged values of the current and the previous time steps.

1.3.2 Newmark's implicit integration

In the Newmark's family of time integration the variables and their time derivatives are approximated as [88]:

$$\begin{aligned}
\{\Delta\}_{i+1} &= \{\Delta\}_i + \Delta t \left\{\dot{\Delta}\right\}_i + \frac{1}{2}\Delta t^2 \left\{\ddot{\Delta}\right\}_{i+\gamma} \\
\left\{\dot{\Delta}\right\}_{i+1} &= \left\{\dot{\Delta}\right\}_i + \Delta t \left\{\ddot{\Delta}\right\}_{i+\alpha} \\
\left\{\ddot{\Delta}\right\}_{i+\alpha} &= (1-\alpha)\left\{\ddot{\Delta}\right\}_i + \alpha \left\{\ddot{\Delta}\right\}_{i+1}
\end{aligned} \tag{1.11}$$

α and γ are the parameters that determine stability and accuracy of the method. The ordinary semi-discretized equations of motion (Eq. 1.2) can be reduced to algebraic fully-discretized equations by making use of (1.11).

$$[\hat{K}]_{i+1} \{\Delta\}_{i+1} = \left\{\hat{F}\right\}_{i,i+1} \tag{1.12}$$

where

$$[\hat{K}]_{i+1} = [K]_{i+1} + a_3[M]_{i+1}, \tag{1.13}$$

$$\left\{\hat{F}\right\}_{i,i+1} = \{F\}_{i+1} + [M]_{i+1} \{A\}_i, A_i = a_3 \{\Delta\}_i + a_4 \left\{\dot{\Delta}\right\}_i + a_5 \left\{\ddot{\Delta}\right\}_i \tag{1.14}$$

Parameters that appear in the above equations are defined as:

$$a_1 = \alpha\Delta t, a_2 = (1-\alpha)\Delta t, a_3 = \frac{1}{\beta\Delta t^2}, a_4 = a_3\Delta t, a_5 = \frac{1}{\gamma} - 1, \gamma = 2\beta \tag{1.15}$$

As seen, the Newmark's time integration procedure requires a factorization of an effective stiffness matrix, i.e. $\hat{K}$, and therefore the scheme is an implicit time integration method [74].

1.3.3 Central difference explicit method

As mentioned before, a time integration method is implicit if its solution process results in a factorization of an effective stiffness matrix. Otherwise, it is called explicit. Among all explicit time integrations, the "central difference method" is still very widely-used in dynamic analysis of vast variety of problems. Central difference method has the largest time increment stability limit of any second-order accurate explicit method [83]. Unlike implicit methods, in explicit schemes the time integration process is performed explicitly starting from the values of the acceleration vector. The acceleration is obtained form the solution of the following equation

$$[M]\left\{\ddot{\Delta}_i\right\} = \left\{F^{ext}\right\}_i - \left\{F^{int}\right\}_i \tag{1.16}$$

Once the second time derivative of the unknown vector is obtained for the current time step, the first order derivative vector (velocity) in the half step may be calculated through direct/explicit integration in the framework of the central difference method [25]:

$$\left\{\dot{\Delta}\right\}_{i+1/2} = \left\{\dot{\Delta}\right\}_i + (t_{i+1/2} - t_i)\left\{\ddot{\Delta}\right\}_i \tag{1.17}$$

Subsequently, the unknown vector (displacement) can be evaluated in the next time step in terms of the half-step velocity obtained in the preceding stage.

$$\{\Delta\}_{i+1} = \{\Delta\}_i + (t_{i+1} - t_i)\left\{\dot{\Delta}\right\}_{i+1/2} \tag{1.18}$$

Hence, the vector of unknown parameters of the problem may be evaluated at each time step via a direct integration from the second order time derivatives. In the case in which diagonal mass matrix is used, there is no need to solve any system of equations as a fully-decoupled system would be developed in (1.16). However, the mentioned central difference explicit method is only conditionally stable. The critical time step (for undamped systems) is calculated through an eigen-value procedure over (1.16) as follows [25]:

$$\Delta t_{critical} = 2/\omega_{max}, \tag{1.19}$$

where ω_{max} is the maximum natural frequency of the semi-discretized system of motion equation that can be calculated from the standard eigenvalue procedure.

1.3.4 Dissipative explicit methods

The central difference explicit method is a non-dissipative scheme [74]. Therefore, the numerical simulation may be very inaccurate because of the dispersion error created by high-frequency modes. To treat this problem, many dissipative time integrations have been introduced and used in order to numerically damp the high-frequency oscillations [82]. The main challenge in developing the dissipative time integration methods is that the numerical damping/dissipation of the scheme needs to be large enough to reduce the spurious oscillations in high frequency modes, and concurrently, be able to maintain good accuracy of low-frequency range [83].

Noh and Bathe [83] recently introduced a new two-step dissipative explicit time integration method for the solution of wave problems. They show that by consideration of specific values for integration constants the method has good potential of damping high-frequency modes while resulting in acceptable accuracy in low-frequency span. In other words, the spectral radii analysis demonstrates that the proposed time integration results in imposing numerical dissipation in high-frequency range, while for the low-frequency range the spectral radii remains close to unity resulting in very little numerical dissipation.

1.4 Crack propagation conditions

Analytical solution of cracked media based on the concept of the Linear Elastic Fracture Mechanics (LEFM) results in asymptotic behaviour in the stress field and singularity of the stress at the crack tip. Irwin [46] represented that the asymptotic behaviour of stress field at crack tip is governed by a parameter which depends on the geometry of the crack and the applied force, named the Stress Intensity Factor (SIF). The SIFs K_I, K_{II}, K_{III}, correspond to three crack behaviour modes known as mode I (opening), mode II (sliding), and mode III (tearing).

Williams [47] used the Airy stress function to obtain the asymptotic behaviour of the stress field in the vicinity of the crack tip in polar coordinate system (r, θ) centered at the crack tip. The Airy stress function satisfying the biharmonic equation (i.e., equilibrium equation) may be represented as:

$$\Phi = r^{\lambda+1} \{C_1 sin(\lambda+1)\theta + C_2 cos(\lambda+1)\theta + C_3 sin(\lambda-1)\theta + C_4 cos(\lambda-1)\theta\} \tag{1.20}$$

Without consideration of any particular boundary condition at crack faces, the basis components of the displacement field associated with (1.20) are:

$$\psi^{u,\lambda} = r^{\lambda} \{sin(\lambda\theta), cos(\lambda\theta), sin(\lambda-2)\theta, cos(\lambda-2)\theta\} \tag{1.21}$$

where λ is a constant power-law parameter.

To produce the asymptotic (i.e., singular) behaviour of the stress field with finite strain energy in the vicinity of the crack tip, the power-law component has the limitation: $0.5 \leq \lambda < 1$. For a traction free crack, $\lambda = 0.5$, the enrichment basis (1.21) is equivalent to the classic basis which is used in regular crack tip enrichment in XFEM [48].

In HF, for the general power-law crack tip asymptotic behaviour with consideration of the effect of fluid pressure on crack faces in obtaining the constants involved in the stress function (1.20),

the asymptotic basis functions have been considered to be [48]:

$$\Psi^{u,\lambda} = r^{\lambda}\left\{sin(\lambda\theta), cos(\lambda\theta), sin(\lambda\theta)sin(\theta), cos(\lambda\theta)sin(\theta)\right\} \tag{1.22}$$

The above HF asymptotic basis functions reduce to (1.21) for ($\lambda = 0.5$).

$\lambda = 0.5$ is associated with a crack in a homogeneous material under the assumption of the classical linear elastic fracture mechanics. Therefore, in HF literature/terminology it is attributed to the state of *toughness dominated regime*, in which the LEFM relations are retrieved with ignoring the effect of internal crack fluid as boundary conditions on the crack faces in developing the basis functions. On the other hand, $\lambda = \frac{2}{3}$ is attributed to the state of *viscosity dominate regime* in which the applied fluid pressure to the crack faces is in equilibrium with the far field in-situ stress in normal direction, and the energy dissipation primarily occurs due to flow of a viscose fluid inside the crack.

The SIF has been widely used as a crack propagation criteria in the context of LEFM [26]. Based on this crack tip stability criterion, crack propagation starts when the mode I SIF due to external force reaches a critical value which is the fracture toughness that is a material property. In general, two types of criteria exists for brittle crack tip stability; the first one is point-wise and the second one is energy-based:

1. Maximum hoop stress: This criteria has been proposed by Erdogan and Shi [49] based on two main hypotheses:

a. crack propagation originates from the tip in radial direction.

b. The crack propagation direction is perpendicular to the maximum tensile hoop stress (which is not necessarily the maximum principle stress in the vicinity of the crack tip).

2. Strain energy release rate: In this criterion, crack propagates when strain energy release per unit length of crack growth reaches a specific value. The crack extension occurs in a direction in which the energy release is maximum [51].

The crack propagates when stress intensity factor reaches a particular critical value of material toughness. This propagation criteria has been extended to the case of orthotropic material in [50]. In this method an equivalent fracture toughness is developed for anisotropic material as a function of fracture toughness values along principle axes of orthotropy and the circumferential angel with respect to the material orientation axis.

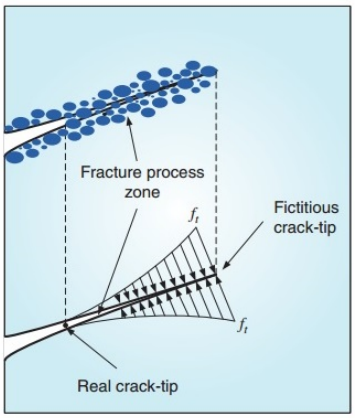

Fig. 1.3: Illustration of the fracture process zone [43].

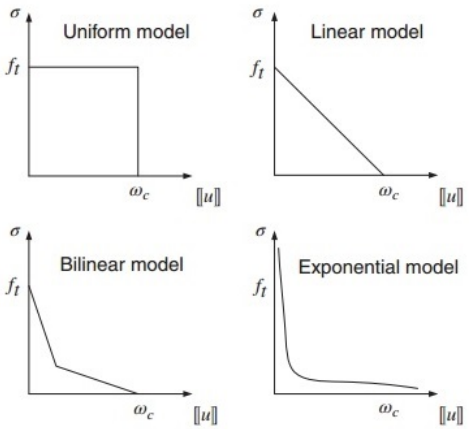

Fig. 1.4: Traction-separation relations.

1.5 Cohesive crack model

Linear Elastic Fracture Mechanics (LEFM) is applicable only when the fracture process zone at crack tip is small in comparison to the size of the specimen [93]. The cohesive crack model is a simple implementation of lumping the damaged zone at the crack tip area over a line. The level of damage is represented and modeled by cohesive traction-separation relation (softening law) which mimics elastic softening damage models.

The cohesive crack model was first proposed by Dugdale [59] and Barenblatt [60]. The cohesive zone is defined between two crack point/tips named the real crack tip (i.e., physical tip) and fictitious tip (i.e., mathematical tip). The real crack tip is the point that separates the cohesive zone from the traction free crack faces and the fictitious tip is the point which is placed at the cohesive zone tip and separates the cohesive zone from the rest of the un-cracked body [61]. The cohesive traction at the fictitious tip is equal to the maximum tensile strength of the material ensuring the nonsingular behaviour of the stress distribution at crack tip area. This is one of the main motivations in developing the cohesive crack models to avoid non-physical singular stress magnitude at the tip that arises in LEFM. Figures (1.3) and (1.4) provide schematic representation of the fracture process zone and different traction-separation laws, respectively.

The cohesive crack models have been used to simulate crack propagation in different solution contexts. In some approaches based on the conventional finite element methods the crack extension is only restricted to the inter-element edges. Cohesive zones are considered between each two neighboring elements providing the possibility of the simulation of crack extension, crack branching, and fragmentation (see for instance, [18], [19]). To avoid the requirement for continuous re-meshing and to model arbitrary discontinuity and extension in a domain, the cohesive crack model has been extensively implemented in the frame work of local partition of unity finite element (or XFEM) [61].

Moës et al. developed a computational scheme for modeling crack growth based on cohesive traction-separation constitutive model in crack tip region in the framework of XFEM [61]. Based on the non-singular stress field at the crack tip field in cohesive zone, instead of point-wise quantities they used an energetic considerations for crack tip stability behaviour. They considered that the mode I stress intensity factor vanishes at the mathematical tip (cohesive zone tip) to ensure the non-singular stress pattern in that area. This way the summation of the stress intensity factors due to the external load and the cohesive forces are set to zero. The crack propagation angle, on the other hand, is determined based on the linear elastic fracture mechanics assumptions, as unlike the load-displacement stability path in crack propagation problems, the crack path is much less sensitive to the size effect (ductility) [61].

In [61] non-singular asymptotic enrichments have been embedded in the element displacement interpolations. It has been shown that the load-deflection curve of the fracturing beam has significant dependency on the fracture energy and size of the specimen (i.e., ductility). It has been demonstrated that for the specimens with lower ductility number the load deflection path exhibits very sharp limit-point behaviour; while in the case of more ductile materials (with larger cohesive zone) the load-deflection path due to crack propagation process is unique and much more stable. It is mentioned that ductile specimens tend to develop longer cohesive zones and at the limit when the ductility approaches zero the cohesive zone shrinks to a point (crack

tip) and in that case the linear elastic fracture mechanics is recovered for very low ductility numbers (brittle materials). In the mentioned work ([61]) the authors also show that in order to obtain reasonably smooth results the cohesive length needs to be covered by sufficient number of elements, otherwise severe oscillations appear in load-deflection (equilibrium) curves in the case of quasi-static crack propagation analysis.

The numerical model proposed in [61] for modeling crack growth using cohesive model has been extended in the work of Zi and Belytschko [62] by introducing a new crack tip element. In this work, all the elements (including the elements containing the crack tip) are enriched only by step function. Hence, no blending of local partition of unity is required. In the proposed approach of this work the partially cracked element that contains the crack tip is divided into two parts, i.e., cracked and un-cracked. To ensure the continuity of the un-cracked part, only the cracked part is enriched using the signed distance function by allocating the enriched degrees of freedom only to appropriate nodes.

1.6 Frictional contact simulation

Many engineering applications involve interface analysis of embedded surfaces. Geological discontinuities such as natural fractures and faults are usually under frictional contact condition between crack faces due to confining in-situ stresses. The problem of interface instability under compressive confining pressure field frequently arises in geostructures. Different types of interface instabilities may take place in geological formations such as tensile fracturing, shear rupturing, axial splitting, and shear banding [52, 53].

Through the literature, different numerical approaches have been used for modeling contact, including penalty methods and Lagrange multiplier methods [55]. A brief introduction has been provided below on some contact simulation numerical approaches.

1.6.1 Penalty method for contact problems

In penalty method, the normal contact constraint (no inter-penetration state) is imposed to the crack faces by considering normal contact stiffness between the interacting surfaces. The inter-penetration between the discontinuity faces can then be controlled by the magnitude of the stiffness constant assumed which is known as the *penalty parameter* [54]. This way, a nonlinear constitutive model is introduced in the local contacting part of the system between the inter-penetration and the normal contact force exerted to the discontinuity faces in opposite directions. Obviously, the accuracy of the normal contact constraint satisfaction is directly dependent on the magnitude of the contact stiffness (i.e., penalty parameter). The larger the magnitude of the penalty parameter, the better the contact constraint is satisfied. Nevertheless, very large contact stiffness magnitudes can result in high conditioning number of the total stiffness matrix of the system and the results obtained from an ill-conditioned system of equations can be inaccurate [43].

1.6.2 Lagrange multiplier method for contact problems

In the Lagrange multiplier approach the normal contact constraint is directly introduced into the variational energy equation (Lagrangian) of the system by consideration of an additional energy potential that is attributed to the variation of the energy of normal gap (penetration) and the contact force acting normal to the interface which is known as the Lagrange multiplier [56]. In this approach, since the variational energy contribution of normal contact forces is directly introduced to the system of equations, the normal contact constraint is thus accurately (i.e., implicitly) satisfied in the resulting solutions.

In this method due to the existence of the variational form of Lagrange multiplier parameter, the normal contact force is indeed one of the unknown parameters [57]. Therefore, in addition to regular displacement and pressure parameters, the normal contact force needs to be interpolated using finite element shape functions in one dimensional elements along the contact interfaces, resulting in more computational cost. Due to the introduction of a new unknown parameter, in this method, the dimension of the total stiffness matrix will be affected and existence of zero diagonal terms can result in complexity of the solution of the system of equations [43].

1.6.3 Augmented Lagrange multiplier method for contact problems

The Lagrange multiplier method introduced in the previous section can enforce the contact constraint accurately but due to the saddle point structure, the resulting system of equations is more difficult to solve. In the penalty method, the contact constraint can be enforced by assuming a very large value for the penalty method. However, consideration of a very large magnitude for the contact stiffness can result in ill-conditioning of the total stiffness matrix.

To remedy the mentioned issues that arise in the penalty method and the Lagrange multiplier method, alternative solutions have been developed based on combinations between these two conventional concepts of contact simulation which are known as *augmented Lagrange multiplier*

methods [57]. In this thesis, an Uzawa-type augmented Lagrange multiplier method will be used to enforce frictional contact condition. The contact constraint is satisfied through an iterative process by trying to minimize inter-penetration of discontinuity surfaces by updating the Lagrange multiplier (normal contact force) through a successive/sequential algorithm [43]. Hence, unlike the regular Lagrange multiplier method, in an augmented Lagrange multiplier technique the normal contact force (Lagrange multiplier) is not an unknown variable of the governing equations. The augmented Lagrange multiplier method consists of two loops. The Lagrange multipliers are kept constant in the inner loop while solving the governing equations. Then the Lagrange multipliers are updated in the outer loop to enforce the contact normal constraint (normal gap) to be within a specified tolerance [57].

1.7 Modeling of Hydraulic Fracturing

The process of hydraulic fracturing has a wide range of applications in engineering. HF is the main stimulation process in extracting hydrocarbons from low permeable unconventional reservoirs [1]. In HF a viscous fluid is used to pressurize the crack faces and generate the crack propagation energy. In fact, the applied pressure changes the stress pattern in the media and therefore, crack propagation or shear failure (fault reactivation) takes place once the crack tip or interface instability criteria are met.

A significant amount of effort has been spent in trying to model hydraulically driven fractures to date. Based on the plane strain assumption and radial hydraulic fracturing, Perkins-Kern-Norgren [7] and Geertsma and de Klerk [8] developed analytical solutions in their pioneering works. Afterwards, numerical models were developed first for fracture propagation simulation with dry cracks based on the Linear Elastic Fracture Mechanics (LEFM) [9, 10]. The mentioned models do not considered nonlinear effects of the crack tip zone. More recent works consider the effect of nonlinear material behaviour at the damaged Fracture Process Zone (FPZ) in the vicinity of the crack tip. Based on the FEM with mesh adaptation technique, Schrefler, Secchi, and Simoni [11], and Secchi, Simoni, and Schrefler [12] modeled the hydraulic cohesive crack growth in saturated porous media.

1.7.1 Hydraulic Fracturing based on partitioned solution between fluid flow inside the fracture and deformation of the surrounding media

Hydraulic fracturing simulation has been conducted in different ways with different assumptions. Boone and Ingraffea [42] developed a computational model based on a combination between Finite Element and Finite Difference method to simulate hydraulically-driven fracture propagation in poroelastic materials. The method is based on a partitioned solution using FEM for poroelastic equations in surrounding media and Finite Difference Method for solving the

fluid flow within the fracture. In this model the flow is assumed to be laminar, steady-state, and fully-developed between parallel surfaces. This approach is suitable for modeling hydraulic fracturing in low-permeable formations in which the fluid pressure within the fracture behaves as an inter-facial force on fracture faces without having a direct effect on pore fluid pressure of surrounding media [43]. This model is valid for fast crack propagation in low permeable porous media and has been widely used in hydraulic fracturing simulations as *partitioned solution* [44, 45]. In this approach the mass conservation equation for fluid flow inside the fracture is as below:

$$\frac{\partial q}{\partial s} + \frac{\partial w}{\partial t} + Q_0 = 0 \tag{1.23}$$

where w is the fracture opening, q is the flow flux along the fracture defined by curve linear coordinate s, and Q_0 is the fluid leak off from the fracture to the surrounding porous media.

Fluid flux in the fracture is traditionally represented by fluid equilibrium equation which is obtained using the lubrication/permeability equation of the fluid inside the crack as:

$$q = -\frac{w^3}{12\mu_f}\frac{\partial P}{\partial s} \tag{1.24}$$

where μ_f is the viscosity of the fluid and P is the fluid pressure acting on crack faces, and w is the crack aperture.

The mentioned fluid flow equation is solved using the finite difference method based on a pre-specified value for fracture length. It is noted that in [44] instead of the commonly-used finite difference scheme a one dimensional finite element method is used to solve the flow equation inside the crack. In this work, conventional finite element shape functions of one dimensional elements are used to interpolate the pressure field along a finite element and variation of pressure parameter is used as the test function to develop the weak form of the fluid flow equation. The length and opening of the crack is solved through an iterative procedure. The method can be extended to the case of permeable porous media by including some experimental relations for the fluid leak-off behaviour [6].

1.8 Acoustic emission in hydraulic fracturing

1.8.1 Introduction to microseismic/acoustic emission

Seismic monitoring has been first introduced as a tool for mine design prediction [67]. Afterwards, the idea of evaluating the microseismic emission was adopted for tracking the evolution of underground damage zone especially in studying fracture zone induced by pressurizing in hydraulic fracturing [68].

A number of works have been reported on quantitative evaluations of acoustic behaviour in formations. Very recently, Lisjak et al. [71] developed a computational tool for investigation of acoustic emissions in brittle rocks by conventional FEM/DEM analysis. In this work, a cohesive law is assumed between elements similar to the discrete inter-element method proposed in the pioneering works of Xu and Needleman [18] and Camacho and Ortiz [19]. However, the main shortcoming of the method they used is that the crack trajectory is restricted only to the inter-element paths. Furthermore, they have not been able to model microseismic emission due to fault reactivation such as slippage along pre-existing discontinuities.

It is important to note that due to the large amounts of in-situ stresses in geological formations, the main source of significant microseismicity in hydraulic fracturing is sliding of fracture surfaces along each other under frictional contact, rather than tensile fracturing. Moreover, in [71], similar to most of the other works reported on the topic [72], the seismic behaviour has been evaluated through developing relation between the change of the local energy due to localization and the induced seismic moment (event magnitude).

In most of the works reported on microseismic analysis the models fail to simulate the process of mechanical wave propagation through the domain following the energy release at the source/localization area. Therefore, many of the mechanical features of the response such as the attenuation of wave due to the viscous behaviour of poroelastic body and interaction

of the mechanical wave patterns with discontinuities and faults in the process of propagation, and also the wave reflection, scattering, and coalescence phenomenon are all completely ignored.

All these shortcomings can affect the accuracy and reliability of the results provided by similar models (e.g., [72, 73]). Basically, the biggest gap in the topic of induced microseismic/acoustic emission analysis is that the models developed to date concentrate on the source of the generation of wave emission and energy release (still with many assumptions and simplifications) and typically do not simulate the process of transient mechanical wave propagation through a multi-physics discontinuous domain which can raise many challenging computational issues in terms of numerical modeling and solution.

1.8.2 Physics of mechanical waves

An elastic medium shows two types of dynamic responses to external stimulations due to excitation of inertia effects. The first type is vibration response which happens in the form of harmonic motions that comprise low-frequency components/modes. This type of dynamic response occurs under low-frequency loads. The second type is wave propagation which is a dynamic response with high-frequency modes [76], and is induced when there is high-frequency contents in the dynamic excitation. Wave propagation phenomenon falls into two categories, namely, time-harmonic waves and transient waves [74]. In elastodynamics, the general wave type response in displacement field is represented in terms of two wave functions; compressional/pressure and shear waves. The pressure wave function (P wave) is the trace of the symmetric part of the deformation gradient (i.e., volumetric strain) and its physical interpretation involves the volumetric change in elastic body. On the other hand, the shear wave (S wave) is attributed to the antisymmetric part of the deformation gradient which represents the rotation field in the media. It is noted that, unlike the P wave which has a scalar potential, S wave is a vector function.

In wave propagation in saturated porous media, two compressional waves, namely, slow and

fast P waves exist, as theoretically shown by Biot [89]. The slow P wave is highly-attenuated and is attributed to volumetric (i.e., compressional) wave propagation when fluid and solid portions are nearly out of phase [90].

1.8.3 Wave propagation simulation

Although the finite element method is known to be a very effective tool for solution of boundary value problems in mechanics, the accuracy and applicability of conventional finite element approximations in solving the problems that involve particular non-smooth or abruptly changing distributions in spatial (or time) domain is still a challenge.

It is well-known that the conventional finite element method is not appropriate for the solution of wave propagation problems [74]. For the numerical analysis of time harmonic wave propagation the accuracy of the solution descends significantly as the wave number increases resulting in more oscillations per element. In fact, the polynomial shape functions are not able to suitably interpolate the actual variation of the oscillatory distribution of the variables within the element in the case of larger wave numbers (i.e., short wave length). Therefore, finer meshes are required to capture the rapid variation of the parameters inside elements [78].

Firstly, in wave propagation problems with small wave length very fine meshes are required to obtain reasonable results. So, in large scale problems with short waves the numerical solution's time and effort may be prohibitive because of the requirement for very fine meshes in the entire domain of propagation.

Secondly, for transient waves the solution may exhibit severe non-physical spurious oscillations related to the Gibbs phenomenon [79]. These oscillations are generated due to numerical dispersions that come from numerical period elongation and amplitude decay [74]. This phenomenon can significantly affect the propagation velocity and the numerical errors become larger as the

wave travels farther in the domain. Therefore, in the case of the existence of high-frequency components in external stimulation, a very fine mesh is required to capture the variations. The conventional polynomial shape functions used in regular finite elements are not able to interpolate the rapid spatial change in the element, and spurious oscillations are generated due to numerical dispersion.

Spectral methods (see reference [75]) have been developed and used to solve the problem of wave propagation in the frequency domain based on using higher-order polynomials or harmonic interpolation functions. Spectral methods are not practically applicable for complex geometries because of using global basis functions that need to be consistent with the geometry and the boundaries. To remedy this problem, the idea has been extended to the *spectral finite element method*, see [77], in which the interpolations based on trigonometric basis functions are implemented in the element level. However, in spectral finite element method the governing equations are transformed to the frequency domain based on the *Discrete Fourier Transformation* [77] and then the discrete finite element equations are developed using harmonic basis functions and the solution is obtained in the frequency domain. The results are then transformed back to the time domain. These transformations can be computationally expensive and tedious.

The main drawback of the spectral methods in the simulation of localization-induced acoustic emission is that the inducing source of wave propagation (localization) needs to be modeled in the time domain. Consequently, the entire coupled problem needs to be solved concurrently in the time domain. This issue makes the use of spectral methods inefficient and problematic for the problem.

The idea of embedding basis functions, that appear in general analytical solution of a particular problem, as enrichment functions in the conventional FEM interpolations has been first expressed and developed in the pioneering work of Melenk and Babuška [20] as the *partition-of-unity finite element method* (PUFEM). Many new enriched finite element formulations have

been developed and used over past few years in the framework of PUFEM, such as the enriched finite element models that have been proposed for crack modeling (see for example, [26, 61] and also section 1.2.).

To solve wave propagation problems more accurately, the idea of spectral methods and PUFEM have been combined in developing new enriched finite element formulations [78, 79] that can model wave problems in the time domain without the burden of transformation to the frequency domain which is encountered in regular spectral methods.

To solve one-dimensional multi-scale wave propagation problems, Kohno et al. [78] developed a new enriched finite element method by taking advantage of both spectral and partition of unity methods. Harmonic basis functions (that appear in the solution of wave problems) are used in this work to enrich the regular finite element interpolations and make the discretization more likely to more accurately interpolate the variables inside finite elements.

The numerical method proposed in [78] was extended to multi-dimensional wave problems in the work by Ham and Bathe [79]. Through various numerical illustrations they showed that the high-frequency spurious oscillations can be significantly inhibited by including enough number of trigonometric enrichment functions. The possibility of the simulation of wave problems in the time domain can noticeably decrease the high computational costs that are typically involved with the spectral methods that need transformations between the time and frequency domains. Most importantly, the possibility of solving the wave propagation problems in the time domain makes this enriched FEM model very appropriate for the simulation of induced acoustic emission.

The numerical dispersion and error in wave propagation analysis using finite element methods may emanate from both spatial and time discretizations. Although the *Central Difference Method* is still a widely-used time integration scheme in structural dynamics, the use of this

method in wave propagation can lead to inaccurate results for high-frequency modes as the central difference method is a non-dissipative explicit time integration which introduces no numerical damping [83].

A significant amount of effort has been spent in trying to remedy the problem of high-frequency spurious modes in wave propagation using appropriate time integrations. Several dissipative time integration methodologies have been developed to suppress the spurious oscillations using numerical damping, such as explicit time integration proposed by Newmark [80], and Chung and Lee [82]. The problem with using dissipative time integrations is that their ability in suppressing the high-frequency spurious modes can significantly affect the accuracy of low-frequency modes at the same time due to the introduced numerical damping.

Noh and Bathe proposed a new second-order two-step dissipative explicit time integration [83]. In this work it has been demonstrated that using particular values for some explicit time integration parameters, it is possible to suppress high-frequency spurious oscillations and concurrently maintain good accuracy for low-frequency modes in the case of having numerical damping. Nevertheless, suppressing the high-frequency spurious oscillations in the case of sharp waves seems not quite possible with only using dissipative time integrations, since the main cause of spurious oscillations in transient waves is the Gibbs phenomenon which is related to the spatial discretization. Therefore, to have more accurate results in the entire frequency spectrum (i.e., low-frequency as well as high-frequency) the enriched finite element formulations developed for wave propagation problems (e.g., [79]) can be more practical, despite the relatively high computational cost that is typically involved with them. However, the mentioned enriched finite element methods are capable of modeling wave propagation in continuous media.

To the best of the author's knowledge, to date, there is no work reported on using the mentioned enriched finite element models for simulation of wave problems in domains with strong and/or weak discontinuities. One of the main objectives of this PhD research is to develop

a new enriched finite element model for wave propagation in domains with discontinuities. The developed enriched finite element model can then be used for induced acoustic emission simulation in the process of hydraulic stimulation.

1.9 Motivations

The purpose of this research is to develop an improved understanding of the relation between the mechanics of acoustic emissions and fault reactivation during hydraulic stimulation. Throughout the literature there is a limited number of works on the mechanics of acoustic wave emission during HF, most of which fail to investigate the process of transient wave propagation in the media, and instead only focus on relating the amount of energy release at the damaging zone to seismic moment. The seismic event magnitude is estimated using an evaluation of the seismic energy released at the source location and therefore, the entire process of the propagation of seismic wave (shear or pressure waves) through the multi-physics porous discontinuous media is completely ignored.

It is noted that the simulation and analysis of the propagation process is of great importance in obtaining realistic and reliable results for the emission pattern and acoustic behaviour. Therefore, developing new mathematical and computational models that can simulate the entire process, from shear failure to propagation of induced acoustic waves, in a discontinuous porous media seems very necessary and practical to better understand the mechanism of hydraulic stimulation-induced microseismicity. However, some of the main challenges in developing numerical models for the problem are as below:

1. Seismic behaviour is a coupled problem of crack reactivation and induced wave propagation due to reactivation. Therefore, there are two main aspects to this problem that need to be simulated. The mainstream of the solutions for wave propagation simulation is spectral methodologies in frequency domain. However, the other aspect of the problem which is the process of crack reactivation/propagation has nothing to do with the frequency domain, and unlike the wave propagation part, needs to be solely modeled in time domain. To handle this issue, in this PhD research we develop an enriched mixed finite element methodology that can solve the entire coupled problem of fault reactivation-induced wave propagation concurrently

and exclusively in time domain.

2. Due to the dynamic hydro-mechanical coupling of the governing equations, nonlinear interface simulations, and also high-frequency transient components of the response, some numerical stability and convergence issues are expected in the solution process of the problem. These issues stem from inf-sup stability conditions in mixed formulations, numerical dispersions related to the Gibbs phenomenon, and ill-conditioning problems that can arise in enriched and mixed formulations [74].

1.10 Research Objectives and Methodologies

In this section, the research objectives and methodologies to accomplish the objectives are represented.

1: Develop a numerical model for simulation of wave propagation in discontinuous media

The studied domain of the problem is basically a discontinuous media that consists of strong discontinuities (cracks) in the displacement field. The Phantom Node Method (PNM) is used to model multiple fractures in two-dimensional domains independently of the original mesh topology. In regular FEM, spurious period elongation and amplitude decay results in significant errors in the wave pattern and propagation velocity. To remedy this problem, fundamental harmonic basis functions are used to enrich the standard FEM approximation space. In order to model wave propagation in a fractured domain a new numerical method (i.e., PNM-GFEM) that combines a local Partition-of-Unity (i.e., PNM) and global Partition-of-Unity (that includes harmonic wave functions) is developed. This objective is realized in Chapter 2 which is based on the following journal article:

Komijani M., Gracie R., An Enriched Finite Element Model for Wave Propagation in Fractured Media, *Finite Elements in Analysis and Design*, 125: 14-23, 2017.

2: Develop a mixed numerical model for simulation of wave propagation in discontinuous porous media and interface modeling

To simulate slip instability at the interface, and to model normal and frictional interactions between fracture faces, an augmented Lagrange multiplier technique is implemented to simulate the frictional contact behaviour at the interface of discontinuities. The PNM-GFEM method is extended to solve wave propagation problems in porous media. The governing conservation of the linear momentum of the solid-fluid mixture is coupled with the continuity equation for the fluid and solved through a newly developed enriched mixed finite element model called

PNM-GFEM-M. This objective is accomplished in Chapter 3 which is based on the following journal paper:

Komijani M., Gracie R., Enriched Mixed Finite Element Models for Dynamic Analysis of Continuous and Fractured Porous Media, *Computer Methods in Applied Mechanics and Engineering*, 343: 74–99, 2019.

3: Develop computational models for simulation of acoustic emissions induced by fracture reactivation and shear slip instability.

The developed PNM-GFEM-M model is implemented and used to simulate induced acoustic emission propagation due to fracture reactivation under hydraulic stimulation. Since the formations are typically subjected to high in-situ compressive stresses, frictional contact behaviour is modeled to account for the interaction of pre-existing crack faces and their probable slippage and/or propagation. This objective is realized in Chapter 4 which is based on the following journal paper:

Komijani M., Gracie R., Sarvaramini E., Simulation of Induced Acoustic Emission in Fractured Porous Media, *Engineering Fracture Mechanics*, DOI: 10.1016/j.engfracmech.2018.07.028, 2018.

Chapter 2

Enriched finite element models for wave propagation simulation in fractured media

This chapter is based on the following journal article:

Komijani M., Gracie R., An Enriched Finite Element Model for Wave Propagation in Fractured Media, *Finite Elements in Analysis and Design*, 125: 14-23, 2017 [32].

In this journal paper I was the first author and was responsible for the writing of the article; the paper was edited by Dr. Gracie. I also developed the mathematical and computational formulation and the numerical code.

This chapter addresses objective 1 of the thesis.

2.1 Introduction

In this chapter a new numerical method has been developed in the context of enriched finite element methods (FEMs) to analyze wave propagation in fractured media. The method combines the advantages of global enrichment with harmonic functions via the Generalized FEM (GFEM) with the efficacy of the Phantom Node Method (PNM), an eXtended FEM (XFEM) variant, to model cracks independently of the mesh. The GFEM enrichment suppresses the spurious oscillation that appear in regular FEM analysis of transient wave propagations due to numerical dispersion and Gibbs phenomenon. For use in explicit simulations, a mass lumping methodology has been introduced with a critical time step size that is both similar to that of the underlining FEM and independent of the location of the fracture. Through three examples, the developed PNM-GFEM is demonstrated to more accurately model wave propagation in fractured media than either the FEM or the PNM/XFEM.

Wave propagation in fractured media is an important phenomenon in many applications from non-destructive tests to hydraulic fracturing. In many instances, simulations of acoustic emission in fractured media (from the reactivation of existing fractures) are artificially damped and/or the stress fields are smoothed due to the presence of spurious oscillations. These non-physical oscillations are produced ahead and behind emitted waves. The need to smooth stress fields and/or to use artificial damping points to some of the remaining challenges, due to the spurious waves, in traditional FEM-based simulations. There are many examples of the simulation of dynamic fracture using eXtended Finite Element Method (XFEM) [95, 96]. The XFEM and its variants (e.g., the Phantom Node Method [31, 29]) are often the preferred methods for the simulation of the fractures in cases where the path of the fracture is not known *a priori* [26, 27, 97]. In many instances, artificially damping and stress smoothing are required to obtain meaningful and/or stable results. In this article, we revisit the use of the FEM-based methods (such as XFEM) for the simulation of wave propagation problems in fractured media and propose an improved Phantom Node Method without spurious oscillations, based on the Generalized FEM (GFEM) enrichment functions recently proposed [79].

Finite element analysis is an effective tool to investigate transient initial boundary value problems. However, the piecewise continuous polynomials used to interpolate the unknown functions have been found to be inadequate in the problems where there are sudden or abrupt changes in the solution. For instance, in the case of transient wave propagation, FEM solution often contains spurious oscillations. These non-physical oscillations degrade the results, including the wave propagation velocity, which is important in application such a microseismic wave simulation, where the waves travel long distances.

The origin of these non-physical oscillations is related to the Gibbs phenomenon. However, in fractured bodies the effect of the spurious oscillations can be more significant because of the interaction of wave pattern with cracks and also interaction/superposition of the primary emitted waves with secondary waves reflected from discontinuities (e.g., the cracks). The origin of spurious oscillations, therefore, do not stem directly from the coarseness of the meshes in explicit or implicit simulations. In the case of high-frequency transient waves, the spurious oscillations observed in regular FE models cannot be effectively removed by refining the mesh; mesh refinement does affect the frequency of the spurious oscillations ahead or behind the wave front. It is worth mentioning that mesh refinement can be effective in decreasing the numerical dispersions and error in the case of time-harmonic waves (but not high-frequency transient waves)[79].

This problem has in part motivated the development of the spectral element method ([98], [99]) and the spectral finite element method ([100], [101]), which overcome the issue of spurious oscillations through the use of harmonic basis functions. Spectral finite element models are formulated in the frequency domain and therefore requires a transformation of the governing equations to the frequency domain. The equations are then solved in the frequency domain, and the results are then back transformed to the time domain. This makes the spectral finite element procedure less practical for problems that need to be solved in the time domain, such as dynamic crack propagation problems.

An alternative, yet related approach, to the spectral element method was proposed in [78],

where an enriched harmonic and conventional low-order polynomials interpolations are used to model multi-scale wave propagation in one-dimensional problem. The general idea of embedding appropriate basis functions, with characteristics that appear in the solution of the problem, as enrichments to the traditional finite element interpolations was established in the pioneering work of Melenk and Babuška [20] on the Partition of Unity Method (PUM). Based on the general approach of the PUM, Ham and Bathe [79] extended the approach in [78] to solve the problem of time-harmonic and transient wave propagation in multiple dimensions; it was demonstrated that the spurious oscillations that appear with the conventional FEM can be effectively suppressed by the proposed enriched FEM in the simulation of wave propagation in continuous domains. To date these enriched finite element methods have not been applied to problems involving discontinuous domains that contain arbitrary cracks.

In Song et al. [29] an XFEM variant, the Phantom Node Method (PNM), was proposed to model discontinuities and is essentially the same as the earlier method proposed by Hansbo and Hansbo [31]. In the PNM, cracks are treated by reformulating elements which contain a fracture as two superimposed elements with additional nodes, called Phantom Nodes. Each of the superimposed elements is used to model a different side of the original fractured element, leading to a discontinuous approximation. The advantage of the Phantom Node formulation over that of the original XFEM is that an implementation of the PNM requires fewer modifications to an existing FEM code than a comparable XFEM implementation; however, in principle the two formulations should yield equivalent results for small displacement analysis. Despite the numerous publications on XFEM and its variants (including GFEM), there is no work in the published literature addressing the spurious oscillation from numerical dispersion that appear in the concurrent simulations of wave propagation and fracture. Here we study a Phantom Node Method, enhanced by a global enrichment using harmonic basis functions, to more effectively simulation wave propagation in fractured media.

Due to the high strain-rates that generally accompany dynamic fracture explicit time integration is often preferred. Therefore, a mass-lumping strategy is presented for the GFEM

enriched Phantom Node Method proposed here, so that the proposed method can be applied efficiently.

A note on terminology: the distinction between the XFEM and the GFEM is ambiguous in the literature; at their core, both methods are identical as they involve using local and/or global enrichment of a finite element basis [27]. In this article, the term XFEM will be used to refer to a FEM locally enriched with the Heaviside step function to model the discontinuities of fractures and so would include the GFEM model of Gupta et al. [28]. The term GFEM will be reserved for global enrichment using harmonic functions as proposed in [79].

2.2 Mathematical formulation

2.2.1 Governing equations

Consider a two-dimensional elastic medium, Ω, defined in terms of a Cartesian coordinate system O_{xy}. Let $u_x(x, y, t)$ and $u_y(x, y, t)$ be the displacement components in x and y directions, respectively, as a function of time, t. Assuming small displacements, the symmetric strain-displacement relations are

$$\varepsilon_{xx} = u_{x,x} \qquad \varepsilon_{yy} = u_{y,y} \qquad \gamma_{xy} = u_{x,y} + u_{y,x} \tag{2.1}$$

The constitutive equations can be written in Voigt notation as:

$$\begin{bmatrix} \sigma_{xx} \\ \sigma_{yy} \\ \sigma_{xy} \end{bmatrix} = \begin{bmatrix} C_{11} & C_{12} & 0 \\ C_{21} & C_{22} & 0 \\ 0 & 0 & C_{33} \end{bmatrix} \begin{bmatrix} \varepsilon_{xx} \\ \varepsilon_{yy} \\ \gamma_{xy} \end{bmatrix} \tag{2.2}$$

where σ_{xx}, σ_{yy}, and σ_{xy} are the component of the Cauchy stress tensor, and C_{11} through C_{33} are the elastic coefficients.

The variational form of the governing partial differential equations are developed from Hamilton's principle, i.e.,

$$\delta \int_t (K - H + R) dt = 0 \tag{2.3}$$

where δH, δK, and δR are the variation of the elastic strain energy, the kinetic energy, and the work done by the external loads, respectively:

$$\delta H = \int_\Omega \boldsymbol{\sigma} : \delta\boldsymbol{\varepsilon} d\Omega \tag{2.4}$$

$$\delta K = \int_{\Omega} \rho \ddot{\boldsymbol{u}} \cdot \delta \dot{\boldsymbol{u}} d\Omega \tag{2.5}$$

$$\delta R = \int_{\Omega} \delta \boldsymbol{u} \cdot \rho \boldsymbol{b} d\Omega + \int_{\Gamma} \delta \boldsymbol{u} \cdot \bar{\boldsymbol{t}} d\Gamma \tag{2.6}$$

where $\boldsymbol{\sigma}$ is the Cauchy stress tensor, $\boldsymbol{\varepsilon}$ is the symmetric strain tensor, $\boldsymbol{u}$ is the displacement vector, ρ is density, $\boldsymbol{b}$ is the body force vector, and $\bar{\boldsymbol{t}}$ is the applied traction vector. As for the integration domains, Ω indicates the overall volume of the system and Γ is the portion of the boundary over which the traction is imposed, i.e., the Neumann boundary.

Substituting (4.1) and (4.2) into the variational form of the energy equation (2.3), the weak formulation of the governing motion equations can be obtained as:

$$\int_{\Omega} \big(\left[C_{11} u_{x,x} + C_{12} u_{y,y} \right] \delta u_{x,x} + \left[C_{33} (u_{x,y} + u_{y,x}) \right] \delta U_{x,y} \big) d\Omega =$$

$$= \int_{\Omega} (-\rho \ddot{u_x} + \rho b_x) \delta u_x d\Omega + \int_{\Gamma} (\bar{t_x}) \delta u_x d\Gamma \tag{2.7}$$

$$\int_{\Omega} \big(\left[C_{21} u_{x,x} + C_{22} u_{y,y} \right] \delta u_{y,y} + \left[C_{33} (u_{x,y} + u_{y,x}) \right] \delta u_{y,x} \big) d\Omega =$$

$$= \int_{\Omega} (-\rho \ddot{u_y} + \rho b_y) \delta u_y d\Omega + \int_{\Gamma} (\bar{t_y}) \delta u_y d\Gamma \tag{2.8}$$

2.2.2 Element interpolation using the Generalized and Phantom Node Methods

The GFEM interpolation of the displacement field [79] within the continuous elements for wave propagation analysis is

$$\boldsymbol{u}(x,y,t) = \sum_I N_I \Big(\boldsymbol{u}_{I(0,0)} + \sum_{k_x=1}^{n} [cos(\frac{2\pi k_x x}{\Lambda_x}) \boldsymbol{u}^{C_x}_{I(k_x,0)} + sin(\frac{2\pi k_x x}{\Lambda_x}) \boldsymbol{u}^{S_x}_{I(k_x,0)}] +$$

$$\sum_{k_y=1}^{m} [cos(\frac{2\pi k_y y}{\Lambda_y}) \boldsymbol{u}^{C_y}_{I(0,k_y)} + sin(\frac{2\pi k_y y}{\Lambda_y}) \boldsymbol{u}^{S_y}_{I(0,k_y)}] +$$

$$\sum_{k_x=1}^{n} \sum_{k_y=1}^{m} [cos(\frac{2\pi k_x x}{\Lambda_x} + \frac{2\pi k_y y}{\Lambda_y}) \boldsymbol{u}^{C+}_{I(k_x,k_y)} + sin(\frac{2\pi k_x x}{\Lambda_x} + \frac{2\pi k_y y}{\Lambda_y}) \boldsymbol{u}^{S+}_{I(k_x,k_y)} + \tag{2.9}$$

$$cos(\frac{2\pi k_x x}{\Lambda_x} - \frac{2\pi k_y y}{\Lambda_y}) \boldsymbol{u}^{C-}_{I(k_x,k_y)} + sin(\frac{2\pi k_x x}{\Lambda_x} - \frac{2\pi k_y y}{\Lambda_y}) \boldsymbol{u}^{S-}_{I(k_x,k_y)}] \Big)$$

where N_I are the regular FE shape functions, $\boldsymbol{u}^{\gamma}_{I(k_x,k_y)}$ with the corresponding superscript are the nodal degree of freedom associated with local node number I, n and m are the cutoff numbers for enrichment functions in x and y directions, respectively, and Λ_x and Λ_y are wavelengths, which are assumed to be equal to the element sizes in x and y directions, respectively. It is noted that the superscripts have been used in the above formulation to refer to degrees of freedom associated to each enrichment function.

The above enriched finite element interpolation can be represented in a more compact form as:

$$\boldsymbol{U}(x,y,t) = \sum_I \Big(N_I \boldsymbol{u}_{I(0,0)} + \sum_{k_x=1}^{n} [N_I \phi^{C_x}_{(k_x,0)} \boldsymbol{u}^{C_x}_{I(k_x,0)} + N_I \phi^{S_x}_{(k_x,0)} \boldsymbol{u}^{S_x}_{I(k_x,0)}] +$$

$$\sum_{k_y=1}^{m} [N_I \phi^{C_y}_{(0,k_y)} \boldsymbol{u}^{C_y}_{I(0,k_y)} + N_I \phi^{S_y}_{(0,k_y)} \boldsymbol{u}^{S_y}_{I(0,k_y)}] +$$

$$\sum_{k_x=1}^{n} \sum_{k_y=1}^{m} [N_I \phi^{C+}_{(k_x,k_y)} \boldsymbol{u}^{C+}_{I(k_x,k_y)} + N_I \phi^{S+}_{(k_x,k_y)} \boldsymbol{u}^{S+}_{I(k_x,k_y)} + \tag{2.10}$$

$$N_I \phi^{C-}_{(k_x,k_y)} \boldsymbol{u}^{C-}_{I(k_x,k_y)} + N_I \phi^{S-}_{(k_x,k_y)} \boldsymbol{u}^{S-}_{I(k_x,k_y)}] \Big)$$

where $\phi^{\gamma}_{(k_x,k_y)}$ with the corresponding superscript represents the trigonometric enriched basis functions shown in (2.9).

To model wave propagation in discontinuous media, the Phantom Node Method [31, 29] is combined with the GFEM approximation (3.16). In the PNM approach, any element containing a discontinuity is replaced by two superimposed continuous elements with real and phantom nodes [29]. Let the signed distance function $f(x, y)$ define the surface of discontinuity, such that $f(x, y) = 0$ specifies the discontinuous surface.

Taking advantage of both the GFEM and the PNM, the displacement field for cracked element is approximated by

$$\begin{aligned}
\boldsymbol{u}(x,y,t) = H(-f(x,y)) \sum_{I\in S_1} \Big(& \psi_{I(0,0)}\boldsymbol{u}_{I(0,0)} + \sum_{k_x=1}^{n} [\psi^{C_x}_{I(k_x,0)}\boldsymbol{u}^{C_x}_{I(k_x,0)} + \psi^{S_x}_{I(k_x,0)}\boldsymbol{u}^{S_x}_{I(k_x,0)}] + \\
& \sum_{k_y=1}^{m} [\psi^{C_y}_{I(0,k_y)}\boldsymbol{u}^{C_y}_{I(0,k_y)} + \psi^{S_y}_{I(0,k_y)}\boldsymbol{u}^{S_y}_{I(0,k_y)}] + \\
& \sum_{k_x=1}^{n}\sum_{k_y=1}^{m} [\psi^{C+}_{I(k_x,k_y)}\boldsymbol{u}^{C+}_{I(k_x,k_y)} + \psi^{S+}_{I(k_x,k_y)}\boldsymbol{u}^{S+}_{I(k_x,k_y)} + \psi^{C-}_{I(k_x,k_y)}\boldsymbol{u}^{C-}_{I(k_x,k_y)} + \psi^{S-}_{I(k_x,k_y)}\boldsymbol{u}^{S-}_{I(k_x,k_y)}] \Big) + \\
H(f(x,y)) \sum_{I\in S_2} \Big(& \psi_{I(0,0)}\boldsymbol{u}_{I(0,0)} + \sum_{k_x=1}^{n} [\psi^{C_x}_{I(k_x,0)}\boldsymbol{u}^{C_x}_{I(k_x,0)} + \psi^{S_x}_{I(k_x,0)}\boldsymbol{u}^{S_x}_{I(k_x,0)}] + \\
& \sum_{k_y=1}^{m} [\psi^{C_y}_{I(0,k_y)}\boldsymbol{u}^{C_y}_{I(0,k_y)} + \psi^{S_y}_{I(0,k_y)}\boldsymbol{u}^{S_y}_{I(0,k_y)}] + \\
& \sum_{k_x=1}^{n}\sum_{k_y=1}^{m} [\psi^{C+}_{I(k_x,k_y)}\boldsymbol{u}^{C+}_{I(k_x,k_y)} + \psi^{S+}_{I(k_x,k_y)}\boldsymbol{u}^{S+}_{I(k_x,k_y)} + \psi^{C-}_{I(k_x,k_y)}\boldsymbol{u}^{C-}_{I(k_x,k_y)} + \psi^{S-}_{I(k_x,k_y)}\boldsymbol{u}^{S-}_{I(k_x,k_y)}] \Big)
\end{aligned} \tag{2.11}$$

where $\psi_{I(0,0)} = N_I$ and $\psi^{\gamma}_{I(k_x,k_y)} = N_I\phi^{\gamma}_{(k_x,k_y)}$, and $H(\cdot)$ is the Heaviside function. S_1 and S_2 are the set of nodes associated with each of the two superimposed elements; each of the two superimposed elements contain original real nodes and phantom nodes. In the context of GFEM, both the real and phantom nodes have conventional and enriched degrees of freedom.

The discontinuous element interpolation (3.17) can be written in more compact matrix form

as

$$u_x(x,y,t) = H(-f(x,y)) \sum_{I \in S_1} \Big(\boldsymbol{\psi}_I(x,y) \boldsymbol{u}_{Ix}(t) \Big) + H(f(x,y)) \sum_{I \in S_2} \Big(\boldsymbol{\psi}_I(x,y) \boldsymbol{u}_{Ix}(t) \Big) \tag{2.12}$$

$$u_y(x,y,t) = H(-f(x,y)) \sum_{I \in S_1} \Big(\boldsymbol{\psi}_I(x,y) \boldsymbol{u}_{Iy}(t) \Big) + H(f(x,y)) \sum_{I \in S_2} \Big(\boldsymbol{\psi}_I(x,y) \boldsymbol{u}_{Iy}(t) \Big) \tag{2.13}$$

where $\boldsymbol{\psi}_I$ is the set of conventional and enriched basis functions for node I given by

$$\boldsymbol{\psi}_I = \left[\begin{array}{cccc} \psi_{I(0,0)} & \psi^{C_x}_{I(1,0)} & ... & \psi^{S-}_{I(n,m)} \end{array} \right] \tag{2.14}$$

and $\mathbf{u}_{Ix}$ and $\mathbf{u}_{Iy}$ are the vectors of corresponding conventional and enriched degrees of freedom for node I in the x and y directions, respectively, i.e.,

$$\boldsymbol{u}^{\top}_{Ix} = [u_{Ix(0,0)}, u^{C_x}_{Ix(1,0)}, ..., u^{S-}_{Ix(n,m)}] \tag{2.15}$$

$$\boldsymbol{u}^{\top}_{Iy} = [u_{Iy(0,0)}, u^{C_x}_{Iy(1,0)}, ..., u^{S-}_{Iy(n,m)}] \tag{2.16}$$

In total, node I has $2(1+2n)(1+2m)$ degrees of freedom. The most appropriate choice for m and n depends on the amount of high-frequency oscillations that appear in each problem. In transient problems with sharper wave fronts, more enrichments are required. Beyond the computational cost of more DOFs, ill-conditioning also becomes more problematic as the number of enrichements is increased. Based on our investigations up to this point, the most effective computation schemes are achieved using $n = m = 1$ or 2.

2.3 Semi-discrete Equations

The element level semi-discretized enriched finite element equations can be developed by substituting the PNM-GFEM approximation (2.12), and the virtual displacements $\delta u_x = \psi_I$ and $\delta u_y = \psi_I$ into the variational form of the governing equations of motion (2.7-2.8), giving:

$$\sum_{J=1}^{n_{node}} \left([M^e]_{IJ}^{11} \ddot{\mathbf{u}}_{Jx}^e + [M^e]_{IJ}^{12} \ddot{\mathbf{u}}_{Jy}^e + [K^e]_{IJ}^{11} \mathbf{u}_{Jx}^e + [K^e]_{IJ}^{12} \mathbf{u}_{Jy}^e \right) = \mathbf{F}_{Ix}^e, \quad (I = 1, ..., n_{node}) \tag{2.17}$$

$$\sum_{J=1}^{n_{node}} \left([M^e]_{IJ}^{21} \ddot{\mathbf{u}}_{Jx}^e + [M^e]_{IJ}^{22} \ddot{\mathbf{u}}_{Jy}^e + [K^e]_{IJ}^{21} \mathbf{u}_{Jx}^e + [K^e]_{IJ}^{22} \mathbf{u}_{Jy}^e \right) = \mathbf{F}_{Iy}^e \quad (I = 1, ..., n_{node}) \tag{2.18}$$

where n_{node} is the number of nodes in each of the two superposed elements 1 and 2, and includes both original real and phantom nodes. It is noted that for the cracked elements, the numerical integration is performed separately over the active areas of each of the two superposed elements. To evaluate the finite element integrals a sub-domain integration scheme is employed [26]. Due to the introduction of the Heaviside function in the PNM-GFEM approximation, it is only necessary to integrate over the active portion of each superimposed element. Let A_1 and A_2 denote the mutually exclusive activated areas (where the displacement approximation is not equal to zero) of superposed elements 1 and 2, respectively. If A is the total area of the original element then $A = A_1 + A_2$.

In an element crossed by a crack, the definitions of $[M^e]_{IJ}$, $[K^e]_{IJ}$, $\mathbf{F}_{Ix}^e$, and $\mathbf{F}_{Iy}^e$ in (2.17) and (2.18) are as follows, for each of the superimposed elements 1 and 2:

$$[M^e]_{IJ}^{11} = \int_{A_e} \rho \boldsymbol{\psi}_I^\top \boldsymbol{\psi}_J d\Omega, \quad [M^e]_{IJ}^{12} = [0],$$

$$[M^e]_{IJ}^{21} = [0], \quad [M^e]_{IJ}^{22} = \int_{A_e} \rho \boldsymbol{\psi}_I^\top \boldsymbol{\psi}_J d\Omega \tag{2.19}$$

$$[K^e]^{11}_{IJ} = \int_{A_e} \Big(C_{11}(\boldsymbol{\psi}^\top_I)_{,x}(\boldsymbol{\psi}_J)_{,x} + C_{33}(\boldsymbol{\psi}^\top_I)_{,y}(\boldsymbol{\psi}_J)_{,y} \Big) d\Omega, \tag{2.20}$$

$$[K^e]^{12}_{IJ} = \int_{A_e} \Big(C_{12}(\boldsymbol{\psi}^\top_I)_{,x}(\boldsymbol{\psi}_J)_{,y} + C_{33}(\boldsymbol{\psi}^\top_I)_{,y}(\boldsymbol{\psi}_J)_{,x} \Big) d\Omega, \tag{2.21}$$

$$[K^e]^{21}_{IJ} = \int_{A_e} \Big(C_{21}(\boldsymbol{\psi}^\top_I)_{,y}(\boldsymbol{\psi}_J)_{,x} + C_{33}(\boldsymbol{\psi}^\top_I)_{,x}(\boldsymbol{\psi}_J)_{,y} \Big) d\Omega, \tag{2.22}$$

$$[K^e]^{22}_{IJ} = \int_{A_e} \Big(C_{22}(\boldsymbol{\psi}^\top_I)_{,y}(\boldsymbol{\psi}_J)_{,y} + C_{33}(\boldsymbol{\psi}^\top_I)_{,x}(\boldsymbol{\psi}_J)_{,x} \Big) d\Omega, \tag{2.23}$$

$$\mathbf{F}^e_{Ix} = \int_{A_e} \Big(\rho(b_x)\boldsymbol{\psi}^\top_I \Big) d\Omega + \int_{s_e} \Big(\bar{t}_x \boldsymbol{\psi}^\top_I \Big) d\Gamma, \tag{2.24}$$

$$\mathbf{F}^e_{Iy} = \int_{A_e} \Big(\rho(b_y)\boldsymbol{\psi}^\top_I \Big) d\Omega + \int_{s_e} \Big(\bar{t}_y \boldsymbol{\psi}^\top_I \Big) d\Gamma, \tag{2.25}$$

where e is either 1 or 2 for the superimposed elements one and two, respectively, and s_e is the portion of superimposed element e on the traction boundary Γ.

2.4 Mass Lumping Technique

In wave propagation problems short-term transient and high strain rate phenomena are often of interest. In such applications, explicit time integration methods are typically preferred over implicit schemes, given the comparatively less computational cost and memory requirement. Hence, developing an appropriate mass lumping strategy for the present enriched finite element method is important for practical applications. Enriched finite element methods introduce additional mathematical degrees of freedom at each node and so it is not possible to distribute the entire mass of the element to the element nodes as is done with conventional finite elements. Hence, the straight forward diagonal mass lumping is not optimal for GFEM.

Few works have discussed the development of a lumped mass matrix for enriched finite element models. Among these works, Menouillard et al. [85] introduced a lumped mass matrix for the elements enriched by the step function in the context of the eXtended Finite Element Method, in which the lumped mass matrix is developed such that an exact representation of the kinetic energy is conserved under rigid body motion. It was shown that using their lumped mass matrix, the critical time step does not tend to zero as the discontinuity gets close to the boundaries of the cracked element. Furthermore, the aforementioned lumped mass matrix yields an XFEM with a critical time step that is of the same order of magnitude as that for the FEM. In the present study, a similar methodology is adopted to develop a lumped mass matrix for the PNM-GFEM model.

The coefficients of the lumped mass matrix are defined such that the discrete kinetic energy associated with a velocity field proportional to each enrichment function is exactly reproduced. We wish to derive an expression for the lumped mass for enriched degrees of freedom $\mathbf{u}^{\gamma}_{I(k_x,k_y)}$ associated with enrichment $\psi^{\gamma}_{(k_x,k_y)}$. To simplify the discussion we will derive the lumped mass coefficients for the x-direction only. The components for the y-direction are readily derived using a similar process and furthermore leads to the same lumped mass coefficient.

Consider the following velocity field defined over a bilinear element

$$\dot{u}_x = \bar{v}_x \phi^{\gamma}_{(k_x,k_y)} \tag{2.26}$$

$\bar{v}_x$ is the enriched degree of freedom corresponding to a particular enrichment function. The exact kinetic energy of the element is

$$T = \frac{1}{2}\int_{Ae} \rho[\bar{v}_x \phi^{\gamma}_{(k_x,k_y)}]^2 d\Omega \tag{2.27}$$

where A_e is the active part of the superimposed element in the case of an element cut by the crack.

An enriched approximation of the form (2.12) exactly interpolates (2.26) when $\dot{\mathbf{u}}^{\gamma}_{x(k_x,k_y)} = \bar{v}_x \left[1,1,1,1\right]^{\top}$ (for a four-node quadrilateral element) and all other degrees of freedom associated to other enriched basis functions are zero. In such a case the discrete kinetic energy computed using a lumped mass matrix would be

$$T^h = \frac{1}{2}(m^{\gamma}_{1(k_x,k_y)} + m^{\gamma}_{2(k_x,k_y)} + m^{\gamma}_{3(k_x,k_y)} + m^{\gamma}_{4(k_x,k_y)})\bar{v}_x^2 \tag{2.28}$$

where $m^{\gamma}_{I(k_x,k_y)}$, $I = 1..4$, are the coefficients of the the lumped mass matrix associated with enriched degree of freedom $u^{\gamma}_{Ix(k_x,k_y)}$. To find $m^{\gamma}_{I(k_x,k_y)}$, the kinetic energies of the continuous and discrete systems are equated, i.e., we set (2.28) equal to (2.27), giving

$$\sum_{I=1}^{4} m^{\gamma}_{I(k_x,k_y)} = \int_{Ae} \rho[\boldsymbol{\phi}^{\gamma}_{(k_x,k_y)}]^2 d\Omega \tag{2.29}$$

or equivalently

$$m^{\gamma}_{I(k_x,k_y)} = \alpha_I \int_{Ae} \rho[\phi^{\gamma}_{(k_x,k_y)}]^2 d\Omega, \;\; \sum_{I=1}^{4} \alpha_I = 1 \tag{2.30}$$

where α_I is a weighting coefficient that determines what percentage of the *mass* is assigned to node I. The last question to be answered is how to best distribute the mass to the four nodes of the element. The simplest way is to assume that the mass is distributed equally to each node

($\alpha_I = 1/4$). A more fair distribution is adopted in which the weighting coefficient is given by

$$\alpha_I = \frac{1}{A}\int_A N_I d\Omega \tag{2.31}$$

where the integral is over the whole element area and not just over the active part of the element as in (2.29) and (2.30). It is noted that when the density ρ of the element is constant and when adjacent sides of the element are perpendicular then

$$m^{\gamma}_{I(k_x,k_y)} = \frac{\rho}{4}\int_{Ae} [\phi^{\gamma}_{(k_x,k_y)}]^2 d\Omega \tag{2.32}$$

It is noted that while (2.32) was derived for the x-direction degrees of freedom, it can also be shown to be valid for the y-direction degrees of freedom.

2.5 Results and discussion

In this section, the developed enriched finite element method is implemented to solve different types of transient wave propagation problems in discontinuous domains. The studied domain is a $1.5m \times 1.0m$ media in a state of plane-stress and is made of a material with $\rho = 8000kg/m^3$, $E = 200GPa$, and $\nu = 0.3$, unless stated otherwise.

2.5.1 Benchmark study-Impact problem

The problem of an impact simulated by prescribing a constant velocity boundary condition to the edge $x = 0$ is known to be a good benchmark problem to examine the accuracy of a developed finite element method [79]. To examine the power of the enriched finite element model of this work to solve transient wave propagation in a fractured domain, a mesh of 30×20 bilinear elements is considered. A tilted crack of length $0.2236m$ centered in the middle of the plate and at the angle of $63.5°$ with respect to the horizontal direction is modeled. Figure 2.1 shows the configuration of the domain along with the discontinuity. In this figure the velocity profile shown was obtained using PNM-GFEM ($n = 2$ and $m = 0$) at time $t = 72.8\mu s$. As seen, in this figure, the wave front has not yet reached the face of the discontinuity, and therefore, the result is the same as for the continuous domain evaluated in [79]. It is noted that the high frequency spurious oscillations that are well-known to appear ahead of the wave front in regular FE/PNM analysis have been significantly inhibited by including the enriched trigonometric basis functions. The result of conventional finite element analysis of the problem at $t = 184\mu s$ is depicted in Figure 2.2. Due to the interaction of the wave and the crack, a discontinuous velocity profile is obtained. Also, the reflected wave from the contact-free crack face is noticeable in the snap shot. As can be seen, very strong non-physical oscillations appear ahead of both primary and reflected wave fronts. The result of PNM-GFEM analysis of this problem is shown in Figures 2.3 and 2.4 with cutoff numbers $n = 1$ and $n = 3$, respectively. Comparing the results it is clear that, the more enriched basis functions that are considered, the smaller the magnitude of the spurious oscillations. Using a cutoff number $n = 3$, the

Table 2.1: A normalized error estimation (e_{L2}) for PNM-GFEM for various values of the cutoff number.

Cutoff number	Normalized error (e_{L2})(%)
0	10.03
1	3.826
2	3.084
3	2.05

non-physical oscillations are dramatically suppressed throughout the domain.

The reduction in the spurious oscillations in the wave patterns of the PNM-GFEM with increasing the cutoff number is illustrated in Figures 2.5 through 2.8, which show the velocty field as the wave is reflected from the crack surface. The expected solution is a step function wave front in the velocity field. As seen in these figures, the non-physical spurious oscillations (numerical dispersion) in both primary emitted and reflected waves are suppressed more and more effectively, as the cutoff number increases. Figure 2.9 presents the convergence of PNM-GFEM solution to step-function-type transient wave propagation response of the impact problem. In this figure, the vertical axis shows the percent error in velocity magnitude (the difference between the obtained result and the benchmark step-function-type response) at the peak of the highest amplitude oscillation. As seen, the error due to the non-physical spurious oscillations decreases with an increase in the cut-off number. To further illustrate the convergence of the PNM-GFEM, Table 2.1 reports estimates of the normalized ($L2$) error for various values of the cutoff number, in which a very fine meshed PNM-GFEM and a cut-off number of 4 is used as a reference solution. As seen, the numerical error decreases upon increasing the number of enriched basis functions.

2.5.2 Wave Propagation - Single Crack Example

The problem of wave propagation induced by a sinusoidal stimulation at the free end of a plate containing a vertical crack of length $0.2m$ along $x = 0.75m$ is examined by considering a 40×20 4-node element mesh. A prescribed displacement is applied to the boundary $x = 0$ as below:

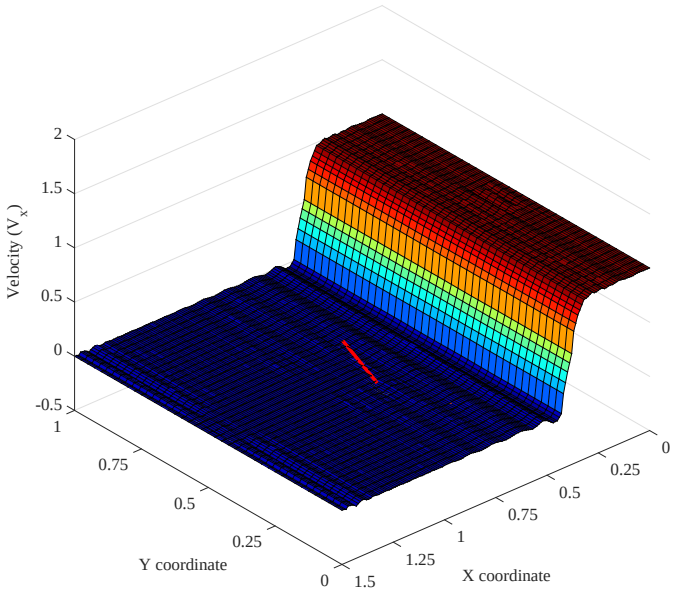

Fig. 2.1: Solution of impact of a cracked plate (x-velocity) at $t = 72.8\mu s$, using PNM-GFEM with cutoff number $n = 2$, before the wave front hits the crack.

$$\bar{u}_x(t) = \begin{cases} 0.03\sin(\frac{\pi}{2\tau}t)[m] & \text{if } t \leqslant 2\tau; \\ 0 & \text{if } t > 2\tau. \end{cases} \tag{2.33}$$

where $\tau = 10^{-5}$ s.

Figure 2.10 illustrates the domain, the location of the crack, and the wave pattern at $t = 70\mu s$ before the wave front hits the crack. Figures 2.11 and 2.12 illustrate the x-displacement field at time $t = 188\mu s$ calculated using the PNM and PNM-GFEM, respectively. By comparing these two figures it is apparent that the high frequency spurious oscillations which appear in the PNM results are significantly reduced by using the PNM-GFEM with $n = 1, m = 0$. In the PNM results, significant high-frequency spurious oscillations appear ahead of the primary wave that propagates around the crack and from the wave reflected from the crack surface. These spurious oscillations pollute the PNM results. In contrast, in the PNM-GFEM results the non-physical oscillations are suppressed, leading to more accurate solutions. The mentioned non-physical

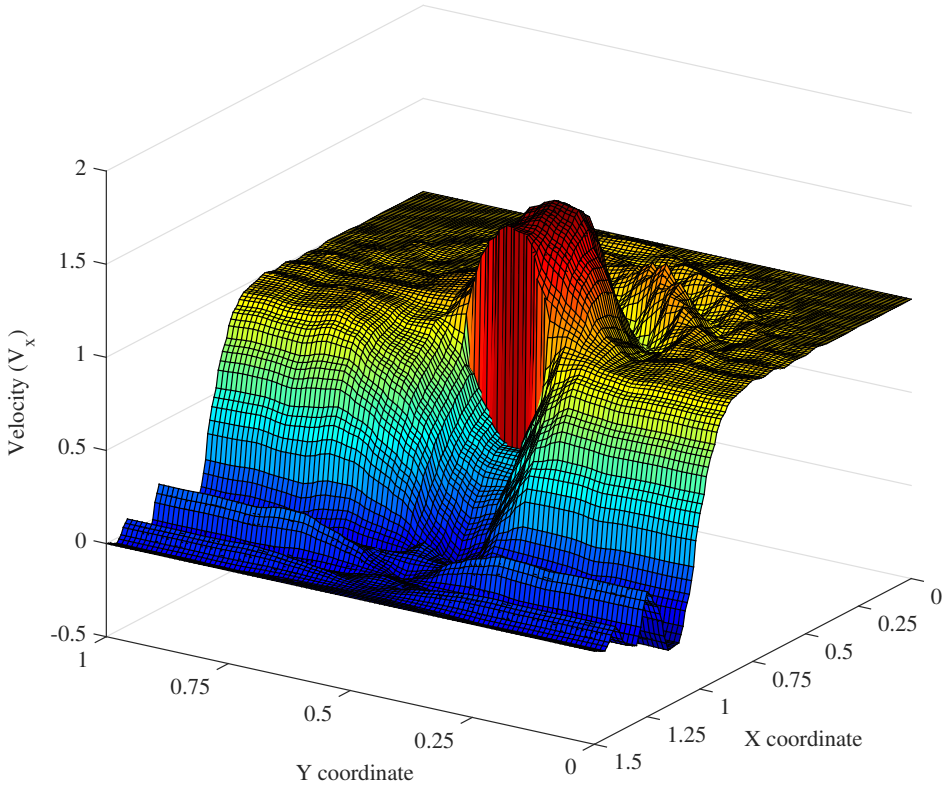

Fig. 2.2: Solution of impact of a cracked plate (x-velocity) at $t = 184\mu s$, using conventional PNM.

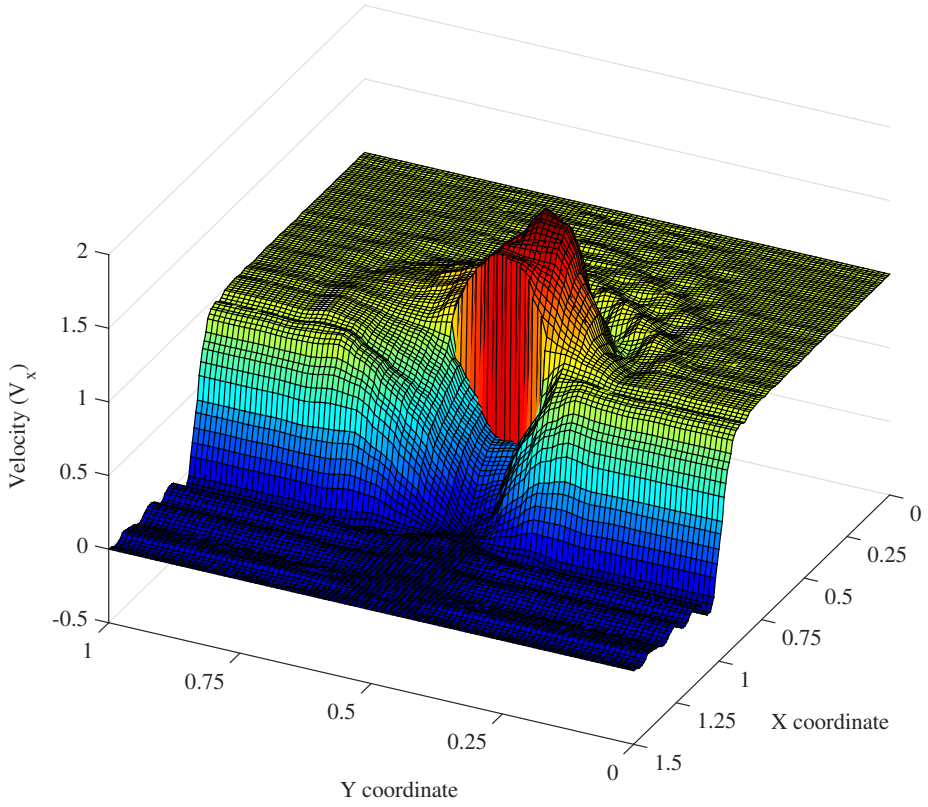

Fig. 2.3: Solution of impact of a cracked plate (x-velocity) at $t = 184\mu s$, using PNM-GFEM with $n = 1$.

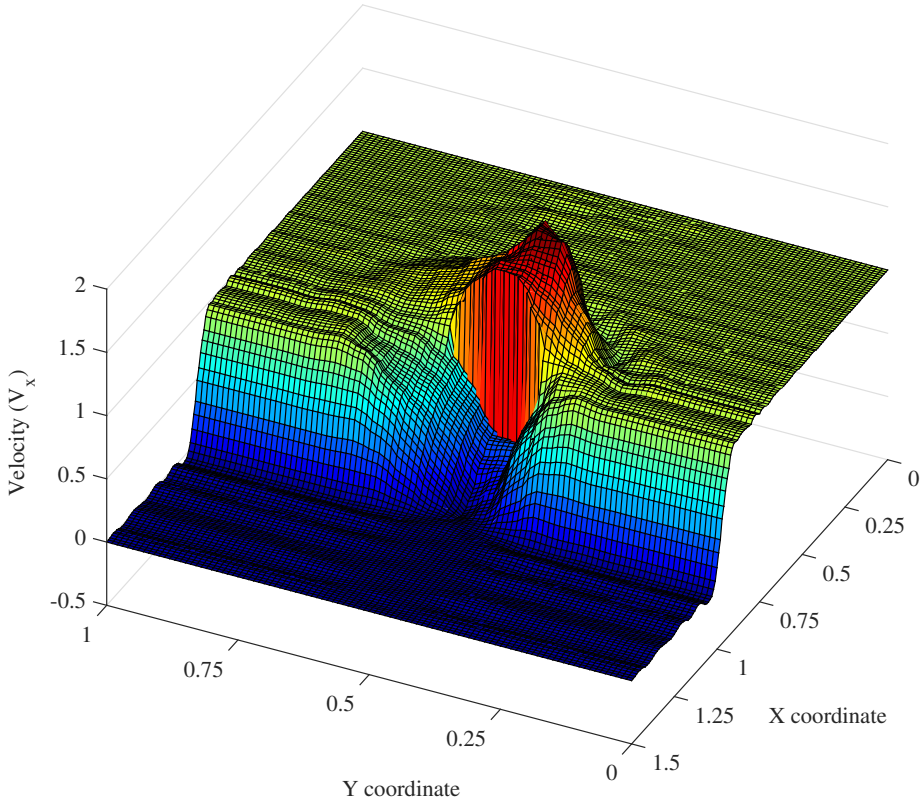

Fig. 2.4: Solution of impact of a cracked plate (x-velocity) at $t = 184\mu s$, using PNM-GFEM with a cutoff number $n = 3$.

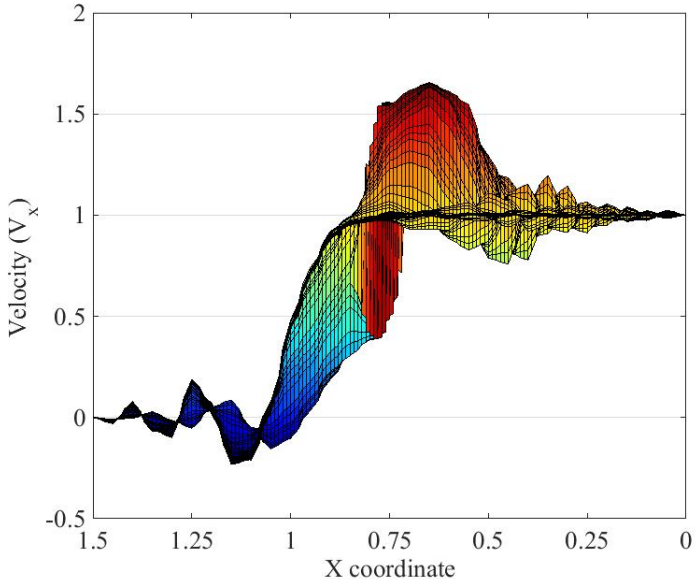

Fig. 2.5: Illustration of high-frequency spurious oscillations in wave pattern obtained using conventional PNM.

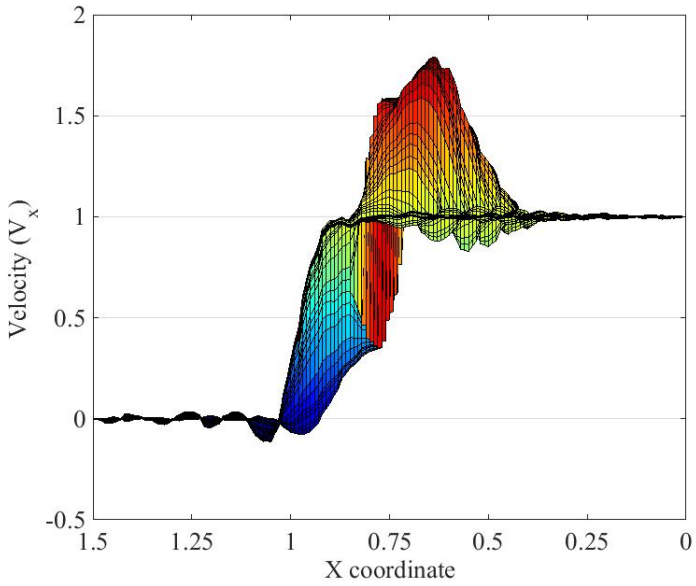

Fig. 2.6: Illustration of the convergence process of the PNM-GFEM to oscillation-free results using cutoff number $n = 1$.

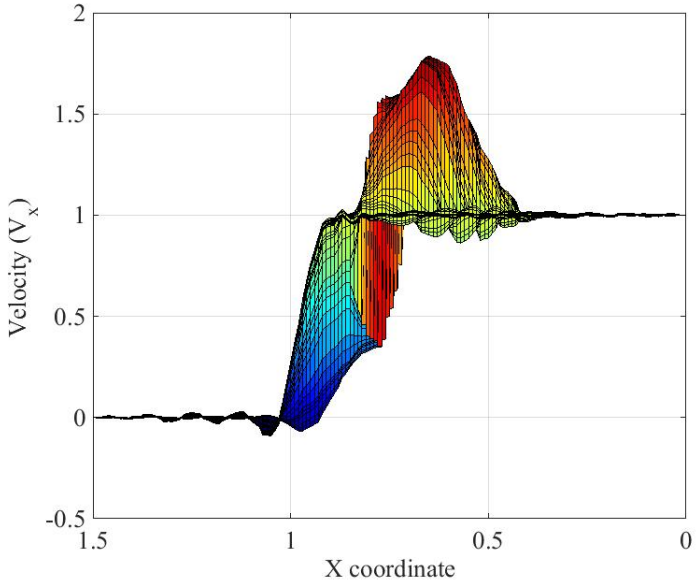

Fig. 2.7: Illustration of the convergence process of the PNM-GFEM to oscillation-free results using cutoff number $n = 2$.

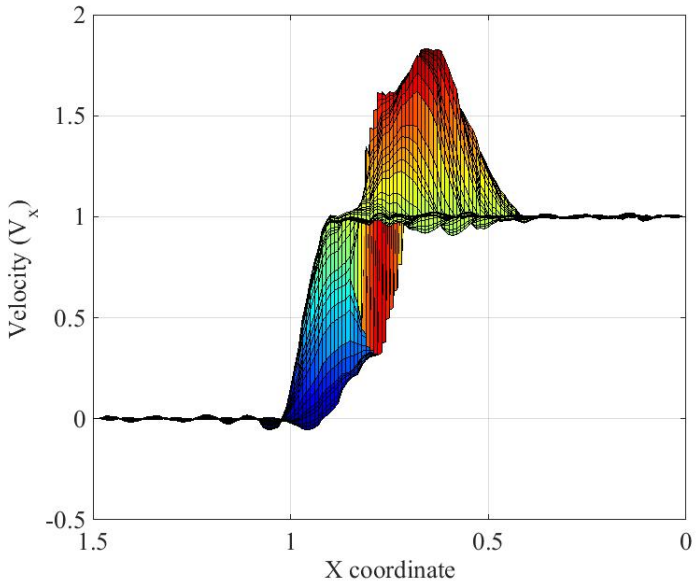

Fig. 2.8: Illustration of the convergence process of the PNM-GFEM to oscillation-free results using cutoff number $n = 3$.

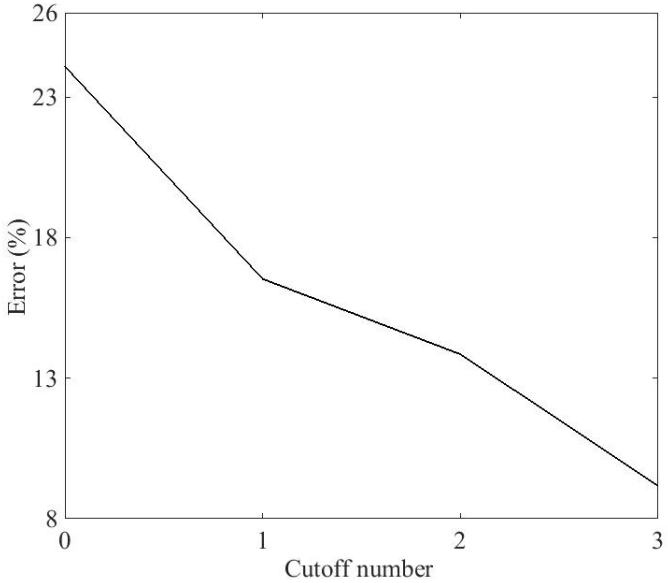

Fig. 2.9: Convergence behaviour of PNM-GFEM upon increasing the number of enrichment basis functions.

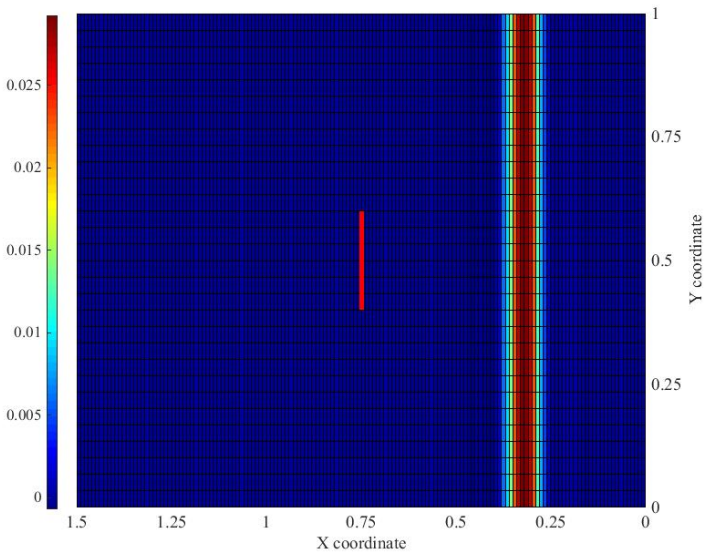

Fig. 2.10: Illustration of x-displacement at $t = 70\mu s$, using PNM-GFEM with a cutoff number $n = 1$, before the wave reaches the crack.

oscillations can be further suppressed by including more enrichment functions (i.e., increasing the cutoff number) in the finite element calculation. As seen in Figure 2.13 by using a cutoff number $n = 2$, the oscillations are further reduced.

Figure 2.14 shows that the wave pattern obtained using the standard PNM and the PNM-GFEM for different mesh sizes. As seen, mesh refinement is not effective in suppressing the spurious oscillations observed when using the standard PNM. The use of meshes with smaller elements changes the frequency of the spurious oscillations in the PNM results; however, significant numerical error still exists. The numerical error is also apparent in the reduction of the peak amplitude of the wave in the PNM results. As can be seen in the last figure (obtained using PNM-GFEM), the peak magnitude of the wave pulse is 0.03 m, which is equal to the amplitude of the external displacement stimulation/ analytical solution (see equation 33). Thus, the developed PNM-GFEM is used the spurious oscillations ahead of both primary emitted and secondary reflected waves are effectively eliminated; these spurious oscillations cannot be eliminated effectivily in the standard PNM using mesh refinement. This result is analogous to that reported in comparisons between the GFEM and the FEM in [79].

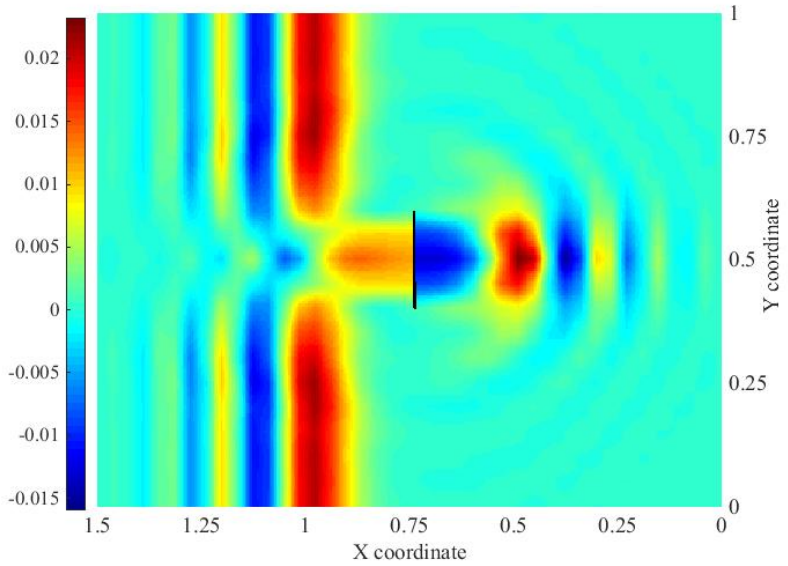

Fig. 2.11: Illustration of x-displacement at $t = 188\mu s$, using conventional PNM.

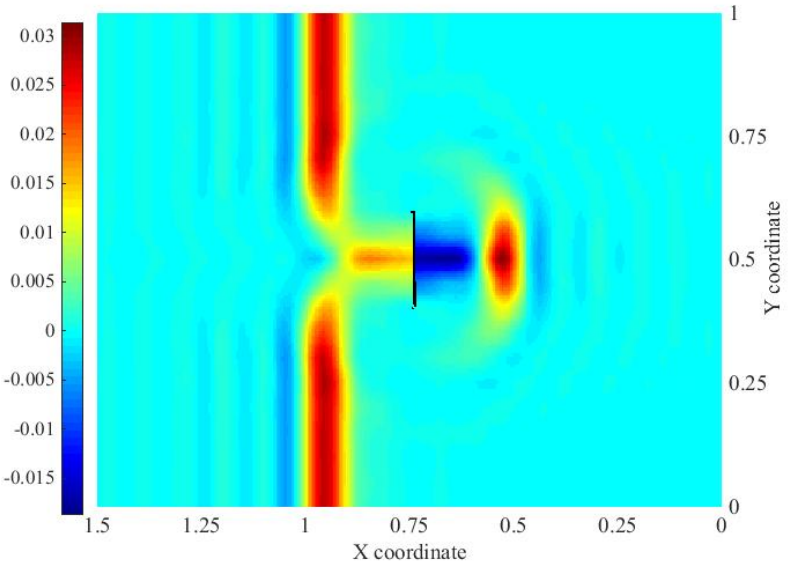

Fig. 2.12: Illustration of x-displacement at $t = 188\mu s$, using PNM-GFEM with $n = 1$.

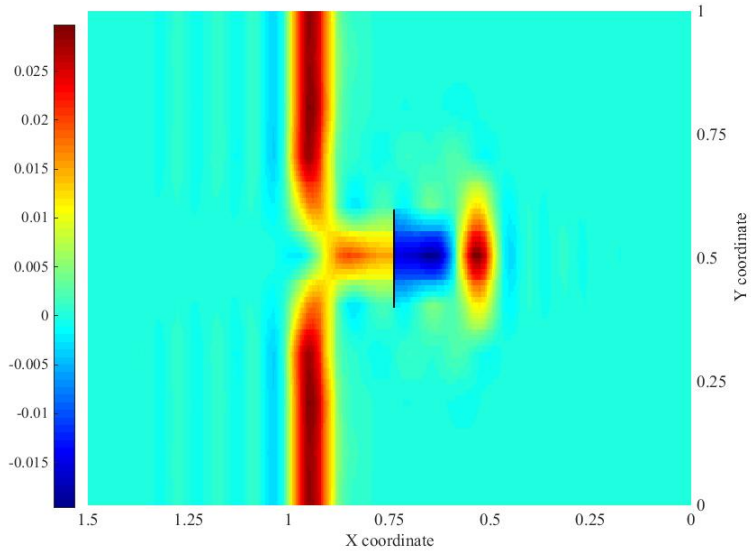

Fig. 2.13: Illustration of x-displacement at $t = 187\mu s$, using PNM-GFEM with $(n = 2)$.

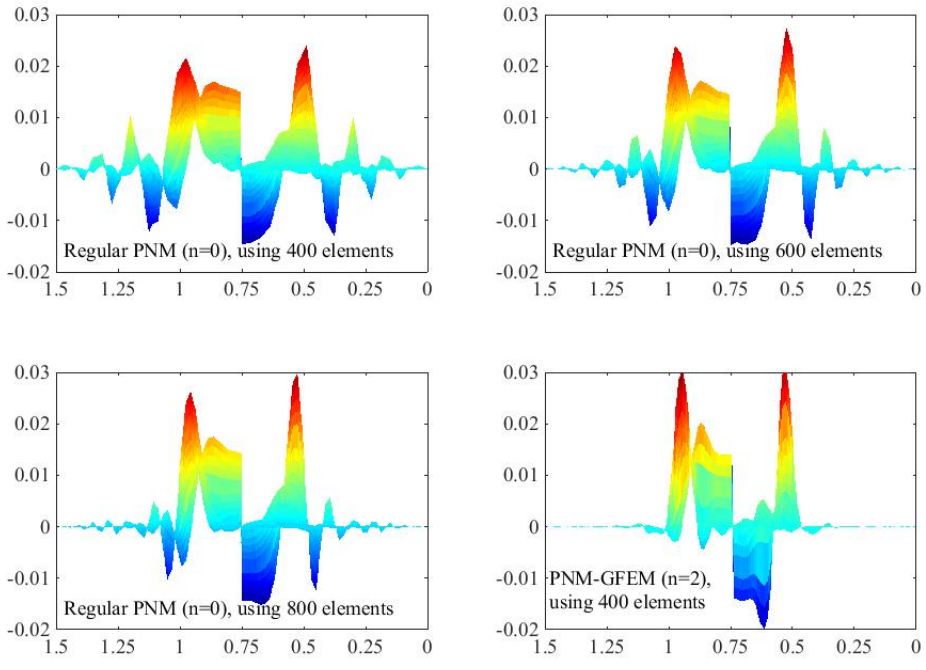

Fig. 2.14: Illustration of x-displacement at $t = 188\mu s$ for different mesh sizes as a function of x; the y-coordinate is perpendicular to the plane of the figure.

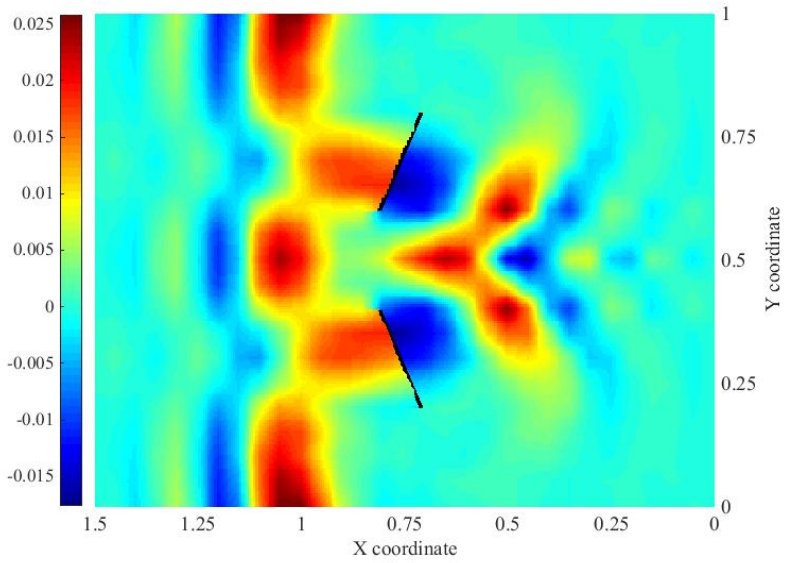

Fig. 2.15: Illustration of x-displacement at $t = 200\mu s$, using conventional FEM.

2.5.3 Wave Propagation - Multiple Crack Example

To illustrate the behaviour of the developed computational model for wave propagation problem in the case of a media with multiple cracks, a $1.5m \times 1m$ domain and a 30×20 elements mesh is considered. The cracks are placed at $63.5°$ with respect to the horizontal direction and are $0.2236m$ in length, as shown in figures 2.15 and 2.16. A displacement stimulation is imposed on the boundary $x = 0$ of the form of (2.33) with $\tau = 1.8 \times 10^{-5}$s.

Figure 2.15 shows the wave profile obtained using conventional PNM at time $t = 200\mu s$. Strong spurious oscillations are observed ahead of both primary and reflected waves. To demonstrate the ability of the developed enriched FE model to reduce non-physical oscillations, Figure 2.16 depicts the wave pattern of the same problem solved using PNM-GFEM with cutoff number $n = 1, m = 0$ at time $t = 200\mu s$. It is clear that the oscillations have been significantly reduced by using enriched FEM.

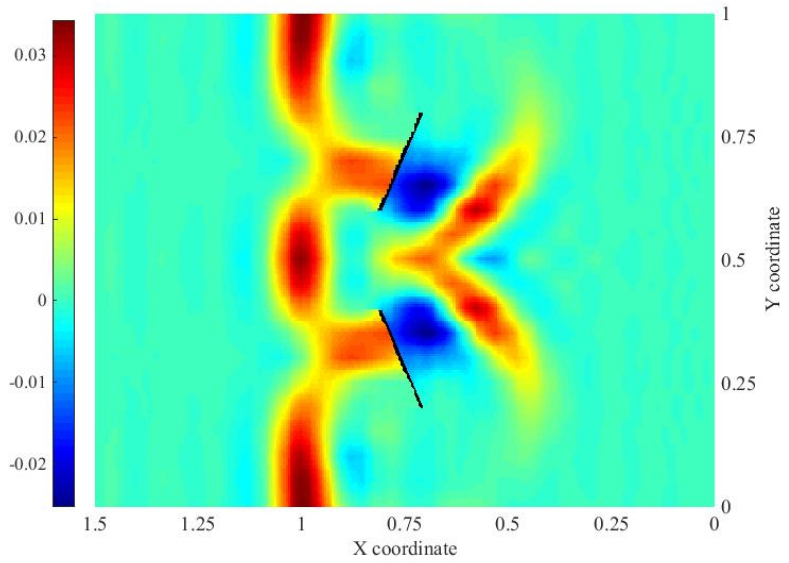

Fig. 2.16: Illustration of x-displacement at $t = 200\mu s$, using enriched FEM with (n=1).

2.5.4 Numerical study of the Critical Time Step in Explicit method using consistent and lumped mass matrices

In this section the ability of the mass lumping technique, described in Section 2.4, to yield a critical time step size for an explicit analysis using a second order central difference method is in a reasonable range is demonstrated. The case of wave propagation in a fractured domain is considered. The geometry of the domain and the location of the fracture is shown in Figure 2.15 and is meshed by a 20×10 bilinear elements. The standard Eigenvalue procedure is employed to obtain the critical time step of the central difference explicit method, as described in [85]. The critical time step for the intact fracture-free domain and fractured domain are reported in Tables 2.2-2.4 for the cases of the consistent and lumped mass matrix. In the results presented in Tables 2.2 and 2.3 only enrichments in the x-direction has been considered (i.e., $m = 0$). In Table 2.4 the critical time step has been reported for the case of multi-axial enrichment for various values of n and m. As can be seen, in the case of the consistent mass matrix, the critical time step decreases significantly, when a discontinuity is introduced into the domain via the Phantom Node Method, in comparison with the value obtained for the original intact domain. The critical time step for the intact domain is 7.8 times larger than that of the fractured

domain, even when no harmonic enrichments are used ($m = n = 0$). Furthermore, as harmonic enrichments are add, i.e., as n and m increase, the critical time step decreases precipitously and the discrete system of equations become ill-conditioned. The critical time step sizes when the consistent mass matrix is used are very small, so small, that the computational cost of using the Phantom Node Method with GFEM enrichment with high cutoff numbers may be prohibitive for practical problems.

The critical time steps computed using lumped mass matrices are noticeably larger than the corresponding values obtained using the consistent mass matrix, whether the domain is fractured or not. The critical time step obtained for fractured domains is almost the same as that of intact continuous domains. Furthermore, the critical time step size for the lumped mass matrix simulations, doesn't decrease as rapidly as the number of GFEM enrichment terms, n or m, increases as occurs when the consistent mass matrix is used in the simulation.

It was not possible to simulate wave propagation using a consistent mass matrix when $n \geq 3$ due to the ill-conditioning of the consistent mass matrix. To overcome the problem of ill-conditioning in implicit analysis, Strouboulis et. al. [86] proposed an iterative approach based on perturbing the diagonal terms of the original ill-conditioned matrix and then iterating until the resulting error is negligible. As an alternative Ham and Bathe [79] used a weighted summation of the consistent and lumped mass matrix as the inertia matrix of the problem in which the coefficient of lumped mass matrix is very small. The total mass diagonal scaling method is used in their work for developing a lumped mass matrix. Although the applicability of the simple diagonal scaling mass lumping can be questionable in the context of GFEM, their proposed scheme seems to be efficient (compared to the aforementioned iterative method), since a very small magnitude is used as the multiplier of the lumped mass matrix. It seems likely that the lumped mass matrix proposed here may be of value in addressing the ill-conditioning problem found in implicit time integration, as considered in [79] . However, it is clear that the problem of ill-conditioning does not occur in the case of the diagonal kinetic energy-consistent lumped mass matrix of the present work.

Table 2.2: A comparison between the critical time steps of cracked and original intact domains using the enriched FE model for various values of the cutoff number n ($m = 0$) for the consistent mass matrix.

n	Intact (consistent mass)	Cracked (consistent mass)	Ratio
0	7.5514×10^{-6}	9.5158×10^{-7}	7.9
1	2.1477×10^{-6}	2.8374×10^{-7}	7.6
2	1.0631×10^{-6}	5.6114×10^{-8}	18.9
3	6.4145×10^{-7}	ill-conditioned mass matrix	$--$
4	1.4928×10^{-7}	ill-conditioned mass matrix	$--$

Table 2.3: A comparison between the critical time steps of cracked and original intact domains using the enriched FE model for various values of the cutoff number n ($m = 0$) for the lumped mass matrix.

n	Intact (lumped mass)	Cracked (lumped mass)	Ratio
0	1.4306×10^{-5}	1.4297×10^{-5}	1
1	4.1965×10^{-6}	4.1964×10^{-6}	1
2	2.2177×10^{-6}	2.0676×10^{-6}	1.07
3	1.4810×10^{-6}	1.3919×10^{-6}	1.06
4	6.6043×10^{-7}	6.6130×10^{-7}	0.99

Table 2.4: A comparison between the critical time steps of cracked and original intact domains using the multi-directional enriched FE model for various values of the cutoff numbers n and m.

n	m	Intact (lumped mass)	Cracked (lumped mass)
0	0	1.4306×10^{-5}	1.4297×10^{-5}
1	0	4.1965×10^{-6}	4.1964×10^{-6}
0	1	5.3399×10^{-6}	5.2151×10^{-6}
1	1	3.3994×10^{-6}	3.2607×10^{-6}
2	2	1.6999×10^{-6}	1.2673×10^{-6}

2.5.5 Role of Crack Location in Element

To assess the effect of the crack's location on the critical time step size a $0.1 \times 0.1[m]$ bilinear rectangular element is considered. The interpolation of the variables inside the element are represented by enriched FEM with cutoff numbers $n = 1$ and $m = 0$. A vertical crack is assumed to divide the element into two superimposed elements. Figure 2.17 depicts the critical time step as a function of the location of the crack within the element. Δt_{cr} is the critical time step of the PNM-GFEM model. The results are normalized using the critical time step of the same element without any crack Δt^0_{cr}. The normalized critical time step sizes are shown as a function of A_{e1}/A_0, where A_{e1} is the active area of the superposed element 1 and A_0 is the total area of the element. As shown in this figure, the critical time step obtained using the proposed lumped mass matrix for the PNM-GFEM model decreases to a finite value as the crack approaches the element edge. This is in contrast to the critical time step obtained using the consistent mass matrix, which tends to zero as the crack approaches the element edge. This result further emphasizes the advantages of using the lumped mass matrix proposed here.

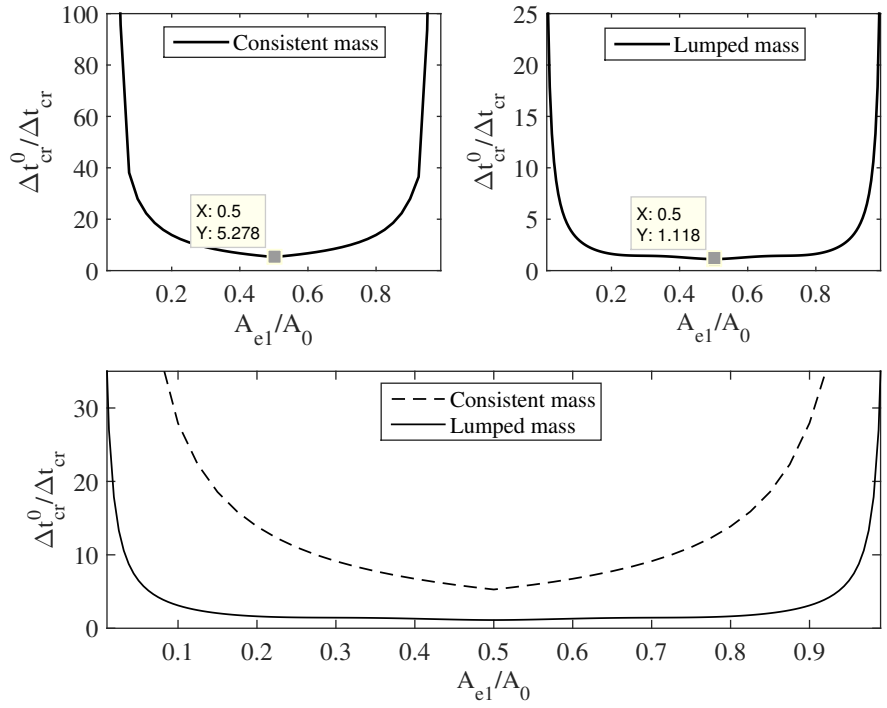

Fig. 2.17: A comparison between the critical time step obtained using the consistent and lumped mass as a function of the crack's location in the element.

2.6 Chapter Conclusions

A new enriched finite element method has been developed to more accurately simulation wave propagation in discontinuous (fractured) domains. The numerical method combines the Phantom Node Method (PNM) to model fractures and the Generalized Finite Element Method (GFEM) to accurately model wave phenomena. Global harmonic enrichment functions have been embedded into the framework to more accurately simulation wave profiles and to reduce the effect of numerical dispersion and spurious oscillations. The general idea of the Phantom Node Method has been adopted to the capture discontinuous displacement in the fractured media, in which a cracked element is replaced by two superimposed regular elements with additional phantom nodes. Through three numerical examples it was demonstrated that the spurious oscillations that appear in propagation pattern of high-frequency waves in PNM simulations can be effectively suppressed by including harmonic enrichment functions (PNM-GFEM). This is observed to be especially important in fractured media where both primary waves and the

secondary reflected waves are present. A specific kinetic energy-consistent lumped mass matrix was proposed for the PNM-GFEM leading to superiour performance in explicit simulations. It was demonstrated that when a consistent mass matrix is used, the critical time step size in explicit time integration simulations tends to zero as the fracture location tends toward the edge of an element and the PNM-GFEM struggles with ill-conditioning problems. In contrast, it was demonstrated that when the proposed lumped mass matrix is used, the critical time step size is both finite (even when a crack lies along an element edge) and of the same order of magnitude of that of the underlying FEM, and ill-conditioning problems are mitigated. The PNM-GFEM is a promising method for the simulation of wave phenomena in fractured media.

Chapter 3

Enriched mixed finite element models for dynamic/wave propagation analysis of continuous and fractured porous media

This chapter is based on the following journal article:

Komijani M., Gracie R., Enriched Mixed Finite Element Models for Dynamic Analysis of Continuous and Fractured Porous Media, *Computer Methods in Applied Mechanics and Engineering*, 343: 74–99, 2019 [36].

In this journal paper I was the first author and was responsible for the writing of the article. The paper was edited by Dr. Gracie. I also developed the mathematical and computational formulation and the numerical code.

This chapter addresses objective 2 of the thesis.

3.1 Introduction

Enriched Finite Element Models are presented to more accurately investigate the transient and wave propagation responses of continuous and fractured porous media based on mixture theory. Firstly, the Generalized Finite Element Method (GFEM) trigonometric enrichments are introduced to suppress the spurious oscillations that may appear in dynamic analysis with the regular Finite Element Method (FEM) due to numerical dispersion/Gibbs phenomenon. Secondly, the Phantom Node Method (PNM) is employed to model multiple arbitrary fractures independently of the mesh topology. Thirdly, frictional contact behaviour is simulated using an Augmented Lagrange Multiplier technique. Mixed Lagrangian interpolants, bi-quadratic for displacements and bi-linear for pore pressure, are used for the underlying FEM basis. Transient (non-wave propagation) response of fractured porous media is effectively modeled using the PNM. Wave propagation in continuous porous media is effectively modeled using the mixed GFEM. Wave propagation in fractured porous media is accurately simulated using a mixed GFEM-enriched Phantom Node Method (PNM-GFEM-M). The developed mixed GFEM portion of the model is verified through a transient consolidation problem. Subsequently, the ability of the enriched FEM models to capture the dynamic response of fractured fully-saturated porous media under mechanical and hydraulic stimulations is illustrated. The superior ability of the PNM-GFEM-M to inhibiting spurious oscillations is shown in comparison against the regular finite element solutions of some impact problems. It is demonstrated that by embedding appropriate enrichment basis functions in both displacement and pore pressure fields the results obtained are more accurate than those obtained using standard finite element approximations or approximations in which only the displacement is enriched.

Analysis of porous media is of importance in a wide range of applications from reservoir engineering to biological materials. Accurate simulation of coupled behaviour of fluid and solid in geomechanics is essential in improving the reservoir performance and ensuring wellbore stability[102]. In a similar fashion, biomechanical analysis of tissues such as the brain, bones,

and cells involves coupled behaviour of solid skeleton and a pore fluid [103, 104, 105, 106]. Investigations of coupled hydro-mechanical problems has a relatively long history going back to the pioneering works of Terzaghi [107] and Biot [108].

Dynamic analysis is important in applications such as liquefaction, induced seismicity, and earthquake analysis, in which inertia effects are of significance. In coupled analysis of porous media, different approaches have been developed to model the hydro-mechanical response. Fully-dynamic three-field models ($u-w-p$) have been used to solve the problem based on the solution for solid skeleton displacement, u, the displacement of the fluid relative to the solid matrix, w, and the fluid pore pressure, p [109, 110]. In some other works, based on the assumption that the relative acceleration of fluid with respect to the total mixture is negligible, a simpler two-field formulations ($u-p$) had been developed [111]. Alternative formulation based on the same assumption has lead to ($u-w$) models, in which pore pressure is eliminated instead of the relative displacement of fluid with respect to the solid skeleton [112, 113] . Two-field $u-p$ models of porous media have been noted to be more appropriate for modelling saturated porous material up to earthquake frequencies [114].

Previous research efforts in dynamic/wave propagation analysis of porous media have emphasized the hydro-mechanical response of continuous domains. However, in many applications, such as the analysis of naturally fractured rock masses, we encounter discontinuous domains which contain pre-existing or induced cracks and/or faults. The analysis of microseismic emission due to the reactivation of natural fractures in geological formations under high in-situ stresses is of practical importance in the evolution of hydraulic fracturing operations, which has not been dealt with sufficiently in the literature so far.

The dominant approach in seismic analysis has been to solve wave propagation in frequency domain [115] with the assumption that the simulation domain is continuous and does not contain any fractures; in spite the fact that the coupled problem of micro-seismic emission due

to fault reactivation has to be partially modeled (in localization/crack propagation phase) in the time domain. Therefore, developing new and efficient time domain-based computational methods and tools to simulate the dynamic hydro-mechanical response of porous systems that include discontinuities seems to be necessary and practical.

In the area of fractured porous media analysis, Remij et al. [116] present an enhanced local pressure model for simulation of fluid-driven fractures in porous media using partition-of-unity finite element to impose strong discontinuity of displacement and pressure fields across the fracture. In this work, fracture propagation due to internal flow is modeled by a cohesive traction-separation law. Nikolic et al. [117] proposed a discrete beam lattice model for simulation of localization in a fluid-saturated poro-plastic media. Localized failure of media is embedded through discontinuities located in cohesive links enabled by the proposed discrete model which can capture the fracture process zone initiation and the localization mechanisms. Armero and Callari [119] performed an analysis of strong discontinuities in displacement in a poroplastic solid. They considered continuous pressure field across the material discontinuity with discontinuous pressure gradient leading to discontinuous fluid flux across the crack. They used an enhanced strain finite element formulation to represent the normal and shear displacement jumps along the discontinuity. Réthoré et al. [118] developed a numerical model for dynamic propagation of shear bands in saturated porous media. They used the partition of unity property of finite element to introduce discontinuity in the domain in the context of XFEM. Using cohesive shear tractions they simulated nucleation and propagation of shear bands based on Tresca-like and a Coulomb criterion.

Another approach for simulation of fracture in porous media has been the phase field modeling. Christian Miehe and Steffen Mauthe [120] proposed a macroscopic framework for a continuum phase field modeling of fracture in porous media. The main idea in this approach is to regularize the discrete crack based on a constitutive balance equation. The approach overcomes difficulties associated with the computational realization of sharp discontinuities which is

involved in discontinuity modeling and specifying the trajectory of fracture once it propagates. The multi-physics coupling of porous media is accommodated through a modular concept for linking of the diffusive crack modeling with the hydro-poro-elastic response of the porous bulk material. Lee et al. [121] employed phase field approach for proppant-filled fractures in porous media to solve for displacements, phase field, pressure, and proppant concentration though a continuum model. The coupling to the pressure equation is imposed via a fixed-stress iteration. A diffraction equation is used to obtain the pressure and the phase-field variable serves as an indicator function that distinguishes between the fracture and the reservoir. In this context, some damage localization models have also been proposed for porous media. Mobasher et al. [122] proposed a damage-poroelastic model for analyzing the localization of porous media in geomechanics applications. The mesh-dependency problem of local damage models has been rectified by introducing a non-local model. However, these earlier works that are proposed to model fracture in porous media did not address the topic of accurate simulation of wave propagation in multi-physics media.

To model arbitrary fractures independently of mesh topology and to rectify the requirement for continuous re-meshing in the process of crack propagation Moës et al. [26] developed the concept of the eXtended Finite Element Model (XFEM). XFEM is based on the general idea of the Partition of Unity Finite Element Method [20]. As a continuation, Song et al. [29] introduced and developed the idea of Phantom Node Method (PNM) to model discontinuities. The model is in essence the same as the earlier method proposed by Hansbo and Hansbo [31]. In the PNM, discontinuity in displacement is achieved by reformulating elements, which contain a fracture as two superimposed intact elements with additional computational nodes, called Phantom Nodes. Each of the superimposed elements is used to represent a different side of the original cracked element, resulting in a discontinuous interpolation for displacement. The most important feature and advantage of the PNM is that its implementation requires fewer modifications to an existing FEM code compared to XFEM. To date the PNM has only been applied to classical applications in structural mechanics. Here we extend its application to

fractured porous media.

Owing to the direct satisfaction of the natural boundary conditions through integral form of the weak formulation (divergence theorem), the finite element method is known to be a very effective tool for solving boundary-value problems. However, the piecewise continuous polynomials used to interpolate the unknown functions have been found to be inadequate in some problems, including transient wave propagation [79]. In the case of transient wave propagation, FEM solution may show spurious oscillations. These non-physical oscillations degrade the accuracy of the results, including the wave propagation velocity, which is important in application such as microseismic wave simulation, where the waves travel long distances. Here, this problem is treated through introduction of harmonic enrichments.

An enriched finite element method was proposed in [78], where enriched harmonic and conventional low-order polynomials interpolations are used to model multiscale wave propagation in one-dimensional problems. The general idea of embedding appropriate basis functions, with characteristics that appear in the analytical solution of the problem, as enrichments using the partition of unity property of the FE interpolants was developed in the pioneering work of Melenk and Babuška [20]. For more detailed information about enriched finite element methods one can also refer to [21, 22, 23]. Based on the general idea of the Partition of Unity Method (PUM), Ham and Bahte [79] extended the approach of [78] to solve the problem of time-harmonic and transient wave propagation in multiple dimensions; it was demonstrated that the spurious oscillations that appear with the conventional FEM can effectively subside by the proposed enriched FEM in the simulation of wave propagation in continuous domains.

Very recently, a GFEM-enriched PNM model was proposed by Komijani and Gracie [32] to extend the enriched FE model developed in [79] to the case of fractured media. Their enriched FE model, the PNM-GFEM, combines the advantages of the trigonometric enrichments introduced in [79] and the Phantom Node Method. Using the PNM-GFEM, problem of transient

wave propagation in fractured media is simulated in various cases of high-frequency/impact mechanical loading conditions. Through several numerical illustrations it was demonstrated that the high-frequency non-physical spurious oscillations can be dramatically suppressed in both primary emitted waves and reflected waves from the fracture surfaces.

To date these enriched finite element models have not been applied to any coupled multi-physics problem with or without discontinuities, such as fractured porous media. The purpose of the present article is to extend the use of the PNM-GFEM enriched FE model introduced in [32] to the case of fractured saturated porous media. GFEM trigonometric functions are used to enrich the displacement field of solid skeleton and pore pressure field to model transient wave propagation response of porous media more accurately. The PNM is employed in a combined fashion to simulate discontinuities in the displacement fields as well as pore pressure field in the case of impervious crack faces. The dynamic behaviour of fractured porous media is investigated through several numerical examples for different mechanical and hydraulic loading types.

3.2 Mathematical Formulation

A porous media is composed of a fluid filled solid matrix. The fluid phase can flow through the connected voids of the solid matrix. The behaviour of a porous media is governed by the interaction of fluid and solid phases. In this work, the governing equations are obtained from Biot's mixture theory based on the concept of volume fractions for each phase in a representative elementary volume.

3.2.1 Governing Equations

Consider a two-dimensional poroelastic medium, Ω, defined in Cartesian coordinate O_{xy}. Let $u_x(x, y, t)$ and $u_y(x, y, t)$ be the displacement components of the total mixture in x and y directions, respectively, as a function of time, t. Assuming infinitesimal deformation, the linear strain-displacement relations are

$$\varepsilon_{xx} = u_{x,x} \qquad \varepsilon_{yy} = u_{y,y} \qquad \gamma_{xy} = u_{x,y} + u_{y,x} \tag{3.1}$$

The constitutive equations for the solid matrix can be written in Voigt notation as:

$$\begin{bmatrix} \sigma'_{xx} \\ \sigma'_{yy} \\ \sigma'_{xy} \end{bmatrix} = \begin{bmatrix} C_{11} & C_{12} & 0 \\ C_{21} & C_{22} & 0 \\ 0 & 0 & C_{33} \end{bmatrix} \begin{bmatrix} \varepsilon_{xx} \\ \varepsilon_{yy} \\ \gamma_{xy} \end{bmatrix} \tag{3.2}$$

in which σ'_{xx}, σ'_{yy}, and σ'_{xy} are the components of the effective stress tensor acting on the solid skeleton, and C_{11} through C_{33} are the elastic coefficients.

The relative motion of the fluid phase with respect to the total mixture is denoted by $w_i(x, t)$; it is assumed that the relative acceleration of the fluid phase with respect to the entire

mixture is negligible, i.e., $\ddot{w}_i = 0$. The momentum balance of the total mixture is:

$$\nabla \cdot \boldsymbol{\sigma} - \rho \ddot{\boldsymbol{u}} + \rho \boldsymbol{b} = 0 \tag{3.3}$$

in which $\ddot{\boldsymbol{u}}$ is the acceleration of the total mixture, $\boldsymbol{\sigma}$ is the total stress, ρ is the average mixture density, and b is the body force acting on the mixture.

The average density of the mixture is defined as a linear combination of solid and fluid phases

$$\rho = n'\rho_f + (1 - n')\rho_s \tag{3.4}$$

in which ρ_f and ρ_s are the density of fluid phase and solid grains, respectively, and n' is the porosity of the media, defined as the ratio of the porous volume to the total volume of the mixture.

The total stress acting on the mixture is defined as

$$\boldsymbol{\sigma} = \boldsymbol{\sigma'} - \alpha_p p \boldsymbol{I} \tag{3.5}$$

where p is the fluid pore pressure, $\boldsymbol{I}$ is the identity tensor, $\boldsymbol{\sigma'}$ denotes the effective stress acting on the solid skeleton, and α_p is Biot's coefficient.

A generalized Darcy relation can be derived from conservation of momentum of the fluid phase. Neglecting the relative acceleration of the pore fluid with respect to the total mixture, the momentum equation for the fluid phase is:

$$-\nabla p + \boldsymbol{R} - \rho_f \ddot{\boldsymbol{u}} + \rho_f \boldsymbol{b} = 0 \tag{3.6}$$

in which $\boldsymbol{R}$ denotes the lumped/averaged viscous drag force acting on the fluid. The drag force may be defined by the Darcy seepage law

$$\dot{\boldsymbol{w}} = -\boldsymbol{k}_f \boldsymbol{R} \tag{3.7}$$

in which $\boldsymbol{k}_f$ denotes the permeability tensor of the porous media.

The Eulerian continuity equation for the fluid phase is:

$$\nabla \cdot \dot{\boldsymbol{w}} + \alpha \nabla \cdot \dot{\boldsymbol{u}} + \frac{\dot{p}}{Q} = 0 \tag{3.8}$$

in which $1/Q = (\alpha - n')/K_s + n'/K_f$, and K_s and K_f are the bulk moduli of solid and fluid phases, respectively.

The relative velocity of fluid phase with respect to the mixture, $\boldsymbol{w}$, can be eliminated from (4.8) using (4.6) and the Darcy seepage law (4.7) leading to [114]

$$\nabla \cdot k_f[-\nabla p - \rho_f \ddot{\boldsymbol{u}} + \rho_f \boldsymbol{b}] + \alpha \nabla \cdot \dot{\boldsymbol{u}} + \frac{\dot{p}}{Q} = 0 \tag{3.9}$$

Equations (4.3) and (4.9) along with the strain-displacement relations (4.1) and effective stress-strain constitutive equations (4.2) are solved together with boundary and initial conditions to find the displacement and pore pressure fields.

3.2.2 Weak Formulation

Consider a 2D domain Ω with boundary Γ. Boundary Γ comprises of Γ_u, Γ_t, Γ_p, and Γ_w, which are the boundary surface for prescribed displacement, traction, pore pressure, and out-flow flux of pore fluid, respectively. Domain Ω contains internal discontinuities (i.e., fractures) denoted by Γ_d. Using Galerkin's method the coupled system of equations (4.3) and (4.9) are transformed into a weak formulation using appropriate test functions, $\delta \boldsymbol{u}$ and δp.

The admissible spaces of the displacement and pore pressure fields are defined as below:

$$U = \left\{ \mathbf{u}(x,y,t) | \mathbf{u}(x,y,t) \in H^1, \mathbf{u}(x,y,t) = \bar{\mathbf{u}}(t) \; on \; \Gamma_u, \mathbf{u} \; discontinuous \; on \; \Gamma_d \right\} \tag{3.10}$$

$$U_0 = \left\{\delta \boldsymbol{u}(x,y,t) | \delta \boldsymbol{u}(x,y,t) \in H^1, \delta \boldsymbol{u}(x,y,t) = 0 \; on \; \Gamma_u, \delta \boldsymbol{u} \; discontinuous \; on \; \Gamma_d\right\} \tag{3.11}$$

$$P = \left\{p(x,y,t) | p(x,y,t) \in H^1, p(x,y,t) = \bar{p}(t) \; on \; \Gamma_p, p \; discontinuous \; on \; \Gamma_d\right\} \tag{3.12}$$

$$P_0 = \left\{\delta p(x,y,t) | \delta p(x,y,t) \in H^1, \delta p(x,y,t) = 0 \; on \; \Gamma_p, \delta p \; discontinuous \; on \; \Gamma_d\right\} \tag{3.13}$$

The resulting weak form of the initial boundary value problem is

$$\int_\Omega \boldsymbol{\sigma} : \delta \boldsymbol{\varepsilon} \; d\Omega + \int_\Omega \rho \ddot{\boldsymbol{u}} \cdot \delta \boldsymbol{u} \; d\Omega - \int_{\Gamma_t} \bar{\boldsymbol{t}} \cdot \delta \boldsymbol{u} \; d\Gamma - \int_\Omega \rho \boldsymbol{b} \cdot \delta \boldsymbol{u} \; d\Omega + \int_{\Gamma_d} \bar{\boldsymbol{t_d}} \cdot \delta [[\boldsymbol{u}]] \; d\Gamma = 0, \forall \delta \boldsymbol{u} \in U_0 \tag{3.14}$$

$$\int_\Omega \nabla \delta p \cdot k_f \nabla p \; d\Omega + \int_\Omega \nabla \delta p k_f \cdot \rho_f \ddot{\boldsymbol{u}} \; d\Omega + \int_\Omega \delta p \; \alpha_p \; \nabla \cdot \dot{\boldsymbol{u}} \; d\Omega + \int_\Omega \delta p \; 1/Q \; \dot{p} \; d\Omega -$$

$$\int_\Omega \nabla \delta p k_f \cdot \rho_f \boldsymbol{b} \; d\Omega + \int_{\Gamma_w} \delta p (\dot{\boldsymbol{w}} \cdot \boldsymbol{n}_\Gamma) \; d\Gamma - \int_{\Gamma_d} \delta p [[\dot{\boldsymbol{w}}]] \cdot \boldsymbol{n}_{\Gamma_d} \; d\Gamma = 0, \forall \delta p \in P_0 \tag{3.15}$$

in which $[[\boldsymbol{u}]]$ denotes the jump in the displacement field across the discontinuity surfaces and $[[\dot{\boldsymbol{w}}]]$ represents the discontinuity of fluid flux into the crack interface in both sides of the discontinuity. $\bar{\boldsymbol{t_d}}$ denotes the internal applied traction (e.g., contact force) on the surfaces of the internal discontinuity Γ_d. In this work natural boundary conditions are imposed on the internal interface, Γ_d. For the mechanical problem, the tractions on the crack surfaces are non-zero when contact is modeled or zero (traction free) when contact is not modeled. For flow problem, the fluid flux perpendicular to the fracture surfaces is zero for impermeable fractures. In the

case of permeable fractures, there is no discontinuity in the pore pressure field and therefore no natural boundary condition needs to be considered on Γ_d.

3.3 Enriched Mixed Finite Element Formulation

In this section, the discretization of the weak form (4.10)-(4.11) using the PNM-GFEM interpolations [32], the implementation of frictional contact using an Augmented-Lagrangian approach, the integration of the semi-discretized equations using a Generalized Newmark implicit method are discussed.

3.3.1 GFEM interpolation

Spurious waves due to the Gibbs phenomenon can be suppressed/reduced in FEM simulations of transient wave propagation in continuous domains by GFEM enrichment with appropriate functions. Inspired by the exponential- (or trigonometric-) type nature of the analytical solutions of wave problems, Ham and Bathe [79] proposed the following interpolation for displacement

$$\begin{aligned}\boldsymbol{u}(x,y,t) = \sum_I \Big(& N_I \boldsymbol{u}_{I(0,0)} + \sum_{k_x=1}^{n} [N_I \phi^{C_x}_{(k_x,0)} \boldsymbol{u}^{C_x}_{I(k_x,0)} + N_I \phi^{S_x}_{(k_x,0)} \boldsymbol{u}^{S_x}_{I(k_x,0)}] + \\ & \sum_{k_y=1}^{m} [N_I \phi^{C_y}_{(0,k_y)} \boldsymbol{u}^{C_y}_{I(0,k_y)} + N_I \phi^{S_y}_{(0,k_y)} \boldsymbol{u}^{S_y}_{I(0,k_y)}] + \\ & \sum_{k_x=1}^{n} \sum_{k_y=1}^{m} [N_I \phi^{C+}_{(k_x,k_y)} \boldsymbol{u}^{C+}_{I(k_x,k_y)} + N_I \phi^{S+}_{(k_x,k_y)} \boldsymbol{u}^{S+}_{I(k_x,k_y)} + \\ & N_I \phi^{C-}_{(k_x,k_y)} \boldsymbol{u}^{C-}_{I(k_x,k_y)} + N_I \phi^{S-}_{(k_x,k_y)} \boldsymbol{u}^{S-}_{I(k_x,k_y)}] \Big)\end{aligned} \tag{3.16}$$

in which $\phi^{\gamma}_{(k_x,k_y)}$ with the corresponding superscript denotes the following trigonometric enriched basis functions:

$$\phi^{C_x}_{(k_x,0)} = cos(\frac{2\pi k_x x}{\Lambda_x}), \quad \phi^{S_x}_{(k_x,0)} = sin(\frac{2\pi k_x x}{\Lambda_x}),$$

$$\phi^{C_y}_{(0,k_y)} = cos(\frac{2\pi k_y y}{\Lambda_y}), \quad \phi^{S_y}_{(0,k_y)} = sin(\frac{2\pi k_y y}{\Lambda_y})$$

$$\phi^{C+}_{(k_x,k_y)} = cos(\frac{2\pi k_x x}{\Lambda_x} + \frac{2\pi k_y y}{\Lambda_y}), \quad \phi^{S+}_{(k_x,k_y)} = sin(\frac{2\pi k_x x}{\Lambda_x} + \frac{2\pi k_y y}{\Lambda_y})$$

$$\phi^{C-}_{(k_x,k_y)} = cos(\frac{2\pi k_x x}{\Lambda_x} - \frac{2\pi k_y y}{\Lambda_y}), \quad \phi^{S-}_{(k_x,k_y)} = sin(\frac{2\pi k_x x}{\Lambda_x} - \frac{2\pi k_y y}{\Lambda_y})$$

In the above enriched FE formulation N_I are the conventional Lagrangian shape functions, $u_{I(0,0)}$ are the conventional nodal degrees of freedom, $u^{\gamma}_{I(k_x,k_y)}$ with the associated superscript $(C_x, C_y, S_x, S_y, ...)$ are the enriched nodal degree of freedom corresponding to the local node number I, k_x and k_y are the wave numbers, n and m are the cutoff numbers for enrichment functions in x and y directions, respectively, and Λ_x and Λ_y are wavelengths, which are assumed to be equal to the element sizes in x and y directions, respectively. It is noted that the cut-off numbers n and m are user-defined parameters and would vary between different problems. In the case of highly-transient waves or time-harmonic waves with short wave lengths, higher cutoff numbers may be required to obtained more accurate results. The excitation of different wave lengths can be modeled using different cutoff numbers, which facilitates the possibility of modelling waves with wavelengths smaller than the element size. It is important to note that considering higher cutoff numbers than 2 may lead to severe ill-conditioning problems. However, based on our experience so far, cutoff numbers of 1 or 2 is sufficient in many cases.

To model the dynamic/wave propagation response of fracture media, the Phantom Node Method [32] is combined with the above GFEM approximation (3.16). The PNM is employed to facilitate the modelling of the discontinuities and GFEM enrichments are used to more accurately model wave propagation, compared to what can be achieve with regular FEM approximations. As illustrated in Figure 3.1, a cracked element containing a discontinuity is represented by two superimposed intact elements (i.e., overlapping paired elements) with real and additional phantom nodes [29]. The location of the discontinuity inside an element is defined by a level set function such that $f(x, y) = 0$ specifies the discontinuous surface. In this work the level set is the signed distance function to the crack [29]. Displacements in fractured

elements in the PNM-GFEM are approximated by

$$\boldsymbol{u}(x,y,t) = H(-f(x,y)) \sum_{I\in S_1} \Big(\psi_{I(0,0)}\boldsymbol{u}_{I(0,0)} + \sum_{k_x=1}^{n} [\psi^{C_x}_{I(k_x,0)}\boldsymbol{u}^{C_x}_{I(k_x,0)} + \psi^{S_x}_{I(k_x,0)}\boldsymbol{u}^{S_x}_{I(k_x,0)}] +$$

$$\sum_{k_y=1}^{m} [\psi^{C_y}_{I(0,k_y)}\boldsymbol{u}^{C_y}_{I(0,k_y)} + \psi^{S_y}_{I(0,k_y)}\boldsymbol{u}^{S_y}_{I(0,k_y)}] +$$

$$\sum_{k_x=1}^{n}\sum_{k_y=1}^{m} [\psi^{C+}_{I(k_x,k_y)}\boldsymbol{u}^{C+}_{I(k_x,k_y)} + \psi^{S+}_{I(k_x,k_y)}\boldsymbol{u}^{S+}_{I(k_x,k_y)} + \psi^{C-}_{I(k_x,k_y)}\boldsymbol{u}^{C-}_{I(k_x,k_y)} + \psi^{S-}_{I(k_x,k_y)}\boldsymbol{u}^{S-}_{I(k_x,k_y)}] \Big) +$$

$$H(f(x,y)) \sum_{I\in S_2} \Big(\psi_{I(0,0)}\boldsymbol{u}_{I(0,0)} + \sum_{k_x=1}^{n} [\psi^{C_x}_{I(k_x,0)}\boldsymbol{u}^{C_x}_{I(k_x,0)} + \psi^{S_x}_{I(k_x,0)}\boldsymbol{u}^{S_x}_{I(k_x,0)}] + \tag{3.17}$$

$$\sum_{k_y=1}^{m} [\psi^{C_y}_{I(0,k_y)}\boldsymbol{u}^{C_y}_{I(0,k_y)} + \psi^{S_y}_{I(0,k_y)}\boldsymbol{u}^{S_y}_{I(0,k_y)}] +$$

$$\sum_{k_x=1}^{n}\sum_{k_y=1}^{m} [\psi^{C+}_{I(k_x,k_y)}\boldsymbol{u}^{C+}_{I(k_x,k_y)} + \psi^{S+}_{I(k_x,k_y)}\boldsymbol{u}^{S+}_{I(k_x,k_y)} + \psi^{C-}_{I(k_x,k_y)}\boldsymbol{u}^{C-}_{I(k_x,k_y)} + \psi^{S-}_{I(k_x,k_y)}\boldsymbol{u}^{S-}_{I(k_x,k_y)}] \Big)$$

in which $\psi_{I(0,0)} = N_I$ and $\psi^{\gamma}_{I(k_x,k_y)} = N_I\phi^{\gamma}_{(k_x,k_y)}$, and $H(\cdot)$ is the step function. S_1 and S_2 are the set of nodes corresponding to each of the two superimposed elements; each of the two superimposed elements contain original real nodes and additional phantom nodes. In the framework of GFEM, both the real and phantom nodes have conventional and enriched degrees of freedom. For cracked elements, the wavelengths Λ_x and Λ_y are taken to be equal to the length of the superimposed paired elements (i.e., regular elements with real and additional phantom nodes) in x- and y-directions, respectively. This is because while only part of each superimposed element is used to model one side of the crack, the displacement and pressure fields are interpolated using nodal degrees of freedom located at the nodes on both sides of the crack.

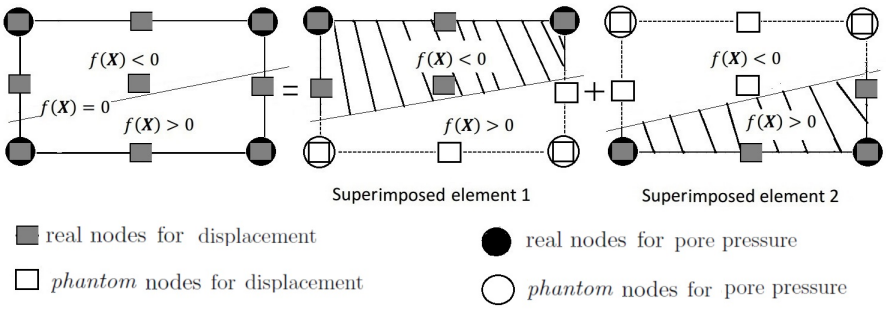

Fig. 3.1: Decomposition of a mixed cracked element into two superimposed elements, in which the underlying Lagrangian interpolants for the displacements and pore pressure are bi-quadratic (Q9) and bi-linear (Q4) shape functions, respectively. Real and phantom nodes with displacement degrees of freedom are shown using solid and hollow rectangles, respectively. Real and phantom nodes with pore pressure degrees of freedom are shown using solid and hollow circles, respectively.

3.3.2 Mixed GFEM-enriched Phantom Node Method (PNM-GFEM-M)

The PNM-GFEM approach is extended to the modelling of dynamic transient response of discontinuous porous media, in which discontinuities in both the displacement and pore pressure fields across the fracture surfaces occur. This is accomplished using an approximation analogous to (3.17) for the pore pressure.

It is noted that the employed trigonometric enrichment functions in [79] are not exclusively derived for linear elastic case and have been originally proposed in [78] for multi-scale electromagnetic and radio-frequency wave propagation in plasmas. Any type of transient or time-harmonic wave can be represented by exponential (or trigonometric) basis functions based on the Fourier concept and analytical solutions of waves. Hence in [78] the fundamental trig wave functions have been embedded in finite element interpolations as enrichments to mimic the transient/harmonic wave responses. In poroelastic case the response is a combination of diffusion and elastic wave process and the wave-type transient behaviour in displacement field is accompanied by a transient response in pore pressure field. Therefore, there is a coupled transient physics in both displacement and pore pressure variables that can be represented by harmonic functions (i.e., fundamental wave packages).

As illustrated in Figure 3.1, the underlying element for our approximation is a mixed element, with a bi-quadratic (nine node) approximation for the displacements and a bi-linear (four node) approximation for the pore pressure. The mixed element is replaced by two superimposed elements: superimposed element 1 (SE1) and superimposed element 2 (SE2). The nodes and corresponding displacement and pressure degrees of freedom of SE1 with $f((X) \leq 0)$ are inherited from the underlining element, while nodes of SE1 with $f((X) > 0)$ are additional phantom nodes with corresponding additional displacement and pressure degrees of freedom. In a similar way, the nodes of SE2 with $f((X) > 0)$ are inherited from the underlining element, while nodes of SE2 with $f((X) \leq 0)$ are additional phantom nodes.

Displacement field discretization

For a cracked element in a porous media, the displacement components in x and y directions are interpolated based on the discretization introduced above, in a more compact form as:

$$u_x(x,y,t) = H(-f(x,y)) \sum_{I \in S_1} \left(\boldsymbol{\psi}_I^1(x,y) \mathbf{u}_{Ix}(t) \right) + H(f(x,y)) \sum_{I \in S_2} \left(\boldsymbol{\psi}_I^1(x,y) \mathbf{u}_{Ix}(t) \right) \tag{3.18}$$

$$u_y(x,y,t) = H(-f(x,y)) \sum_{I \in S_1} \left(\boldsymbol{\psi}_I^2(x,y) \mathbf{u}_{Iy}(t) \right) + H(f(x,y)) \sum_{I \in S_2} \left(\boldsymbol{\psi}_I^2(x,y) \mathbf{u}_{Iy}(t) \right) \tag{3.19}$$

in which $\boldsymbol{\psi}_I^1$ and $\boldsymbol{\psi}_I^2$ are the arrays of conventional and enriched basis functions of node I for the displacement components in x and y directions, respectively. $\mathbf{u}_{Ix}$ and $\mathbf{u}_{Iy}$ are the vectors of corresponding conventional and enriched mixture displacement degrees of freedom of the porous media for node I in the x and y directions, respectively, as shown below.

$$\boldsymbol{\psi}_I^{1,2} = \begin{bmatrix} \psi_{I(0,0)} & \psi_{I(1,0)}^{C_x} & \dots & \psi_{I(n,m)}^{S-} \end{bmatrix} \tag{3.20}$$

$$\boldsymbol{u}_{Ix}^{\top} = [u_{Ix(0,0)}, u_{Ix(1,0)}^{C_x}, ..., u_{Ix(n,m)}^{S-}] \tag{3.21}$$

$$\boldsymbol{u}_{Iy}^{\top} = [u_{Iy(0,0)}, u_{Iy(1,0)}^{C_x}, ..., u_{Iy(n,m)}^{S-}] \tag{3.22}$$

The Lagrange interpolation functions ($\psi_{I(0,0)} = N_I$) are taken to be bi-quadratic shape functions ($Q9$).

Pore pressure field discretization

When the pore pressure in the cracked element is discontinuous, as when the crack faces are impervious or when the fluid pressure in the fracture is different than in the bulk, pore pressure is approximated by PNM type approximation.

Following the general idea of PNM-GFEM, the pore pressure approximation in discontinuous (pressure) elements is

$$p(x,y,t) = H(-f(x,y)) \sum_{I \in S_1} \left(\boldsymbol{\psi}_I^3(x,y) \boldsymbol{p}_I(t) \right) + H(f(x,y)) \sum_{I \in S_2} \left(\boldsymbol{\psi}_I^3(x,y) \boldsymbol{p}_I(t) \right) \tag{3.23}$$

in which $\boldsymbol{\psi}_I^3$ denotes the set of conventional and enriched interpolation functions for the pore pressure variable (i.e., the third unknown field of the problem), and $\boldsymbol{p}_I$ is the vector of corresponding regular and enriched, phantom or real pore pressure degrees of freedom for node I.

$$\boldsymbol{\psi}_I^3 = \left[\begin{array}{cccc} \psi_{I(0,0)} & \psi_{I(1,0)}^{C_x} & ... & \psi_{I(n,m)}^{S-} \end{array} \right] \tag{3.24}$$

It is noted that the Lagrange interpolation functions ($\psi_{I(0,0)} = N_I$) for the pore pressure filed are bi-linear shape functions ($Q4$).

3.3.3 Semi-discretized mixed FE equations

Substitution of the prescribed interpolation functions for the displacement fields (4.12)- (4.13) and pore pressure field (4.17) in the governing weak form (4.10)-(4.11) results in a semi-

discretized system of equations, which at the element level is

$$\sum_{J=1}^{n_{node}} \Big([M^e]^{11}_{IJ} \ddot{\mathbf{u}}^e_{Jx} + [K^e]^{11}_{IJ} \mathbf{u}^e_{Jx} + [K^e]^{12}_{IJ} \mathbf{u}^e_{Jy} + [K^e]^{13}_{IJ} \mathbf{p}^e_J \Big) = \mathbf{F}^e_{Iu_x}, \quad (I = 1, ..., n_{node}) \tag{3.25}$$

$$\sum_{J=1}^{n_{node}} \Big([M^e]^{22}_{IJ} \ddot{\mathbf{u}}^e_{Jy} + [K^e]^{21}_{IJ} \mathbf{u}^e_{Jx} + [K^e]^{22}_{IJ} \mathbf{u}^e_{Jy} + [K^e]^{23}_{IJ} \mathbf{p}^e_J \Big) = \mathbf{F}^e_{Iu_y}, \quad (I = 1, ..., n_{node}) \tag{3.26}$$

$$\sum_{J=1}^{n_{node}} \Big([M^e]^{31}_{IJ} \ddot{\mathbf{u}}^e_{Jx} + [M^e]^{32}_{IJ} \ddot{\mathbf{u}}^e_{Jy} + [C^e]^{31}_{IJ} \dot{\mathbf{u}}^e_{Jx} + [C^e]^{32}_{IJ} \dot{\mathbf{u}}^e_{Jy} +$$

$$[C^e]^{33}_{IJ} \dot{\mathbf{p}}^e_J + [K^e]^{33}_{IJ} \mathbf{p}^e_J \Big) = \mathbf{F}^e_{Ip}, \quad (I = 1, ..., n_{node}) \tag{3.27}$$

in which n_{node} is the number of nodes in each of the two superposed elements 1 and 2, and includes both original real and phantom nodes. It is noted that for the cracked elements, the numerical integration is performed separately over the active areas of each of the two superposed elements. To evaluate the finite element integrals a sub-domain integration scheme is employed [26].

In an element crossed by a crack, the definitions of $[M^e]_{IJ}$, $[C^e]_{IJ}$, $[K^e]_{IJ}$, $\mathbf{F}^e_{Iu_x}$, $\mathbf{F}^e_{Iu_y}$, and $\mathbf{F}^e_{Ip}$ in (4.19), (4.20), and (4.21) for each of the superimposed elements, i.e., e= 1 or 2, are

$$[M^e]^{11}_{IJ} = \int_{A_e} \rho (\boldsymbol{\psi}^1_I)^\top \boldsymbol{\psi}^1_J d\Omega, \quad [M^e]^{31}_{IJ} = \int_{A_e} \rho_f k_f (\boldsymbol{\psi}^3_I)^\top_{,x} \boldsymbol{\psi}^1_J d\Omega \tag{3.28}$$

$$[M^e]^{22}_{IJ} = \int_{A_e} \rho (\boldsymbol{\psi}^2_I)^\top \boldsymbol{\psi}^2_J d\Omega, \quad [M^e]^{32}_{IJ} = \int_{A_e} \rho_f k_f (\boldsymbol{\psi}^3_I)^\top_{,y} \boldsymbol{\psi}^2_J d\Omega \tag{3.29}$$

$$[K^e]^{11}_{IJ} = \int_{A_e} \Big(C_{11} (\boldsymbol{\psi}^1_I)^\top_{,x} (\boldsymbol{\psi}^1_J)_{,x} + C_{33} (\boldsymbol{\psi}^1_I)^\top_{,y} (\boldsymbol{\psi}^1_J)_{,y} \Big) d\Omega, \tag{3.30}$$

$$[K^e]^{12}_{IJ} = \int_{A_e} \Big(C_{12} (\boldsymbol{\psi}^1_I)^\top_{,x} (\boldsymbol{\psi}^2_J)_{,y} + C_{33} (\boldsymbol{\psi}^1_I)^\top_{,y} (\boldsymbol{\psi}^2_J)_{,x} \Big) d\Omega, \tag{3.31}$$

$$[K^e]^{13}_{IJ} = \int_{A_e} -\alpha_p(\boldsymbol{\psi}^1_I)^\top_{,x}(\boldsymbol{\psi}^3_J)d\Omega, \tag{3.32}$$

$$[K^e]^{21}_{IJ} = \int_{A_e} \Big(C_{21}(\boldsymbol{\psi}^2_I)^\top_{,y}(\boldsymbol{\psi}^1_J)_{,x} + C_{33}(\boldsymbol{\psi}^2_I)^\top_{,x}(\boldsymbol{\psi}^1_J)_{,y}\Big)d\Omega, \tag{3.33}$$

$$[K^e]^{22}_{IJ} = \int_{A_e} \Big(C_{22}(\boldsymbol{\psi}^2_I)^\top_{,y}(\boldsymbol{\psi}^2_J)_{,y} + C_{33}(\boldsymbol{\psi}^2_I)^\top_{,x}(\boldsymbol{\psi}^2_J)_{,x}\Big)d\Omega, \tag{3.34}$$

$$[K^e]^{23}_{IJ} = \int_{A_e} -\alpha_p(\boldsymbol{\psi}^2_I)^\top_{,y}(\boldsymbol{\psi}^3_J)d\Omega, \tag{3.35}$$

$$[K^e]^{33}_{IJ} = \int_{A_e} k_f\Big((\boldsymbol{\psi}^3_I)^\top_{,x}(\boldsymbol{\psi}^3_J)_{,x} + (\boldsymbol{\psi}^3_I)^\top_{,y}(\boldsymbol{\psi}^3_J)_{,y}\Big)d\Omega, \tag{3.36}$$

$$[C^e]^{31}_{IJ} = \int_{A_e} \alpha_p(\boldsymbol{\psi}^3_I)^\top(\boldsymbol{\psi}^1_J)_{,x}d\Omega, \tag{3.37}$$

$$[C^e]^{32}_{IJ} = \int_{A_e} \alpha_p(\boldsymbol{\psi}^3_I)^\top(\boldsymbol{\psi}^2_J)_{,y}d\Omega, \tag{3.38}$$

$$[C^e]^{33}_{IJ} = \int_{A_e} (\boldsymbol{\psi}^3_I)^\top(\boldsymbol{\psi}^3_J)\frac{1}{Q}d\Omega, \tag{3.39}$$

$$\mathbf{F}^e_{Iu_x} = \int_{A_e} \Big(\rho(b_x)(\boldsymbol{\psi}^1_I)^\top\Big)d\Omega + \int_{s^t_e} \Big(\bar{t}_x(\boldsymbol{\psi}^1_I)^\top\Big)d\Gamma_t + \int_{s^d_e} \Big(\bar{t}_{d_x}(\boldsymbol{\psi}^1_I)^\top\Big)d\Gamma_d, \tag{3.40}$$

$$\mathbf{F}^e_{Iu_y} = \int_{A_e} \Big(\rho(b_y)(\boldsymbol{\psi}^2_I)^\top\Big)d\Omega + \int_{s^t_e} \Big(\bar{t}_y(\boldsymbol{\psi}^2_I)^\top\Big)d\Gamma_t + \int_{s^d_e} \Big(\bar{t}_{d_y}(\boldsymbol{\psi}^2_I)^\top\Big)d\Gamma_d, \tag{3.41}$$

$$\mathbf{F}^e_{Ip} = \int_{A_e} k_f \rho_f \Big((\boldsymbol{\psi}^3_I)^\top_{,x} b_x + (\boldsymbol{\psi}^3_I)^\top_{,y} b_y \Big) d\Omega - \int_{s^w_e} \Big(\dot{w} \cdot n_{\Gamma w} (\boldsymbol{\psi}^3_I)^\top \Big) d\Gamma_w \tag{3.42}$$

in which e is either 1 or 2 for the superimposed elements one and two, respectively, and s^t_e, s^d_e, and s^w_e are the portions of superimposed element e on the traction boundary Γ_t, discontinuity surface Γ_d, and fluid flux boundary Γ_w, respectively. $\bar{t}_{d_x}$ and $\bar{t}_{d_y}$ are the components of contact tractions in x and y directions, respectively.

The semi-discretized coupled hydro-mechanical poro-elastic finite element equations (4.19), (4.20), and (4.21) can be rewritten in a more compact form as:

$$[M] \left\{ \ddot{\boldsymbol{\Delta}} \right\} + [C] \left\{ \dot{\boldsymbol{\Delta}} \right\} + [K] \{ \boldsymbol{\Delta} \} = \{ \mathbf{F} \} \tag{3.43}$$

where $\{\boldsymbol{\Delta}\} = \{ \mathbf{u}_x \;\; \mathbf{u}_y \;\; \mathbf{p} \}^\top$ is the vector of unknown nodal values for displacement and pore pressure degrees of freedom in the porous media, and $\{\mathbf{F}\} = \left\{ \mathbf{F}_{u_x} \;\; \mathbf{F}_{u_y} \;\; \mathbf{F}_p \right\}^\top$ is the vector of mechanical forces and flow fluxes.

3.3.4 Fully Discrete Equations

To establish the fully-discretized governing algebraic equations, the Generalized Newmark time integration schemes G22 and G11 are employed for displacement and pore pressure degrees of freedom, respectively. The following relations link the unknown values for displacement and pore pressure at time step $(i+1)$ to the corresponding values at time step (i)

$$\ddot{u}_{i+1} = \frac{1}{\beta \Delta t^2} (u_{i+1} - u_i) - \frac{1}{\beta \Delta t} \dot{u}_i - (\frac{1}{2\beta} - 1) \ddot{u}_i \tag{3.44}$$

$$\dot{u}_{i+1} = \frac{\gamma}{\beta \Delta t} (u_{i+1} - u_i) - (\frac{\gamma}{\beta} - 1) \dot{u}_i - \Delta t (\frac{\gamma}{2\beta} - 1) \ddot{u}_i \tag{3.45}$$

$$\dot{p}_{i+1} = \frac{1}{\theta \Delta t} (p_{i+1} - p_i) - (\frac{1}{\theta} - 1) \dot{p}_i \tag{3.46}$$

where γ, β, and θ are the integration parameters that are all considered to be 0.7 in the numerical examples of the present work. The integration constants are typically chosen in the range of [0 1]. For unconditional stability of the time integration θ and γ need to be greater than or equal to 0.5 and β should be greater than or equal to $0.25(0.5+\gamma)^2$.

For a prescribed set of initial and boundary conditions and surface tractions on the crack faces, which may include contributions from friction and contact forces, the substitution of (4.23-4.25) into (4.22) leads to a linear system of equations of the following form for the displacement and pressure degrees of freedom $\boldsymbol{\Delta}_{i+1}$ at time t_{i+1} in terms of known displacement and pressure degrees of freedom $\boldsymbol{\Delta}_i$ at time t_i.

$$\mathbf{A}\boldsymbol{\Delta}_{i+1} = \mathbf{R}\left(\boldsymbol{\Delta}_i, \bar{\mathbf{t}}, \bar{\mathbf{t}}_d, \bar{\mathbf{q}}\right) \tag{3.47}$$

in which the right hand side $\mathbf{R}$ is function of the degrees of freedom at time t_i, the external applied traction $\bar{\mathbf{t}}$, the crack surface tractions $\bar{\mathbf{t}}_d$, and the boundary flux $\bar{\mathbf{q}} = \dot{\boldsymbol{w}} \cdot \boldsymbol{n}_\Gamma$. In the next section, the calculation of the crack surface tractions stemming from friction and contact is discussed.

3.4 Augmented-Lagrangian frictional contact simulation

Geomechanical porous systems experience high in-situ confining stresses due to the overburden and horizontal stresses leading to large contact and frictional forces acting along natural fractures and faults. A considerable amount of attention has been given to how to enforce interfacial constraints in the context of the partition-of-unity FEM; a number of contact simulation methodologies and appropriate spacial and interfacial interpolation strategies have been developed leading to smoother and more stable contact results [123, 124, 125]. In this work, an augmented Lagrange multiplier approach is adopted to enforce the normal contact constraint via an iterative method.

When frictional contact between crack surfaces is incorporated into the model, it is convenient to rewrite the weak form (4.10) as

$$\int_{\Omega} \boldsymbol{\sigma} : \delta\boldsymbol{\varepsilon}\ d\Omega + \int_{\Omega} \rho\ddot{\boldsymbol{u}} \cdot \delta\boldsymbol{u}\ d\Omega - \int_{\Gamma_t} \bar{\boldsymbol{t}} \cdot \delta\boldsymbol{u}\ d\Gamma - \int_{\Omega} \rho\boldsymbol{b} \cdot \delta\boldsymbol{u}\ d\Omega - \int_{\Gamma_d} \bar{\lambda}_N \delta g_N d\Gamma -$$

$$\int_{\Gamma_d} \bar{\lambda}_T \delta g_T d\Gamma = 0 \tag{3.48}$$

in which $\bar{\lambda}_N$, g_N, $\bar{\lambda}_T$, and g_T are the normal contact traction, the normal inter-penetration, the tangential contact frictional traction, and the tangential displacement jump across the contact surface, respectively. It is noted that the inter-penetration (g_N) has been defined with a positive sign. Here $\bar{\lambda}_T$ is the friction stemming for a stick-slip friction model.

The normal contact and tangential frictional force/Lagrange multiplier fields are interpolated using one-dimensional elements along the discontinuity as:

$$\bar{\lambda}_N = \tilde{\mathbf{N}}\bar{\boldsymbol{\lambda}}_N \text{ and } \bar{\lambda}_T = \tilde{\mathbf{N}}\bar{\boldsymbol{\lambda}}_T \tag{3.49}$$

in which $\tilde{\mathbf{N}}$ are linear one-dimensional Lagrangian shape functions and $\left(\bar{\boldsymbol{\lambda}}_N, \bar{\boldsymbol{\lambda}}_T\right)$ are the vec-

tors of Lagrange multipliers degrees of freedom. The nodes of the Lagrange multiplier mesh are chosen using the Vital Vertex Method [124, 125].

At each time step, $\boldsymbol{\Delta}_{i+1}$ and $\left(\bar{\boldsymbol{\lambda}}_N, \bar{\boldsymbol{\lambda}}_T\right)_{i+1}$, given the solutions $\boldsymbol{\Delta}_i$ and $\left(\bar{\boldsymbol{\lambda}}_N, \bar{\boldsymbol{\lambda}}_T\right)_i$ at t_i, are sought using an iterative process. The iterative process starts ($k = 0$) with an initial guess for the vector of Lagrange multipliers $\left(\bar{\boldsymbol{\lambda}}_N, \bar{\boldsymbol{\lambda}}_T\right)_{i+1}^{k=0} = \left(\bar{\boldsymbol{\lambda}}_N, \bar{\boldsymbol{\lambda}}_T\right)_i$. Given $\left(\bar{\boldsymbol{\lambda}}_N, \bar{\boldsymbol{\lambda}}_T\right)_{i+1}^{k}$ at iteration k, the linear system of equations (3.47) is solved for $\boldsymbol{\Delta}_{i+1}^k$, from which the normal interpenetration g_N^k and tangential slip g_T^k of the crack at each node of the Lagrange multiplier mesh are computed. If the norm of g_N^k is greater than a prescribed tolerance then the Lagrange multiplier nodal vector (normal contact forces) are updated using

$$\bar{\boldsymbol{\lambda}}_N^{k+1} = \bar{\boldsymbol{\lambda}}_N^k + d\bar{\boldsymbol{\lambda}}_N^k, \quad and \quad d\bar{\boldsymbol{\lambda}}_N^k = K_N g_N^k \tag{3.50}$$

in which K_N is an arbitrary rebounding stiffness value.

In the case of frictional contact, a similar iterative update procedure is implemented to obtain the frictional (i.e., tangential) contact nodal forces. Sliding occurs, $g_T > 0$, if the tangential frictional contact force, $\bar{\lambda}_T$, required to prevent slip exceeds $\bar{\lambda}_T^{max} = \bar{\lambda}_N \mu_f$, otherwise a state of stick exists and the associated tangential slip, g_T, should be 0. When frictional contact is modelled, the iterative process is also conditioned on the norm of the tangential slip g_T at Lagrange multiplier nodes in a state of stick being less than a prescribed tolerance. When this condition is not satisfied, the Lagrange multiplier nodal vector associated with the stick-slip friction is updated using

$$\begin{cases} \bar{\boldsymbol{\lambda}}_T^{k+1} = \bar{\boldsymbol{\lambda}}_T^k + K_T g_T^k & \text{if } \bar{\lambda}_T < \bar{\lambda}_T^{max,k+1} \quad \text{(Stick Condition)} \\ \bar{\boldsymbol{\lambda}}_T^{k+1} = \bar{\lambda}_T^{max,k+1} & \text{otherwise} \qquad \text{(Slip Condition)} \end{cases} \tag{3.51}$$

in which $\bar{\lambda}_T^{max,k+1} = \bar{\lambda}_N^{k+1} \mu_f$ and K_T is an arbitrary rebounding stiffness.

By repeating the iterative process at each time step, the normal inter-penetration at the

crack location approaches zero as the vector of Lagrange multiplier, $\bar{\lambda}_N^{k+1}$, converges to the real magnitude of the contact force at the interface of the crack. In a similar way, the frictional contact forces converge to those satisfying the stick-slip condition. Once convergence of the iterative procedure is achieve, the solution algorithm proceeds to the next time step.

Table 3.1: Material properties of the porous media.

$E(Pa)$	ν	$\rho_s(kg/m^3)$	$\rho_f(kg/m^3)$	n'	$k_f(m^3s/kg)$	$K_f(Pa)$	$K_s(Pa)$
14.516×10^6	0.3	2000	1000	0.3	1.0194×10^{-6}	2.1×10^9	1×10^{20}

3.5 Results and discussion

In this section, different types of dynamic and transient wave propagation problems are simulated in poroelastic domains. The domain of analysis is assumed to be a two-dimensional poroelastic media with hydro-mechanical properties given in Table 4.1, unless stated otherwise. A unit thickness is assumed in the out-of-plane direction.

3.5.1 Verification study - Consolidation

To verify the accuracy and reliability of the developed enriched finite element model in solving dynamic transient poroelastic problems, the results obtained using the enriched FE model of the present work (with $n = 1$) is compared with some available results from the literature. To this end, as shown schematically in Figure 3.2 a vertical column of small width is considered under uniformly applied external traction on its top surface. The side walls and the bottom are assumed to be impervious and there is normal displacement restriction on them. The upper boundary is drained (there is essential boundary condition for p, i.e., p=0) and under compressive normal uniform traction of 3 kN/m^2. The width and length of the porous column are $0.1m$ and $10m$, respectively, and a one dimensional coordinate system is set on the domain with its origin at the bottom of the vertical column. Sixty rectangular $Q4$ elements with bi-linear polynomial interpolations have been considered to model this problem. Figures 3.3 and 3.4 show the velocity and pore pressure time histories of the transient response in the domain for particular control points on the column. As seen in these figures, a very close agreement is observed between the results of the numerical model of this work and those reported in [109].

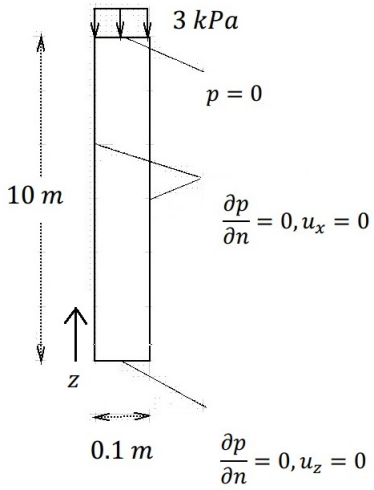

Fig. 3.2: A schematic picture of the porous column used for the validation study.

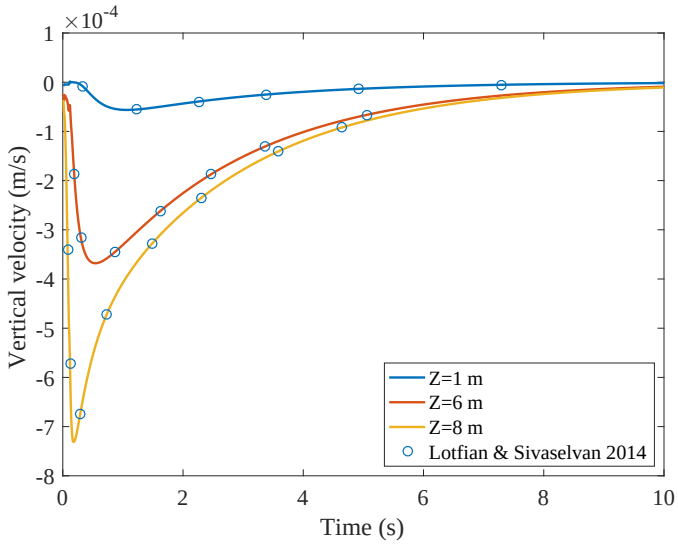

Fig. 3.3: A comparison study of the proposed enriched FE model with [109] on the variation of point velocity over time for vertical column of porous media.

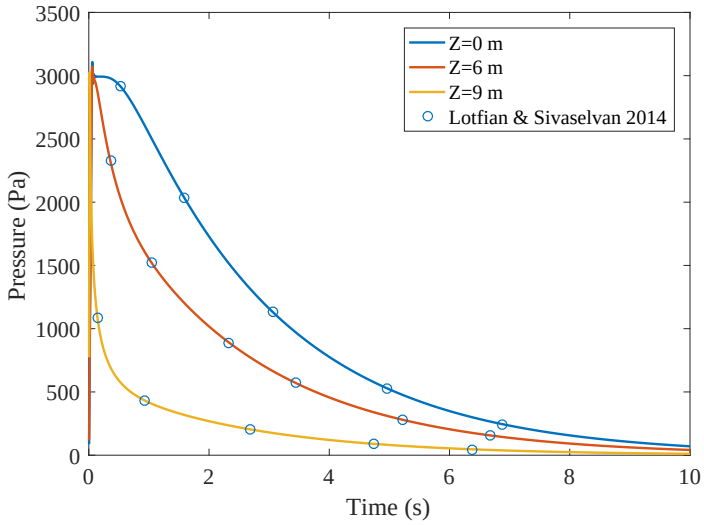

Fig. 3.4: A comparison study of the proposed enriched FE model with [109] on the variation of pore pressure over time for vertical column of porous media.

3.5.2 Dynamic response of fractured porous media under external traction-

To investigate the effect of discontinuity on the dynamic response of porous media, a $1m \times 0.1m$ poroelastic domain discretized by 30×10 $Q4$ mesh is considered. The domain contains a vertical crack of length $0.06m$ centered at $x = 0.5m$. The crack faces are assumed to be hydraulically impervious. Simulations with and without crack surface contact are modeled and are compared to the case of a continous intact domain. A uniform traction is imposed on the left side of the domain ($x = 0$) as:

$$\bar{t}_x(t) = \begin{cases} 3000 \times \frac{t}{0.1}[N/m^2] & \text{if } t \leqslant 0.1s; \\ 3000 & \text{if } t > 0.1s. \end{cases} \tag{3.52}$$

The top, bottom, and right edges of the domain are assumed to be impervious and the normal displacements to these edges are constrained. The left edge of the domain is fully drained. The domain, crack geometry, and the boundary conditions are shown in Figure 3.5.

In this problem long term dynamic response is investigated, which is comprised of lower frequency components. This is in contrast with the early time dynamic response, which is com-

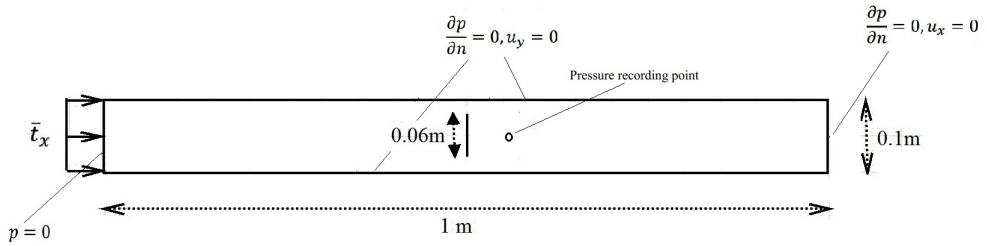

Fig. 3.5: A schematic figure of the porous media of section 4.5.1.

prised of higher frequency components. In the case of the former long term dynamic behaviour, the regular (uneriched) PNM model can be employed to accurately model the porous media.

Figure 3.6a illustrates the x-displacement contour of fractured domain at $t = 0.16\ s$ when contact between the crack faces is modeled. As seen in this contour plot, the contact no-interpenetration constraint is satisfied across the crack faces. On the other hand, as expected, neglecting the contact condition along the fracture faces results in a discontinuous displacement field, results for which are shown in Figure 3.6b. Neglecting the contact traction results in a higher magnitude of peak displacement in the field compared to the case in which the contact problem is accounted for. Figure 3.6c illustrates the differences between the response of the fractured porous media along the center-line, $y = 0.05$, with and without contact modeled along the crack faces. When contact is modeled the displacements normal to the crack are continuous, whereas when contact is not modeled the displacements are discontinuous across the crack.

Figures 3.7a, 3.7b, and 3.8 illustrate, respectively, the pore fluid velocity contour in x-direction, pore fluid velocity streamlines, and normal strain in the x-direction (ε_{xx}) at $t = 0.08s$ using 90×60 $Q4$ mesh. As seen in Figures 3.7a and 3.7b, because of the existence of an impervious crack, the streamlines go around the fracture and the velocity of the fluid perpendicular to the fracture at the interface of the discontinuity is zero (no fluid flux goes through the fracture). As seen in Figure 3.8 the strain magnitude at the fracture surface region is zero due to the traction-free interface assumption.

To further demonstrate the effect of the existence of crack on the hydraulic response of porous media, Figures 3.9a and 3.9b illustrate the pore pressure distribution through the frac-

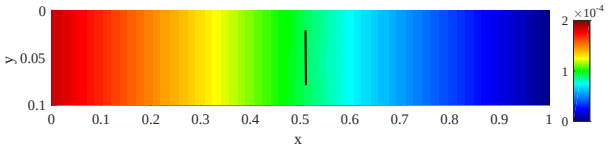

(a) with contact traction along crack faces

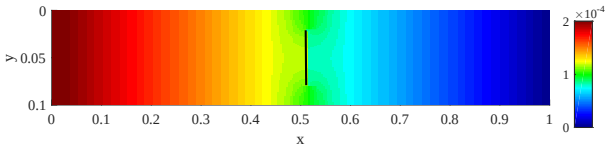

(b) with no contact traction along crack faces

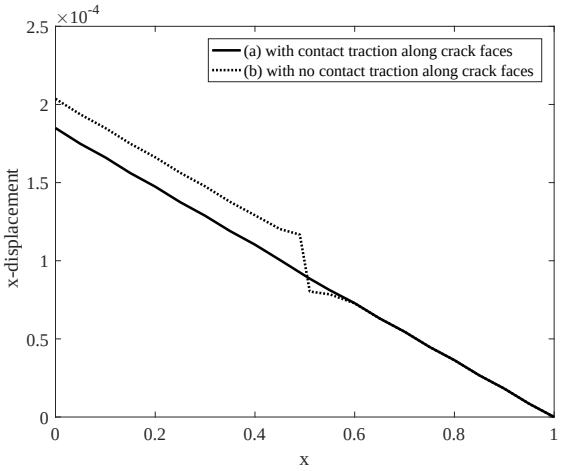

(c) 2D plot of x-displacement along the center-line (i.e., y=0.05)

Fig. 3.6: x-displacement under external uniformly distributed loading on the left edge at ($t = 0.16\ s$).

tured and intact domain, respectively. In the case of fractured domain it was assumed that the crack faces were completely impervious. As seen, the discontinuity in the pore pressure across the fracture is clear in Figure 3.9b while Figure 3.9a exhibits a continuous distribution for pore pressure. Moreover, due to the impermeability of crack faces, the maximum pore pressure of the domain (behind the crack) is higher than that of the intact media with no crack after the pore fluid begins to be discharged from the domain through the drained surface (left edge). This phenomenon happens due to the trapping of the pore fluid behind the fracture in the discharge process which makes the fluid discharge slower compared to the case with no crack. Figure 3.10 shows the time history of the pore pressure at a particular point in the domain ($x = 0.5667\ m, y = 0.05\ m$) behind the fracture. The impermeability of crack faces results in higher peak pressure in the cracked domain compared to the intact media. Due to the existence of drained hydraulic boundary condition at the left edge, as the system moves forward the pore pressure gradually tends to zero in steady state condition.

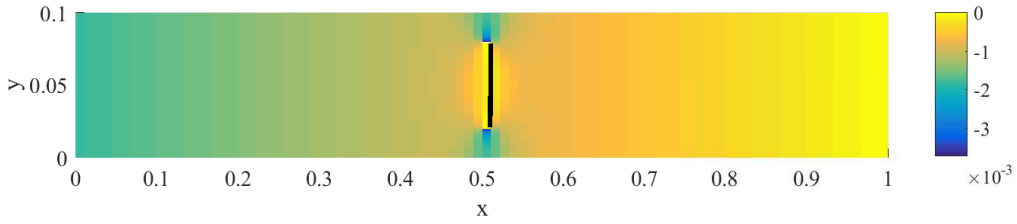

(a) Velocity contour in x-direction.

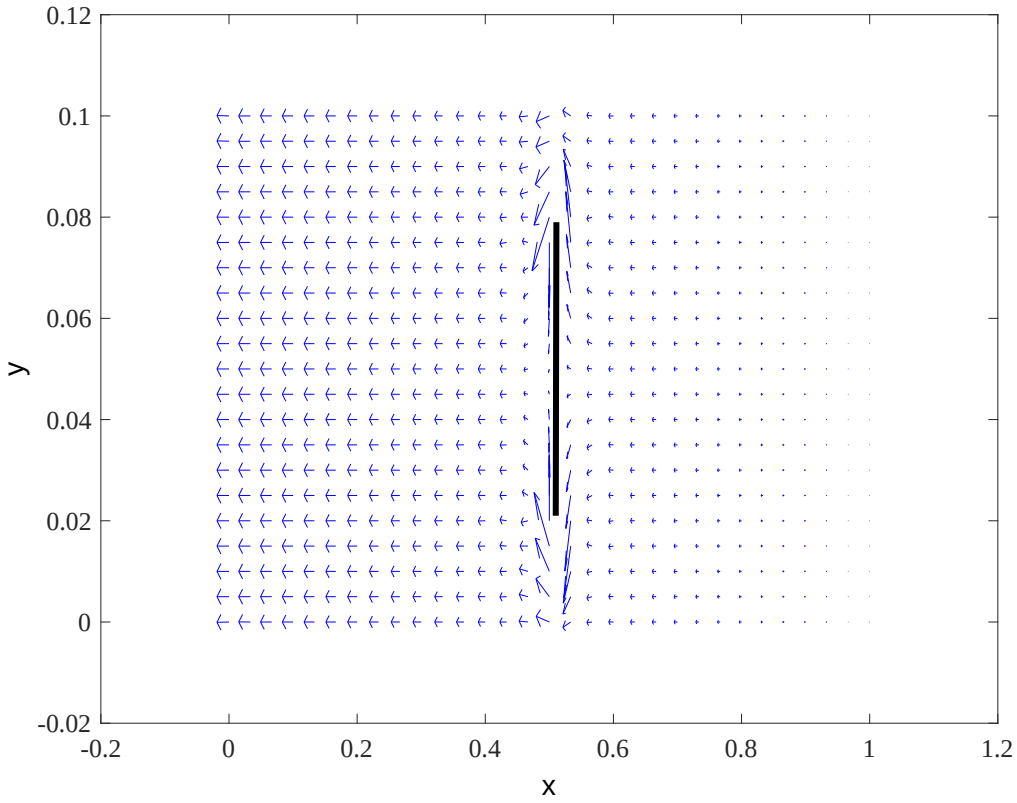

(b) Velocity streamlines.

Fig. 3.7: Pore fluid velocity at $t = 0.08s$.

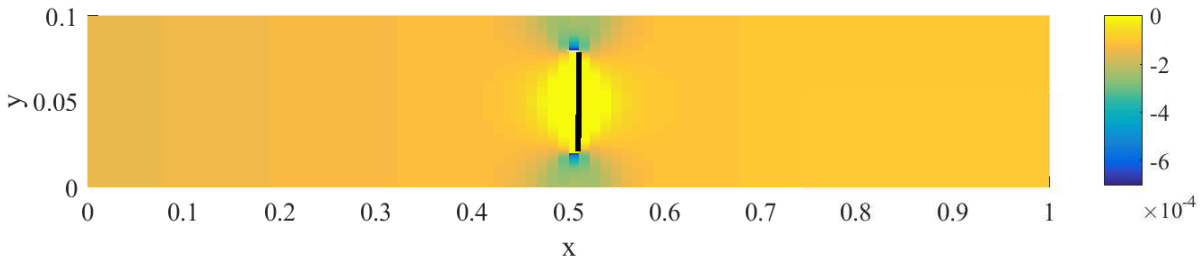

Fig. 3.8: Strain contour (ε_{xx}) at $t = 0.08s$.

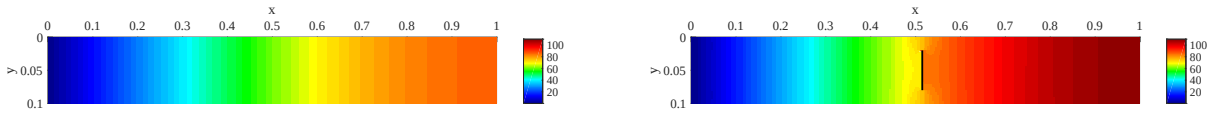

(a) Intact domain with no fracture

(b) Fractured domain with contact

Fig. 3.9: Pore pressure distribution under external uniformly distributed loading on the left edge at ($t = 0.16\ s$).

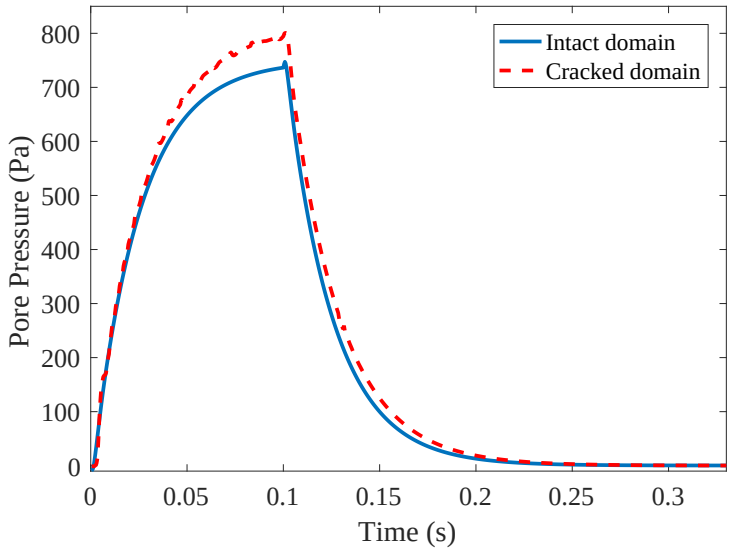

Fig. 3.10: Time history of pore pressure at point ($x = 0.5667\ m, y = 0.05\ m$) for cracked and intact domains.

3.5.3 Dynamic response of fractured porous media under point injection

To investigate the transient response of fractured porous media under hydraulic stimulation, a $1m$ by $1m$ domain (illustrated schematically in Figure 3.11) is considered under point injection at the center of the domain. The system is discretized by a 10×10 $Q4$ rectangular mesh. The boundaries are fully drained and are assumed to be traction-free with no displacement constraints. The problem is solved for the cases of discontinuous and intact domain. For the case of discontinuous media a vertical crack of $0.6m$ length is embedded at $x = 0.65m$. The problem is investigated under impervious as well as permeable crack face conditions. Contact

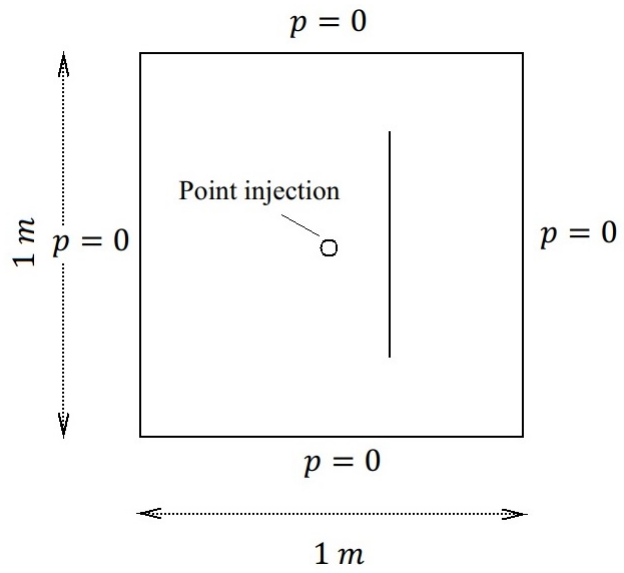

Fig. 3.11: Schematic picture of porous media under point injection.

constraints are considered for the cases in which there exists a crack. Due to the diffusive nature of this hydraulically-stimulated problem, regular PNM is used for the simulation.

To asses the effect of the hydraulic loading rate on the dynamic response of the system, two types of point injection rates are considered as:

- Case 1 (rapid injection):

$$\bar{q}(t) = \begin{cases} 0.01 \times \frac{t}{1\times10^{-4}}[m^3/s] & \text{if } t \leqslant 1 \times 10^{-4}s; \\ 0.01 & \text{if } t > 1 \times 10^{-4}s. \end{cases} \tag{3.53}$$

- Case 2 (slow injection):

$$\bar{q}(t) = \begin{cases} 0.01 \times \frac{t}{100\times10^{-4}}[m^3/s] & \text{if } t \leqslant 100 \times 10^{-4}s; \\ 0.01 & \text{if } t > 100 \times 10^{-4}s. \end{cases} \tag{3.54}$$

Figures 3.12a and 3.12b illustrate the early responses of the pore pressure at the mid-point of the domain as a function of time for two different injection rates into fractured and intact (continuous) domains. For the case of rapid injection, a peak-pressure point exist in the pore pressure time history. After the peak-pressure, the pore pressure abruptly drops-off before

gradually increasing to a steady-state value. The pressure peak in the high injection rate simulation are a result of the initially undrained behaviour of the porous media. In contrast, under slow injection the pore pressure increases in a nearly monotonically way towards a steady-state. The pore pressure response of an intact domain under both rapid and slow injection are also illustrated in Figures 3.12a and 3.12b. In both cases, the pore pressure response of the intact domain falls beneath that of the fractured domain. This behaviour is reasonable, since the cracks were assumed to be impervious and so the effective hydraulic conductivity of the fractured domain is less than that of the intact (continuous) domain. As a means to further verify the PNM and contact implementations, the simulated hydraulic response of the fractured media with fully-permeable crack surfaces is also included in Figure 3.12b. The responses of the fractured media with fully-permeable crack surfaces and contact is almost identical to that of intact domain, as would be expected.

3.5.4 Dynamic response under point injection in porous media with multiple fractures

To demonstrate the applicability of the developed model in hydro-mechanical simulation of porous media with multiple fractures, Figure 3.13 exhibits the pore pressure contour of a domain with three cracks as shown in the figure. The domain is considered to be under Case 2 type of point injection as represented in the preceding example in section 3.5.3. In the example PNM is used to introduce impermeable fractures. The domain is discretized by a 20×20 $Q4$ rectangular mesh. To specify the geometry of the fractures of this model the starting and finishing points of the cracks are given. For the vertical crack: ($x_{starting} = 0.3m, y_{starting} = 0.2m$) and ($x_{finishing} = 0.3m, y_{finishing} = 0.8m$); for the first sloping crack: ($x_{starting} = 0.5m, y_{starting} = 0.1m$) and ($x_{finishing} = 0.67m, y_{finishing} = 0.4m$); and for the second sloping crack: ($x_{starting} = 0.67m, y_{starting} = 0.6m$) and ($x_{finishing} = 0.5m, y_{finishing} = 0.9m$). Figure 3.13 shows a snapshot of pore pressure distribution at $t = 0.055s$. As expected, the

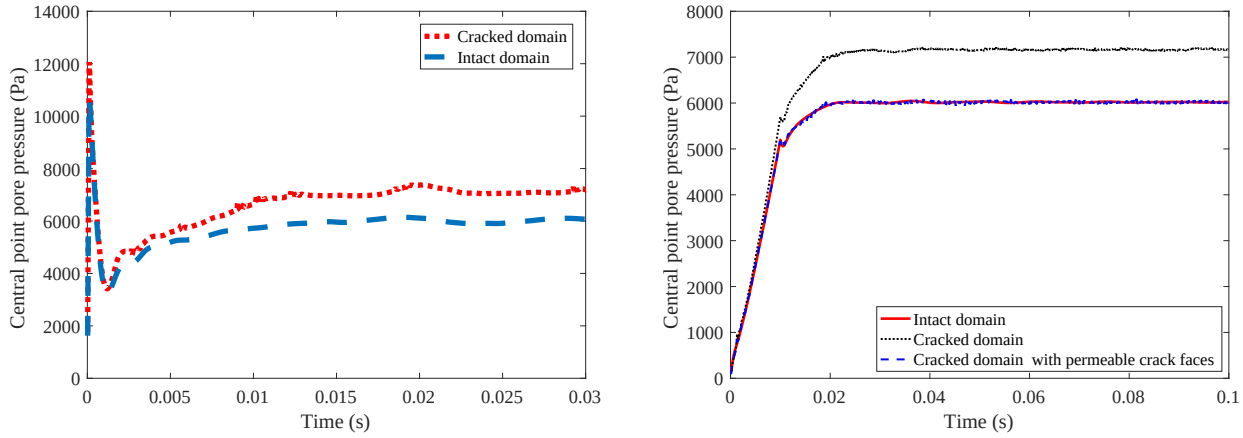

(a) Case 1 point injection (rapid injection)

(b) Case 2 point injection (slow injection)

Fig. 3.12: Pore pressure time history under point injection.

figure shows a discontinuous distribution for the pore pressure due to the impermeability assumption on crack faces.

3.5.5 Stick-slip frictional contact behaviour of fractured porous media

To examine the ability of the developed FE model to simulate frictional contact phenomenon in porous media a $1m \times 0.1m$ domain with a tilted crack is considered, as schematically shown in Figure 3.14. The crack faces are assumed to be impervious. A time dependent traction of the following form is applied on the left side ($x = 0$) of the domain.

$$\bar{t}_x(t) = \begin{cases} 3000 \times \frac{t}{0.1}[N/m^2] & \text{if } t \leqslant 0.1s; \\ 3000 & \text{if } t > 0.1s. \end{cases} \tag{3.55}$$

Top, bottom, and right boundaries are assumed to be impervious and normal displacements are restricted. The left edge is hydraulically open. In this problem long term dynamic response is investigated, which is comprised of lower frequency components. This is in contrast with the early time dynamic response, which is comprised of higher frequency components. In the

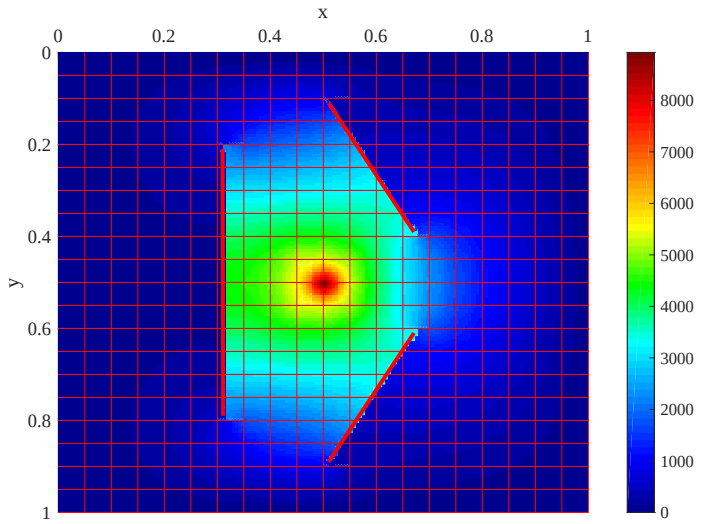

Fig. 3.13: Pore pressure distribution under point injection at $t = 0.055s$ in porous media with multiple fractures.

case of the former long term dynamic behaviour, the regular (uneriched) PNM model can be employed to accurately model the porous media.

To simulate different frictional contact behaviour, from full-slip to perfect-stick conditions, four different friction coefficients of $\mu_f = 0.00$, $\mu_f = 0.05$, $\mu_f = 0.10$, and $\mu_f = 0.50$ are examined. Results for each of these coefficients are shown in Figures 3.15a, 3.15b, 3.15c, and 3.15d, respectively. Figure 3.15e shows the variation of x-displacements as a function of x along the center-line (i.e., $y = 0.05$) for different friction coefficients. As the friction coefficient increases the magnitude of the displacement discontinuity decreases. As can be observed, by increasing the friction coefficient magnitude from 0 to 0.5, the contact behaviour of the system changes from the condition of fully-slip to perfect-stick response.

3.5.6 Wave propagation in porous media: Regular vs enriched FE

In this section the ability of the proposed PNM-GFEM-M model in simulating transient wave propagation is assessed for the case of velocity impact problem in continuous and fractured porous media. The results are compared with regular FEM/PNM simulations to demonstrate

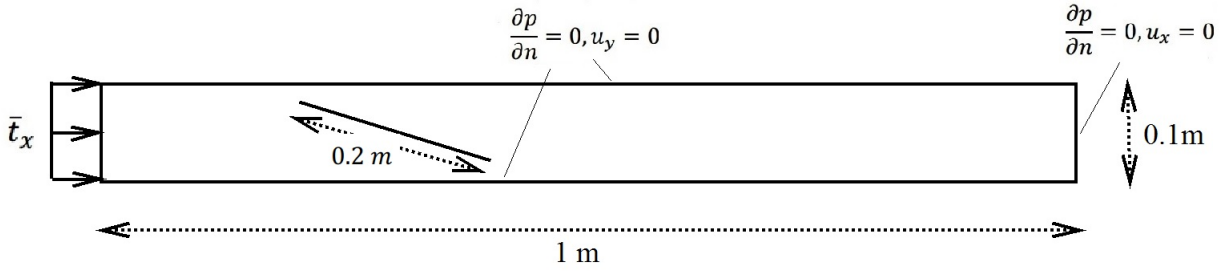

Fig. 3.14: Schematic picture of porous media with inclined crack.

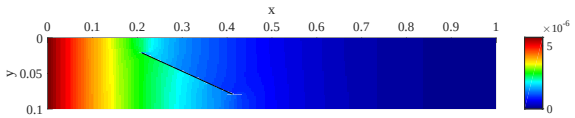

(a) $\mu_f = 0.00$ (no friction- slip behaviour)

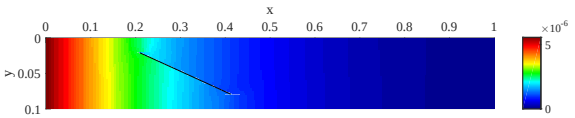

(b) $\mu_f = 0.05$ (stick-slip behaviour)

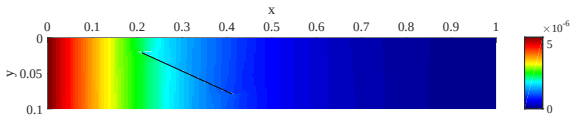

(c) $\mu_f = 0.10$ (stick-slip behaviour)

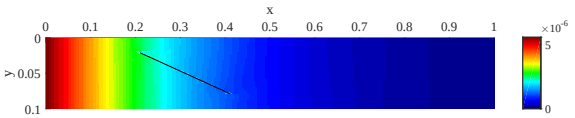

(d) $\mu_f = 0.50$ (stick behaviour)

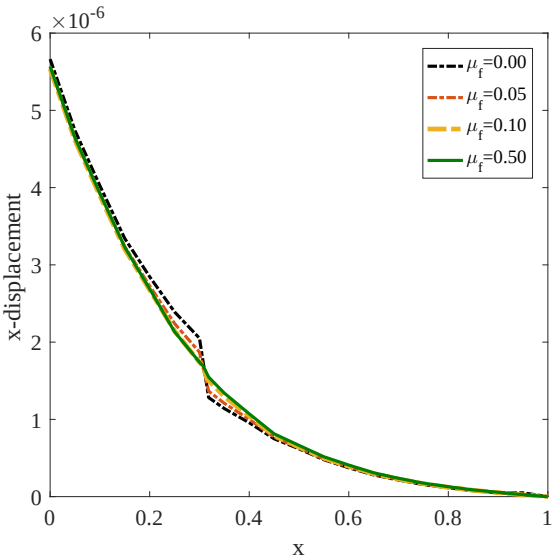

(e) 2D plot of x-displacement along the center-line (i.e., y=0.05)

Fig. 3.15: x-displacement under frictional contact.

the capability of the developed enriched FE model in suppressing the high-frequency spurious oscillations in both displacement and pore pressure variables. In the numerical simulations of this section, bi-quadratic ($Q9$) and bi-linear ($Q4$) polynomials are used as shape functions for interpolation of the displacement and pore pressure fields, respectively.

Impact problem in continuous media

The fixed-velocity impact phenomenon is known to be a good benchmark problem to examine the accuracy of a developed finite element method for wave propagation[79]. To demonstrate the ability of the developed enriched finite element model in solving the problem of transient wave propagation in porous media a poroelastic domain of $6m \times 0.1m$ is considered. An impact mechanical load is applied on the left edge of the domain and is imposed in the form of a fixed velocity boundary condition of $\dot{u}_x = 1m/s$. All the boundaries are considered to be fully-drained and with displacement restrictions normal to the domain. The considered domain, the boundary conditions, and the loading are exhibited schematically in Figure 3.16.

The impact problem investigated here is similar to the benchmark problem for evaluating the accuracy of dynamic finite element analysis for non-porous media [79]. In the case of non-porous media, it is known that the velocity response is a step function with no oscillations. In the case of porous media, we are not aware of the existence of an analytical solution for this problem. However, it's expected that the velocity response of the solid matrix will be similar to the non-porous media case, but that the response will be a step-like function with a steep but non-infinite slope. The slope of the step-like function is expects to decrease as the wave propagates due to diffusion of the fluid in the porous media. The expected behaviour of the pore pressure is also non-oscillatory. The compressive wave in displacement/velocity field stimulates pore pressure at the wave front. The induced pore pressure at the velocity front is then expected to decay over time due to diffusion. Hence, it is physically sensible to see a moving pulse, free from oscillations in the pore pressure during the wave propagation.

For a 20×2 mesh, Figures 3.17 and 3.18 illustrate the time histories at the center of the

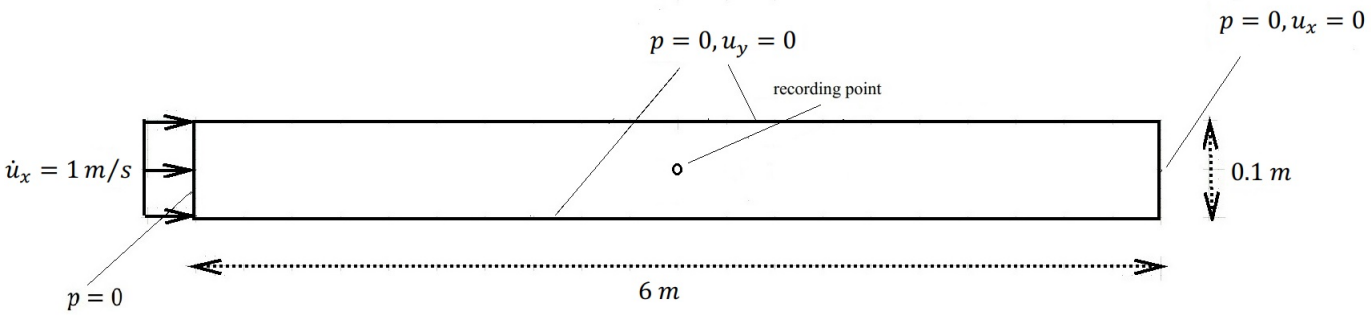

Fig. 3.16: Schematic picture of porous media under velocity impact loading.

domain at ($x = 3m,\ y = 0.05m$) for x-velocity and pore pressure, respectively. Comparing the results of conventional/unenriched FEM with those obtained using the GFEM model of this work demonstrates the shortcoming and deficiency of regular/conventional FE models and also, the requirement for employing enriched/unconventional finite element models for wave propagation analysis of porous media. As can be seen in both figures, the velocity and pore pressure curves exhibit high-frequency non-physical spurious oscillations over time in the case of conventional FEM. However, the oscillations (numerical dispersions that appear due to the Gibbs phenomenon) can be significantly suppressed by employing the GFEM model. In other words, using the GFEM model for porous media results in much more accurate wave patterns in both velocity and pore pressure fields. In Figure 3.17 it can be observed that using the GFEM model leads to a velocity-time profile that is very close to the step-function response, which is the analytical solution of this impact problem.

It is very important to note that in Figure 3.18 the results of the GFEM model have been provided for different types of enrichments for the displacement field (u) and pore pressure field (p). As seen in this figure, the most accurate results for pore pressure wave pattern are obtained when both displacement and pressure fields are enriched using trigonometric basis function in the context of GFEM. The GFEM models that are enriched only in the displacement field exhibit relatively more oscillations compared to the GFEM models that are enriched for both displacement and pore pressure. Moreover, increasing the cutoff number of enriched basis func-

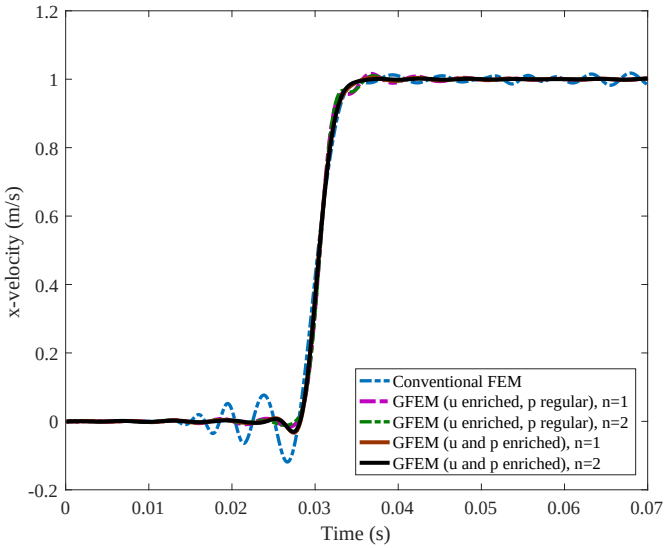

Fig. 3.17: Time history for x-velocity at the mid point of the porous media under impact loading. Conventional FEM Vs the developed GFEM model of this work with different types of enrichment for displacement and pore pressure fields.

tions embedded in the GFEM model leads to the wave results with fewer spurious oscillations and subsequently to more accurate solutions. Figure 3.19 shows the wave propagation results of pore pressure for a longer period of time. In this case, the effect of wave reflection from boundaries are observed. As seen, when using the conventional FEM model the non-physical oscillations exist for primary emitted wave (the very first pulse) as well as the waves reflected from the boundaries (the second pulse onward). The effect of physical damping/dissipation (which is attributed to the viscous pore fluid) is apparent from the attenuation of the pressure pulse as the wave travels. Also it is observed that the spurious oscillations tend to gradually subside over time due to this attenuation.

Figure 20 demonstrates a convergence study of regular FE approach for the impact problem. Different mesh resolutions are considered to simulate the wave propagation response. As seen, the conventional FEM approach shows noticeable numerical dispersions and oscillations even for highly refined meshes. However, the refined regular finite element solutions are converging (qualitatively) to enriched finite element result (see Figure 3.18). In Figure 3.20 the regular

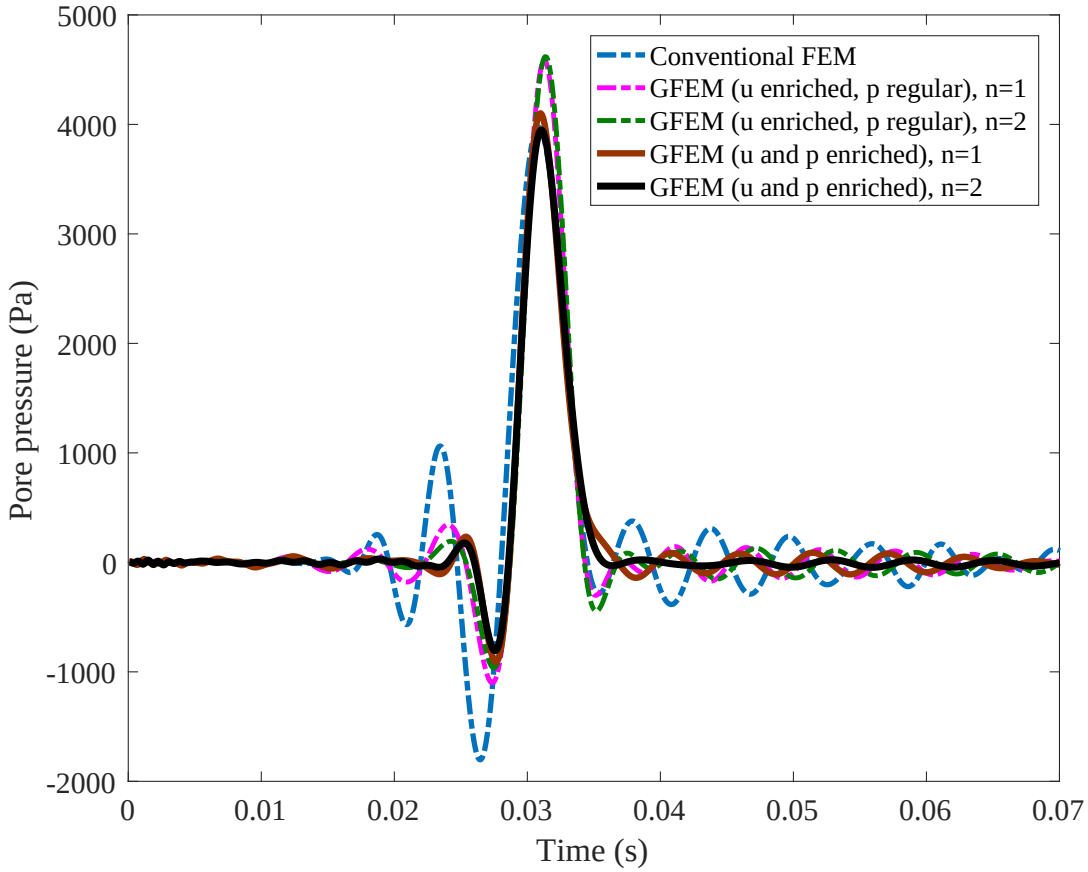

Fig. 3.18: Time history for pore pressure at the mid point of the porous media with $K_f = 1.0194 \times 10^{-6}$ under impact loading. Conventional FEM Vs the developed GFEM model of this work with different types of enrichment for displacement and pore pressure fields.

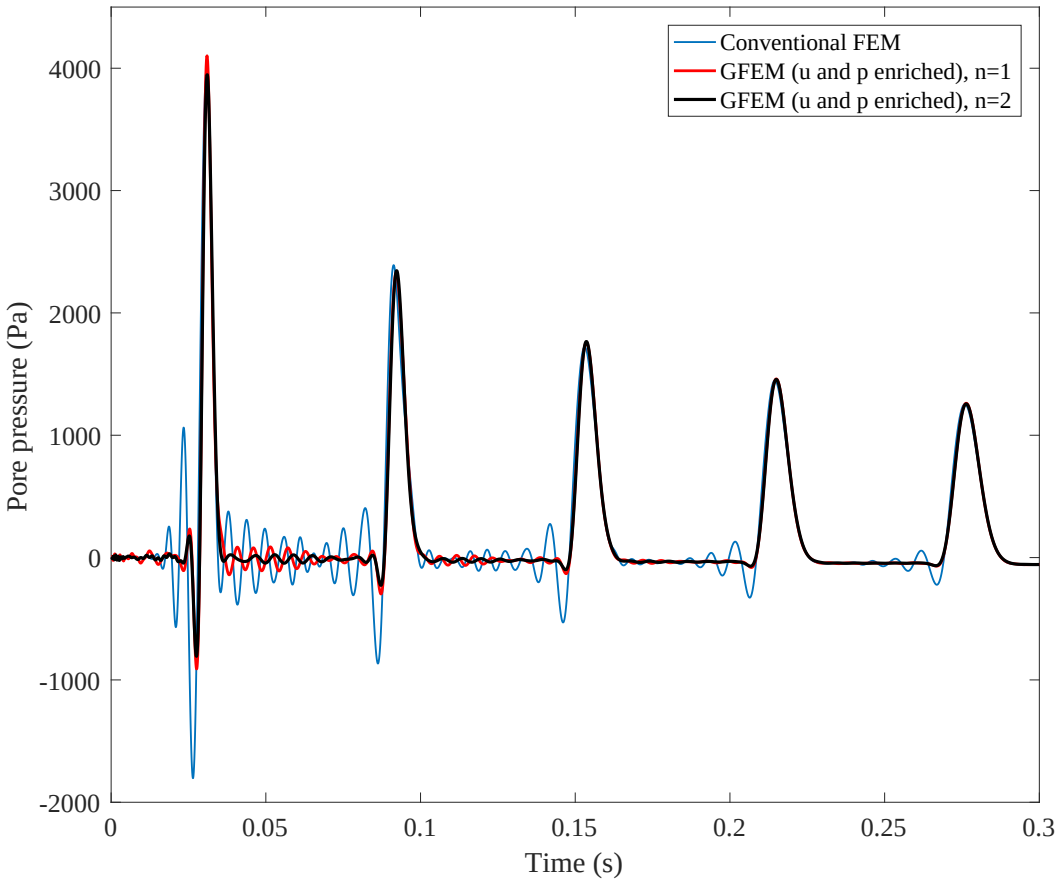

Fig. 3.19: Time history of pore pressure at the mid point of the porous media under impact loading with wave reflection from the boundaries. Conventional FEM Vs the developed GFEM model of this work.

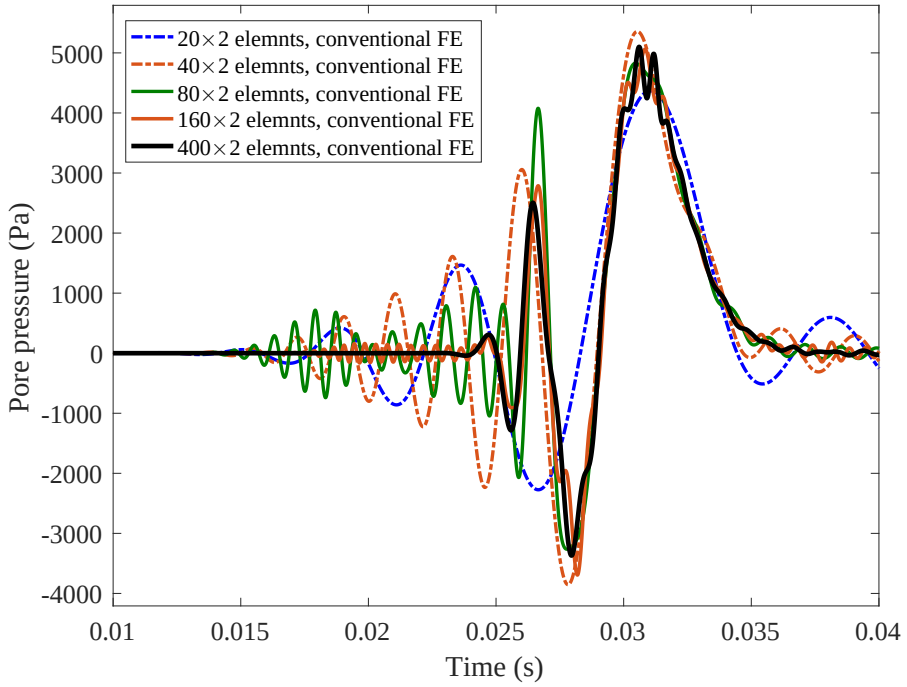

Fig. 3.20: Convergence study of conventional FE approach for pore pressure at the mid point.

FEM model with the highest mesh resolution (400×2 elements) has 12015 degrees of freedom while in Figure 3.18 the GFEM model with the coarsest mesh resolution (20×2 elements with $n = 1$) has 1435 degrees of freedom. Although the number of degrees of freedom in regular FEM simulation is more than 8 times higher than that of the enriched GFEM model, the enriched model provides more accurate (spurious oscillation-free) results. Moreover, the computational cost of the simulation using the mentioned enriched GFEM model is proportionally lower than that of the regular FEM simulation.

Role of Permeability

To assess the effect of the permeability parameter on wave propagation response of porous media, Figure 3.21 shows the pore pressure time history of the same problem for a lower permeability/diffusivity porous media case ($K_f = 1.0194 \times 10^{-7}$). As seen, lower values for permeability results in higher peak pore pressures. Moreover, regular FE analysis of porous media with lower permeability shows even relatively less oscillations compared with the pre-

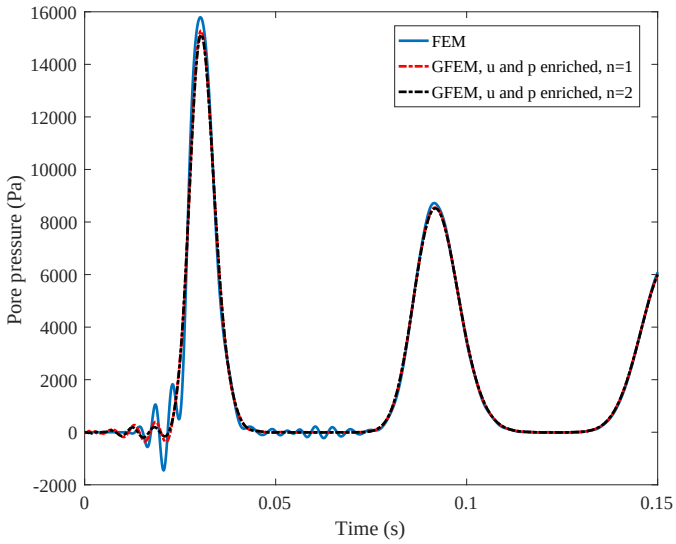

Fig. 3.21: Time history of pore pressure at the mid point of the porous media under impact loading with wave reflection from the boundaries with $K_f = 1.0194 \times 10^{-7}$. Conventional FEM Vs the developed GFEM model of this work.

ceding case with $K_f = 1.0194 \times 10^{-6}$ since the hydraulic behaviour is closer to undrained, as the permeability decreases.

To have a better intuitive understanding to the effect of permeability on transient wave propagation response of porous media, Figures 3.22 through 3.25 show the wave propagation responses for pore pressure and velocity variables at the mid point of the media for various values of permeability. Comparing the figures reveals the crucial effect of diffusivity value on wave propagation behaviour. As is clear in the figures, decreasing the permeability of porous media results in the reduction of the frequency of pressure wave/pulse. Also, the long-term pore pressure is dependent on permeability. In other words, for low permeability media (Figure 3.24) there is a positive non-zero steady-state pore pressure. Whereas for the higher permeability cases (Figures 3.22 and 3.23) the pressure keeps its periodic trend of the wave pulse in which the peak value is monotonically decreasing. Moreover, the results show the highest rate of attenuation/dissipation for the lowest permeable case.

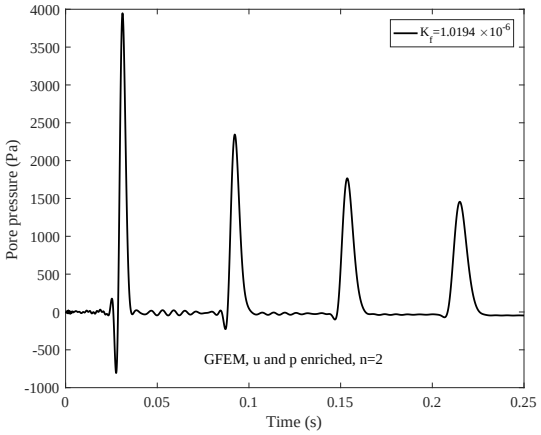

Fig. 3.22: Time history of pore pressure under impact loading for $K_f = 1.0194 \times 10^{-6}$.

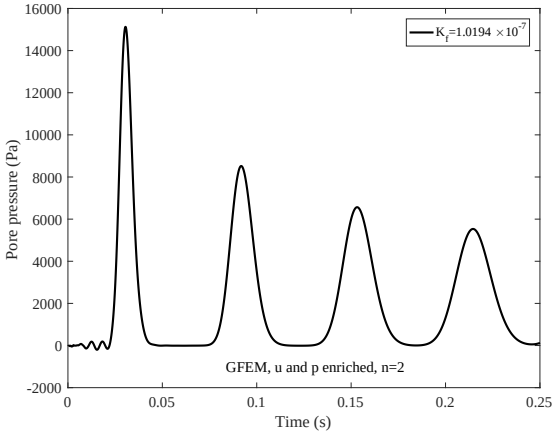

Fig. 3.23: Time history of pore pressure under impact loading for $K_f = 1.0194 \times 10^{-7}$.

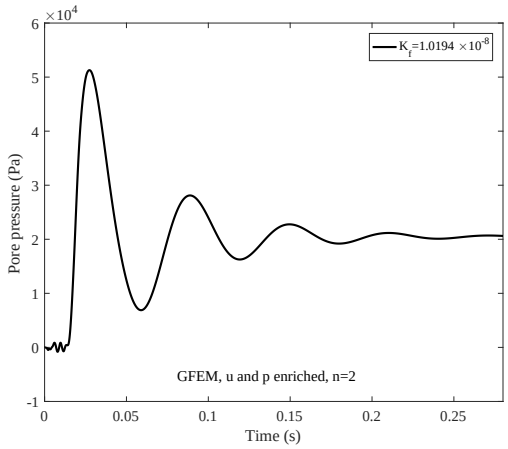

Fig. 3.24: Time history of pore pressure under impact loading for $K_f = 1.0194 \times 10^{-8}$.

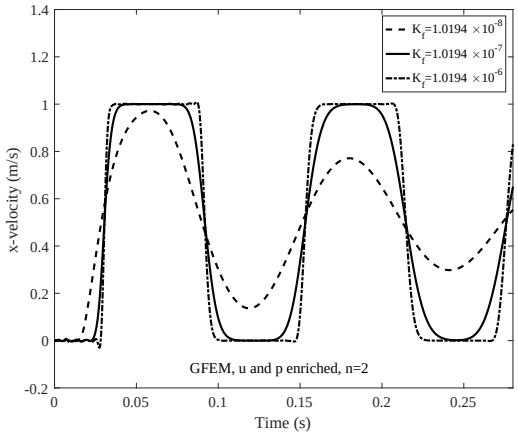

Fig. 3.25: Time history of velocity under impact loading for various values of permeability.

Impact problem in fractured media

To demonstrate the transient wave propagation response in a cracked porous media under impact loading (the same velocity impact loading of the earlier example is considered) and to investigate the interaction of hydro-mechanical wave pulse with fracture, a cracked poroelastic domain of $3m \times 0.5m$ with $k_f = 1.631 \times 10^{-6} m^3 s/kg$ is considered. Contact constraints across the fracture are satisfied through the ALM technique and the crack face are assumed to be impervious. The domain is discretized by a 20×10 rectangular mesh. A $0.3m$ long nearly vertical crack, inclinded at an angle of 3.6×10^{-2} radians, is embedded in the media centered at $x = 1.1m$.

Figures 3.26a and 3.26b exhibit wave pattern for pore pressure distribution using the conventional PNM and the enriched PNM-GFEM-M model of this work ($n = 1$ for both displacement and pore pressure variables), respectively. As observed in these figures, in the case of the conventional PNM, the wave pattern (at a particular time) is noisy and asymmetric owing to numerical dispersions emerging from the regular polynomial interpolations used in conventional FEM. To be more clear, the interaction of the wave pulse and the impervious crack (when the wave front hits the crack surface) results in very abrupt and sharp spacial variation in the pore pressure distribution in the vicinity of the fracture. These sharp variations cannot be captured and modeled accurately using conventional interpolations, resulting in very severe numerical dispersion as seen in Figure 3.26a. Furthermore, the small amount of asymmetry introduced into the problem, by slightly inclining the fracture, leads to very asymmetric solution. Unlike the regular PNM, as seen in Figure 3.26b, using the developed PNM-GFEM-M leads to much more accurate and tangible results for the pore pressure contour of the interaction between the wave pulse and the crack. In addition, the PNM-GFEM-M solution is nearly symmetric, as would be expected for a nearly symmetric problem.

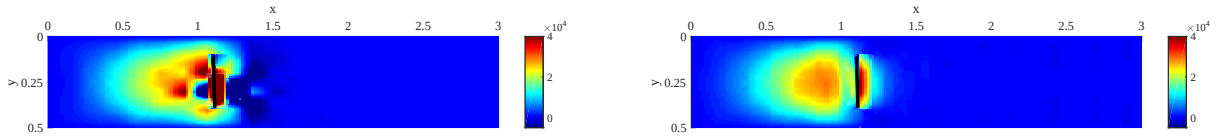

(a) using the conventional PNM (b) using the PNM-GFEM-M model with ($n = 1$)

Fig. 3.26: Pore pressure signal in fractured porous media under impact loading at $t = 0.0092s$.

3.6 Chapter Conclusions

A two-variable ($u - p$) mixed Finite Element Model (FEM) has been developed for dynamic and wave propagation analysis of continuous and fractured porous media. General idea of the Phantom Node Method (PNM) is employed to introduce strong discontinuity of displacement and pore pressure across the crack faces. Trigonometric enrichments are included in the context of the Generalized Finite Element Method (GFEM) to rectify the problem of numerical dispersion that can appear in transient wave propagation simulation of porous media. This way, a new GFEM-enriched PNM mixed finite element model (i.e., PNM-GFEM-M) is developed for coupled dynamic hydro-mechanical simulation of saturated porous media. To satisfy the no-interpenetration condition along the crack faces and to simulate the frictional contact in stick/slip regimes, an Augmented Lagrange Multiplier Method is implemented.

Through various numerical examples, the effectiveness of the developed enriched FE model over conventional approaches is demonstrated. It has been demonstrated that the high-frequency numerical dispersions that may appear in regular FEM/PNM wave results (that are attributed to the Gibbs phenomenon) can be successfully suppressed in the hydro-mechanical wave propagation solutions of porous media using the enriched mixed FE model of this work. Moreover, it was shown that the most accurate wave results with the least amount of spurious oscillations are achieved when both the displacement and pore pressure fields are enriched with trigonometric interpolations; the larger the cutoff number for enrichments, the better the spurious oscillations are inhibited.

Lastly, some interesting hydro-mechanical features of the dynamic response of porous media are documented. When fluid is rapidly injected into a porous media, a non-monotonic response, characterized by a peak-pressure point in the injection pressure time history, is observed. This is in contrast to the monotonically-increasing trend of the injection pressure time history observed when fluid is injected slowly.

The developed Mixed GFEM-enriched Phantom Node Method (PNM-GFEM-M) is a promising model for the simulation of hydro-mechanical wave phenomena and transient dynamic behaviour in both continuous and fractured porous media. It is worth mentioning that the proposed computational approach can be extended to moving cracks in applications like 3D hydraulic fracturing by adding suitable crack propagation criterion and evolving the discontinuities by replacing the regular element with superimposed elements with additional phantom nodes at the locations where failure occurs and fracture advances.

The present article does not concentrate on the computational efficiency of the method for large-scale problems. Given the significant spurious oscillations which appear in the regular FE simulations (even with highly-refined meshes) of high-frequency waves or time-harmonic waves with small wavelengths and the notable capability of the presented enriched FE method to more accurately simulate the wave problems, a future investigation should address the cost-effectiveness of the enriched scheme for large-scale problems.

Chapter 4

Induced acoustic emission simulation in fractured porous media

This chapter is based on the following journal article:

Komijani M., Gracie R., Sarvaramini E., Simulation of Induced Acoustic Emission in Fractured Porous Media, *Engineering Fracture Mechanics*, DOI: 10.1016/j.engfracmech.2018.07.028, 2018 [37]

In this journal paper I was the first author and was responsible for the writing of the article. The paper was edited by Dr. Gracie and Dr. Sarvaramini. I also developed the mathematical and computational formulation and the numerical code.

This chapter addresses objective 3 of the thesis.

4.1 Introduction

Acoustic/microseismic emissions (AE) in naturally fractured porous media are the result of local instability along internal interfaces and the sudden release of strain energy stored in the rock matrix. This rapid release of energy, stimulates high-frequency components of the dynamic response of the rock mass, inducing mechanical wave propagation. In this article an enriched finite element model is employed to concurrently simulate the interface instability and the induced wave propagation processes in a fractured porous media. Harmonic enrichment functions are used in the context of the Generalized Finite Element Method (GFEM) to provide more spurious oscillation-free results for wave propagation/dynamic response. To model the fractures, the Phantom Node Method (PNM) is employed with the GFEM. The frictional contact condition at material interfaces is modeled using a stable augmented Lagrange multiplier approach. Through various parametric studies it is shown that i) decreasing the permeability leads to an increase in the frequency and a decrease in the amplitude of the acoustic signal; ii) increasing viscous damping leads to narrower frequency spectrum and decreased magnitude of the emitted acoustic signal; iii) increasing damping leads to a transition from transient wave propagation to diffusion dominated response; iv) increasing interface friction leads to more pronounced stick-slip behavior and higher amplitude AE-without interface friction there is no AE. Lastly, the numerical illustrations demonstrate the superior capability of the enriched model over regular finite element models in providing non-physical spurious high-frequency oscillation-free, AE solutions.

The process of elastic wave propagation induced by an abrupt local release of stored strain energy is known as an Acoustic Emission (AE) [63]. Acoustic emissions are generated by bifurcation-instabilities such as fault reactivation, pore collapse, and fracture, i.e., localization phenomena. As a result, AE monitoring and analysis are often used to probe the behaviour of solid materials in engineering applications such as, concrete structures [64, 65] and masonry bridges [66], and also geological formations, particularly in mining and hydraulic fracturing applications [126, 127]. For example, during hydraulic fracturing, microseismic monitoring is

often conducted to determine the extent and orientation of the fracture network created [129]. A series of experimental and numerical investigations have been conducted by Carpinteri and his coworkers on analysis of damage and fracturing behaviour in solids and the associated induced acoustic emissions (see for instance, [130, 131, 132, 133]). Analysis of acoustic emissions induced by localization involves many uncertainties and researchers have not yet focused on both explicitly modeling the fracturing/damage process and the simulation of associated induced acoustic wave propagation (specially in shear failure type). In this article, a specially designed enriched mixed-finite element model is employed to study both fracture reactivation due to hydraulic perturbations in a porous media and the resulting AEs. Using this model, the key system characteristics (e.g., friction, permeability, etc.) governing the nature of the emitted AEs are elucidated.

Recent attempts to correlate fracturing/slip and microseismic emission do not explicitly simulate transient acoustic wave propagation through the media following the release of elastic energy, e.g., Tang et al. [134, 135] used a quasi-static approach to relate the energy released by damage to the magnitude of acoustic events. Such approaches do not account for the propagation and interactions of emitted waves with discontinuities, attenuation, nor other wave reflection and coalescence phenomena.

Another class of acoustic emission simulation methods make use of the particle-based Discrete Element Method (DEM), in which the rock mass is represented as a collection of particles/blocks connected together by contact/cohesive forces. Localization and nucleation of fractures is modeled by breakage of the cohesive bonds between particles. Based on this methodology, Hazzard and Young [72] proposed a technique for the simulation of acoustic emission under nucleation (i.e., bond breakage) in rock. The radiated acoustic energy from the source was estimated by measuring the change in kinetic energy upon failure of the bond; however, wave emission and propagation were not directly simulated. In a similar fashion, Lisjak et al. [71] investigated acoustic emissions using DEM with non-porous deformable blocks, where AEs

were related to an energy release through cohesive tension (not shear) tractions between blocks; while an explicitly time integrated dynamic model was used, the accuracy of the wave forms and wave propagation was not the focus of the study. It is important to note that most microseismicity induced in applications like hydraulic fracturing is due to shear failure and sliding along pre-existing discontinuities [68]. Other versions of DEM have also been proposed for studying acoustic emission signals induced by damage, e.g., Carpinteri and his coworkers [69, 70] employed three-dimensional lattice models based on truss-like Discrete Element Method to study AEs in a prismatic concrete specimen subjected to compressional loads. They demonstrated good correlations between numerical results and AE data obtained from experimental tests.

There is a limited number of semi-analytical elastodynamics solution of AEs induced by sudden fracture nucleation, for example the models of Andreykiv et al. [136, 137, 138] for the AE due to the nucleation of penny-shaped fractures under modes I and III. None of the available analytical or semi-analytical solutions specifically address AE due to failure in shear (mode II) (i.e., microseismicity) under compression, where contact forces and frictional behaviour influence the AEs. Furthermore, there is a lack of solutions for AE in porous media due to reactivation of fracture or fracture nucleation.

Analysis of porous media spans applications from the geomechanics of reservoirs [102] to biomechanical analysis of tissues and cells [106, 141]. It is common in such models to assume that the fluid flow is transient but the solid evolves quasi-statically. There has been less emphasis on dynamic simulation of fracture in porous media; the focus to date has been on the modeling of fracture propagation rather than the simulation of the waves emitted from the cracks. For example, recently Cao et al. [142] simulated the stepwise process of fracturing in porous media and the associated fluid pressure oscillations using the standard FEM and Réthoré et al. [118] modeled the dynamic propagation of shear bands in saturated porous media. However, these earlier works did not address the topic of simulation of wave propagation nor acoustic emission.

Accurate simulation of wave propagation using standard finite element approaches is problematic, as the polynomial basis functions used have been shown to be insufficient in some dynamic simulations [74]. Conventional finite element solutions of wave phenomena are well-known to contain spurious wave forms, which often cannot be efficiently eliminated using mesh refinement in transient and time-harmonic waves with short wave lengths [79]. Furthermore, numerical dispersions can significantly affect wave propagation velocity. Enriched Generalized Finite Element Methods (GFEM) have been developed to inhibit the spurious oscillations [78, 79]. Recently, Komijani and Gracie [32] extended these models to wave propagation in fractured media by combining the GFEM approach with the initial discretization-independent fracture/discontinuity modeling ability of the Phantom Node Method (PNM) of [29]. The enriched model (PNM-GFEM) combines the benefits of the two methods and minimizes the non-physical oscillations observed in regular dynamics simulations of fractures.

It is noted that in addition to the weak form-based finite element methods, a new class of numerical methods, i.e., Extended Particle Difference Method (EPDM) [33, 34, 35], has been developed recently to model strong/weak discontinuities independently of the initial discretization, which may be used as an alternative for the finite element methods. The EPDM is a strong form-based numerical solution of the governing equations with the particle derivative approximation. In addition to the increase of computational efficiency that is achieved by avoiding numerical integration of the weak form, one of the notable features of the EPDM is that, unlike the weak form-based methods, there is no need for employing an additional boundary tracking scheme such as the level set method, which makes the method very suitable for moving boundary problems.

This article presents the application of an extension of the PNM-GFEM method to acoustic wave emission simulation in fractured porous media. The media is modeled using mixture theory of poroelasticity [107, 108]. The solution of the governing system of equations is ap-

proximated using a mixed enriched finite element method (PNM-GFEM-M). The frictional contact at the interface of the fractures is simulated using an augmented Lagrange multiplier technique. Fracture instability is initiated via a perturbation source like fluid injection near the discontinuity, causing a stick to slip transition and leading to a sudden release of energy. Acoustic emissions, triggered through a sudden release of strain energy at the discontinuity interface due to shear failure, are simulated. It is shown that the PNM-GFEM-M results in more spurious-oscillation-free AEs compared to standard finite element approaches because it suppresses numerical dispersions of acoustic signals in both velocity and pore pressure fields. Using this simulation tool, the role of permeability, viscous damping, and contact friction on AEs is more clearly illustrated.

4.2 Mathematical Formulation

The differential equations governing the interaction of solid and fluid phases in porous media are obtained from Biot's mixture theory based on the concept of volume fractions for each phase.

4.2.1 Governing Equations

A two-dimensional poroelastic medium, Ω in Cartesian coordinate O_{xy} is considered. Let $\boldsymbol{u}(x, y, t)$ denote the displacement vector of the total mixture. For the sake of completeness, the well-established formulation of mixture theory of poroelasticity is given below.

The linear strain-displacement relation in infinitesimal deformation is

$$\boldsymbol{\varepsilon} = \frac{1}{2}(\nabla \boldsymbol{u} + (\nabla \boldsymbol{u})^T) \tag{4.1}$$

The constitutive equation for the solid matrix is given by:

$$\boldsymbol{\sigma'} = \boldsymbol{C} : \boldsymbol{\varepsilon} \tag{4.2}$$

in which $\boldsymbol{\sigma'}$ is the effective stress tensor acting on the solid skeleton, and $\boldsymbol{C}$ is the elastic stiffness tensor.

The relative motion of the fluid phase with respect to the total mixture is denoted by $w_i(x, t)$. To arrive at a two-field model, it is assumed that the relative acceleration of the fluid phase with respect to the total mixture is negligible, i.e., $\ddot{w}_i = 0$. It is noted that this assumption has been shown to be valid and more appropriate for loading conditions up to earthquake frequencies for modeling the saturated porous material [114, 43]. The momentum balance of the total mixture is:

$$\nabla \cdot \boldsymbol{\sigma} - \rho \ddot{\boldsymbol{u}} + \rho \boldsymbol{b} = 0 \tag{4.3}$$

in which $\ddot{\boldsymbol{u}}$ denotes the acceleration of the mixture, $\boldsymbol{\sigma}$ is the total stress, ρ is the average mixture density, and b is the body force acting on the mixture.

The average density of the mixture is defined as a weighted summation of solid and fluid phases densities

$$\rho = n' \rho_f + (1 - n') \rho_s \tag{4.4}$$

in which ρ_f and ρ_s are the density of fluid phase and solid skeleton, respectively, and n' is the porosity of the media.

The total stress of the mixture is defined as a combination of the stress acting on the solid phase and the pore pressure:

$$\boldsymbol{\sigma} = \boldsymbol{\sigma'} - \alpha_p p \boldsymbol{I} \tag{4.5}$$

where p is the fluid pore pressure, $\boldsymbol{I}$ is the identity tensor, $\boldsymbol{\sigma'}$ denotes the effective stress acting on the solid skeleton, and α_p is Biot's coefficient.

Neglecting the relative acceleration of the pore fluid with respect to the mixture, the generalized Darcy relation can be obtained from conservation of momentum of the fluid phase:

$$-\nabla p - \boldsymbol{R} - \rho_f \ddot{\boldsymbol{u}} + \rho_f \boldsymbol{b} = 0 \tag{4.6}$$

in which $\boldsymbol{R}$ is the averaged viscous drag force acting on the fluid defined by the Darcy seepage law:

$$\dot{\boldsymbol{w}} = \boldsymbol{k}_f \boldsymbol{R} \tag{4.7}$$

where $\boldsymbol{k}_f$ is the permeability tensor of the porous media.

The Eulerian continuity equation of the fluid phase can be written as:

$$\nabla \cdot \dot{\boldsymbol{w}} + \alpha \nabla \cdot \dot{\boldsymbol{u}} + \frac{\dot{p}}{Q} = 0 \tag{4.8}$$

in which $1/Q = (\alpha - n')/K_s + n'/K_f$, and K_s and K_f are the bulk moduli of solid and fluid phases, respectively.

The relative velocity of the fluid phase with respect to the mixture (i.e., $\boldsymbol{w}$) may be eliminated from (4.8) using (4.6) and (4.7) resulting in

$$\nabla \cdot k_f[-\nabla p - \rho_f \ddot{\boldsymbol{u}} + \rho_f \boldsymbol{b}] + \alpha \nabla \cdot \dot{\boldsymbol{u}} + \frac{\dot{p}}{Q} = 0 \tag{4.9}$$

Equations (4.3) and (4.9) are the governing differential equations of the problem for the unknown displacement and pore pressure fields[114].

4.2.2 Weak Formulation of the Governing Differential Equations

Consider a porous media Ω with boundary Γ. Boundary Γ comprises of Γ_u, Γ_t, Γ_p, and Γ_w, which represent the boundary surfaces for prescribed displacement, traction, pore pressure, and out-flow flux of fluid, respectively. Domain Ω contains internal interfaces denoted by Γ_d.

A weak formulation of the coupled system of equations (4.3) and (4.9) may be developed using appropriate test functions, $\delta\boldsymbol{u}$ and δp. The problem to be solved is to find $\mathbf{u}(x, y, t) \in U$ and $p(x, y, t) \in W$ such that

$$\int_\Omega \boldsymbol{\sigma} : \delta\boldsymbol{\varepsilon}\, d\Omega + \int_\Omega \rho \ddot{\boldsymbol{u}} \cdot \delta\boldsymbol{u}\, d\Omega - \int_{\Gamma_t} \bar{\boldsymbol{t}} \cdot \delta\boldsymbol{u}\, d\Gamma - \int_\Omega \rho \boldsymbol{b} \cdot \delta\boldsymbol{u}\, d\Omega + \int_{\Gamma_d} \bar{\boldsymbol{t_d}} \cdot \delta[[\boldsymbol{u}]]\, d\Gamma = 0, \forall \delta\boldsymbol{u} \in U_0 \tag{4.10}$$

$$\int_\Omega \nabla\delta p \cdot k_f \nabla p \; d\Omega + \int_\Omega \nabla\delta p k_f \cdot \rho_f \ddot{\boldsymbol{u}} \; d\Omega + \int_\Omega \delta p \; \alpha_p \; \nabla \cdot \dot{\boldsymbol{u}} \; d\Omega + \int_\Omega \delta p \; 1/Q \; \dot{p} \; d\Omega -$$

$$\int_\Omega \nabla\delta p k_f \cdot \rho_f \boldsymbol{b} \; d\Omega + \int_{\Gamma_w} \delta p (\dot{\boldsymbol{w}} \cdot \boldsymbol{n}_\Gamma) \; d\Gamma - \int_{\Gamma_d} \delta p [[\dot{\boldsymbol{w}}]] \cdot \boldsymbol{n}_{\Gamma_d} \; d\Gamma = 0, \forall \delta p \in W_0 \tag{4.11}$$

in which U,W, U_0, and W_0 are appropriate function spaces. The jump in the displacement field across the discontinuity surface is denoted by $[[\boldsymbol{u}]]$, and $[[\dot{\boldsymbol{w}}]]$ is the discontinuity of fluid flux into the crack interface from either crack face. $\bar{\boldsymbol{t_d}}$ denotes the internal applied traction (e.g., contact force) on the internal discontinuity Γ_d.

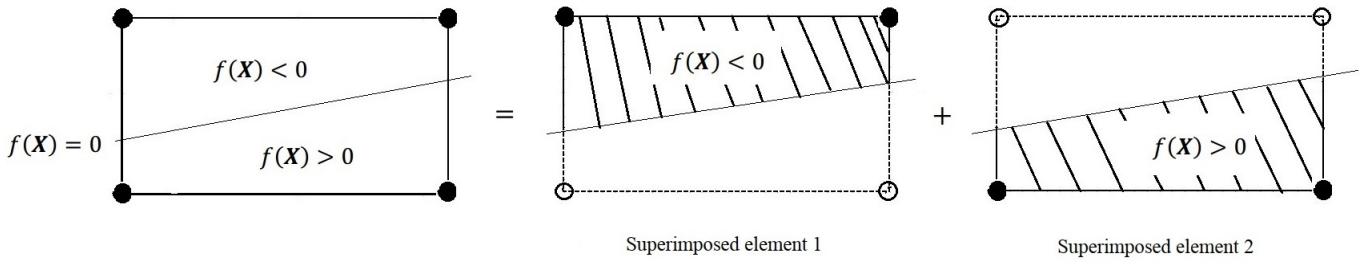

Fig. 4.1: Decomposition of a cracked element into two superimposed paired elements with original real and additional phantom nodes in the PNM. Original real nodes and additional phantom nodes are shown by solid and hollow circles, respectively.

4.3 Finite Element Formulation

4.3.1 Mixed GFEM-enriched Phantom Node Method (PNM-GFEM-M)

To model a discontinuity in the displacement and pore pressure fields within a fractured element, the Phantom Node Method (PNM) [29] is employed to achieve a discontinuous interpolation of the fields. This is accomplished using two superimposed paired elements with original real and additional fictitious/phantom nodes. In this framework, to model discontinuity, any element cut by a crack is replaced by two superimposed continuous elements with real and additional phantom nodes as shown schematically in Figure 4.1. Also, based on the general idea of PNM-GFEM method [32], trigonometric enrichment basis functions [79] are used to enrich the approximation functions to suppress the non-physical numerical dispersions that can appear in dynamic response of regular FEM solutions.

Displacement field discretization

For a cracked element in a porous media, the PNM-GFEM [32] interpolation is employed to approximate the displacement in the x and y directions, i.e.,

$$u_x(x,y,t) = H(-f(x,y)) \sum_{I \in S_1} \left(\boldsymbol{\psi}_I^1(x,y) \boldsymbol{u}_{Ix}(t) \right) + H(f(x,y)) \sum_{I \in S_2} \left(\boldsymbol{\psi}_I^1(x,y) \boldsymbol{u}_{Ix}(t) \right) \qquad (4.12)$$

$$u_y(x,y,t) = H(-f(x,y)) \sum_{I \in S_1} \left(\boldsymbol{\psi}_I^2(x,y) \boldsymbol{u}_{Iy}(t) \right) + H(f(x,y)) \sum_{I \in S_2} \left(\boldsymbol{\psi}_I^2(x,y) \boldsymbol{u}_{Iy}(t) \right) \quad (4.13)$$

in which $H(\cdot)$ is the step function and S_1 and S_2 are the sets of nodes corresponding to each of the two superimposed elements. Each of the two superimposed elements contains original real nodes and additional phantom nodes. The location of the discontinuity inside an element is defined by a level set function such that $f(x,y) = 0$ specifies the discontinuous surface. $\boldsymbol{\psi}_I^1$ and $\boldsymbol{\psi}_I^2$ are the arrays of conventional and enriched basis functions of node I for the displacement components in x and y directions, respectively. Vectors of corresponding conventional and enriched displacement degrees of freedom for node I in the x and y directions are respectively denoted by $\mathbf{u}_{Ix}$ and $\mathbf{u}_{Iy}$, as shown below.

$$\boldsymbol{\psi}_I^{1,2} = \left[\begin{array}{cccc} \psi_{I(0,0)} & \psi_{I(1,0)}^{C_x} & ... & \psi_{I(n,m)}^{S-} \end{array} \right] \quad (4.14)$$

$$\boldsymbol{u}_{Ix}^{\top} = [u_{Ix(0,0)}, u_{Ix(1,0)}^{C_x}, ..., u_{Ix(n,m)}^{S-}] \quad (4.15)$$

$$\boldsymbol{u}_{Iy}^{\top} = [u_{Iy(0,0)}, u_{Iy(1,0)}^{C_x}, ..., u_{Iy(n,m)}^{S-}] \quad (4.16)$$

In the above formulation $\psi_{I(0,0)} = N_I$ denote regular Lagrangian interpolation functions and $\psi_{I(k_x,k_y)}^{\gamma} = N_I \phi_{(k_x,k_y)}^{\gamma}$ are the GFEM interpolation functions in which $\phi_{(k_x,k_y)}^{\gamma}$ with the corresponding superscript denotes the following trigonometric basis functions:

$$\phi_{(k_x,0)}^{C_x} = cos(\frac{2\pi k_x x}{\Lambda_x}), \quad \phi_{(k_x,0)}^{S_x} = sin(\frac{2\pi k_x x}{\Lambda_x}),$$

$$\phi_{(0,k_y)}^{C_y} = cos(\frac{2\pi k_y y}{\Lambda_y}), \quad \phi_{(0,k_y)}^{S_y} = sin(\frac{2\pi k_y y}{\Lambda_y})$$

$$\phi_{(k_x,k_y)}^{C+} = cos(\frac{2\pi k_x x}{\Lambda_x} + \frac{2\pi k_y y}{\Lambda_y}), \quad \phi_{(k_x,k_y)}^{S+} = sin(\frac{2\pi k_x x}{\Lambda_x} + \frac{2\pi k_y y}{\Lambda_y})$$

$$\phi^{C-}_{(k_x,k_y)} = cos(\frac{2\pi k_x x}{\Lambda_x} - \frac{2\pi k_y y}{\Lambda_y}), \quad \phi^{S-}_{(k_x,k_y)} = sin(\frac{2\pi k_x x}{\Lambda_x} - \frac{2\pi k_y y}{\Lambda_y})$$

Pore pressure field discretization

Following the general idea of the PNM-GFEM, in the case of impervious crack faces (i.e., discontinuous pore pressure field), the pore pressure approximation in fractured elements is

$$p(x,y,t) = H(-f(x,y)) \sum_{I \in S_1} \left(\boldsymbol{\psi}^3_I(x,y) \boldsymbol{p}_I(t) \right) + H(f(x,y)) \sum_{I \in S_2} \left(\boldsymbol{\psi}^3_I(x,y) \boldsymbol{p}_I(t) \right) \tag{4.17}$$

in which $\boldsymbol{\psi}^3_I$ denotes the set of conventional and enriched interpolation functions for the pore pressure variable, and $\boldsymbol{p}_I$ is the vector of corresponding regular and enriched, phantom or real pore pressure degrees of freedom for node I.

$$\boldsymbol{\psi}^3_I = \left[\begin{array}{cccc} \psi_{I(0,0)} & \psi^{C_x}_{I(1,0)} & ... & \psi^{S-}_{I(n,m)} \end{array} \right] \tag{4.18}$$

4.3.2 Discretized mixed finite element equations

Semi-discretized system of equations can be developed by substitution of the specified displacement interpolation functions (4.12)-(4.13) and pore pressure field (4.17) in the weak form (4.10)-(4.11):

$$\sum_{J=1}^{n_{node}} \left([M^e]^{11}_{IJ} \ddot{\mathbf{u}}^e_{Jx} + [K^e]^{11}_{IJ} \mathbf{u}^e_{Jx} + [K^e]^{12}_{IJ} \mathbf{u}^e_{Jy} + [K^e]^{13}_{IJ} \mathbf{p}^e_J \right) = \mathbf{F}^e_{Iu_x}, \quad (I = 1, ..., n_{node}) \tag{4.19}$$

$$\sum_{J=1}^{n_{node}} \left([M^e]^{22}_{IJ} \ddot{\mathbf{u}}^e_{Jy} + [K^e]^{21}_{IJ} \mathbf{u}^e_{Jx} + [K^e]^{22}_{IJ} \mathbf{u}^e_{Jy} + [K^e]^{23}_{IJ} \mathbf{p}^e_J \right) = \mathbf{F}^e_{Iu_y}, \quad (I = 1, ..., n_{node}) \tag{4.20}$$

$$\sum_{J=1}^{n_{node}} \Big([M^e]^{31}_{IJ} \ddot{\mathbf{u}}^e_{Jx} + [M^e]^{32}_{IJ} \ddot{\mathbf{u}}^e_{Jy} + [C^e]^{31}_{IJ} \dot{\mathbf{u}}^e_{Jx} + [C^e]^{32}_{IJ} \dot{\mathbf{u}}^e_{Jy} +$$

$$[C^e]^{33}_{IJ}\dot{\mathbf{p}}^e_J + [K^e]^{33}_{IJ}\mathbf{p}^e_J\Big) = \mathbf{F}^e_{Ip}, \quad (I = 1, ..., n_{node}) \tag{4.21}$$

in which n_{node} is the number of nodes in each of the two superposed elements 1 and 2, and includes both original real and fictitious/phantom nodes. In an element crossed by a crack, the definitions of $[M^e]_{IJ}$, $[C^e]_{IJ}$, $[K^e]_{IJ}$, $\mathbf{F}^e_{Iu_x}$, $\mathbf{F}^e_{Iu_y}$, and $\mathbf{F}^e_{Ip}$ in (4.19), (4.20), and (4.21) for each of the superimposed elements, i.e., e= 1 or 2, are given in the Appendix.

The semi-discretized coupled hydro-mechanical poro-elastic finite element equations (4.19), (4.20), and (4.21) can be rewritten in a more compact form as:

$$[M]\left\{\ddot{\mathbf{\Delta}}\right\} + [C]\left\{\dot{\mathbf{\Delta}}\right\} + [K]\{\mathbf{\Delta}\} = \{\mathbf{F}\} \tag{4.22}$$

where $\{\mathbf{\Delta}\} = \{\mathbf{u}_x \;\; \mathbf{u}_y \;\; \mathbf{p}\}^\top$ is the vector of unknown nodal values for displacement and pore pressure degrees of freedom in the porous media, and $\{\mathbf{F}\} = \left\{\mathbf{F}_{u_x} \;\; \mathbf{F}_{u_y} \;\; \mathbf{F}_p\right\}^\top$ is the vector of mechanical forces and flow fluxes.

The G22 and G11 generalized Newmark implicit schemes are employed for time integration of displacement and pore pressure degrees of freedom, respectively. To this end, the values of the first- and second-order time derivatives of the variables at time step $(i+1)$ are represented in terms of the corresponding values of the variables at the current time step (i) and unknown values of the variables at time step $(i+1)$ through the following relationships:

$$\ddot{u}_{i+1} = \frac{1}{\beta\Delta t^2}(u_{i+1} - u_i) - \frac{1}{\beta\Delta t}\dot{u}_i - (\frac{1}{2\beta} - 1)\ddot{u}_i \tag{4.23}$$

$$\dot{u}_{i+1} = \frac{\gamma}{\beta\Delta t}(u_{i+1} - u_i) - (\frac{\gamma}{\beta} - 1)\dot{u}_i - \Delta t(\frac{\gamma}{2\beta} - 1)\ddot{u}_i \tag{4.24}$$

$$\dot{p}_{i+1} = \frac{1}{\theta\Delta t}(p_{i+1} - p_i) - (\frac{1}{\theta} - 1)\dot{p}_i \tag{4.25}$$

where γ, β, and θ are the integration parameters that are set to be 0.7 in the numerical examples of the present work. The integration constants are usually chosen in the range of [0 1]. To preserve the unconditional stability condition of the time integration θ and γ need to be greater than or equal to 0.5 and β should be greater than or equal to $0.25(0.5+\gamma)^2$ [43]. However, it is clear that because of the highly-transient feature of wave propagation, sufficiently small time steps need to be considered in dynamic simulations to obtain converged results.

4.4 Interface simulation

Geomechanical formations experience huge amounts of overburden and horizontal in-situ stresses leading to significant normal and frictional contact forces acting along natural and induced fractures and faults. In the context of the partition-of-unity finite element a noticeable amount of research has been dedicated to the imposition of inter-facial constraints [123, 124, 125]. In this work, a stable augmented Lagrange multiplier approach is adopted to enforce the frictional contact via an iterative method.

Accounting for the contact force contributions, the weak form (4.10) is transformed as:

$$\int_{\Omega} \boldsymbol{\sigma} : \delta\boldsymbol{\varepsilon}\ d\Omega + \int_{\Omega} \rho\ddot{\boldsymbol{u}} \cdot \delta\boldsymbol{u}\ d\Omega - \int_{\Gamma_t} \bar{\boldsymbol{t}} \cdot \delta\boldsymbol{u}\ d\Gamma - \int_{\Omega} \rho\boldsymbol{b} \cdot \delta\boldsymbol{u}\ d\Omega - \int_{\Gamma_d} \bar{\lambda}_N \delta g_N d\Gamma - \int_{\Gamma_d} \bar{\lambda}_T \delta g_T d\Gamma = 0 \tag{4.26}$$

Normal contact traction, normal inter-penetration, tangential contact frictional traction, and tangential slip across the interface are denoted by $\bar{\lambda}_N$, g_N, $\bar{\lambda}_T$, and g_T , respectively.

One-dimensional elements are used along the interface to interpolate the contact force/Lagrange multiplier fields:

$$\bar{\lambda}_N = \tilde{\mathbf{N}}\bar{\boldsymbol{\lambda}}_N \text{ and } \bar{\lambda}_T = \tilde{\mathbf{N}}\bar{\boldsymbol{\lambda}}_T \tag{4.27}$$

Here, $\tilde{\mathbf{N}}$ denotes linear one-dimensional Lagrangian shape functions, and $\left(\bar{\boldsymbol{\lambda}}_N, \bar{\boldsymbol{\lambda}}_T\right)$ are the vectors of Lagrange multiplier degrees of freedom for normal and friction contact forces. To ensure the stability of the interface contact solution, the nodes of the Lagrange multiplier mesh are chosen using the Vital Vertex Method [124, 125].

At each time step, $\boldsymbol{\Delta}_{n+1}$ and $\left(\bar{\boldsymbol{\lambda}}_N, \bar{\boldsymbol{\lambda}}_T\right)_{n+1}$ are sought using an iterative procedure. The iterative process starts ($k = 0$) with an initial guess for the vector of Lagrange multipliers

$\left(\bar{\boldsymbol{\lambda}}_N, \bar{\boldsymbol{\lambda}}_T\right)_{n+1}^{k=0} = \left(\bar{\boldsymbol{\lambda}}_N, \bar{\boldsymbol{\lambda}}_T\right)_n$. Given $\left(\bar{\boldsymbol{\lambda}}_N, \bar{\boldsymbol{\lambda}}_T\right)_{n+1}^{k}$ at iteration k, the linear fully-discretized system of equations is solved for $\boldsymbol{\Delta}_{n+1}^{k}$, from which the normal interpenetration g_N^k and tangential slip g_T^k of the crack at each node of the Lagrange multiplier mesh are calculated. The Lagrange multiplier nodal vectors are updated if the gap norms surpass a defined tolerance. In the case of frictional contact, interface slippage occurs, $g_T > 0$, if the tangential frictional contact force, $\bar{\lambda}_T$, required to prevent slip exceeds the limit $\bar{\lambda}_T^{max} = \bar{\lambda}_N \mu_f$ (μ_f is the friction coefficient). Otherwise the interface is in the stick state.

Table 4.1: Material properties of the porous media.

$E(Pa)$	ν	$\rho_s(kg/m^3)$	$\rho_f(kg/m^3)$	n'	$k_f(m^3s/kg)$	$K_f(Pa)$	$K_s(Pa)$
14.516×10^6	0.3	2000	1000	0.3	1.0194×10^{-6}	2.1×10^9	1×10^{20}

4.5 Results and discussion

In this section, the simulation of acoustic wave emission due to sudden release of strain energy (in shear mode) at interface location is carried out. The domain of analysis is assumed to be a two-dimensional isotropic-homogeneous poroelastic media with hydro-mechanical properties given in Table 4.1, unless stated otherwise. Based on the magnitudes considered for the bulk moduli of solid skeleton and pore fluid, the material is compressible. However, the material behaviour can get close to incompressibility condition by decreasing the permeability magnitude. It is worth mentioning that the numerical model developed in this paper is a general computational scheme for simulation of acoustic emissions induced by shear slip on material interfaces and can be employed for different types of materials with different inhomogeneity and anisotropy conditions and randomness in material and geometry characteristics (e.g., randomly distributed cracks). A unit thickness is assumed in the out-of-plane direction. It is noted that proportional damping in the form of $\mu_1[M] + \mu_2[K]$ is assumed to describe the physical attenuation of waves in the solid phase of the media, in which μ_1 and μ_2 are the damping coefficients corresponding to the mass and stiffness matrices of the solid phase, respectively. It is important to mention that, to the best of the authors' knowledge there is no analytic nor experimental data in the literature on induced acoustic wave propagation under interface instability (shear failure) with frictional contact condition. Therefore, no comparison could be carried out between the results of this study with other data. However, the general framework of the employed numerical method in this work (i.e., PNM-GFEM) has been well-established in a couple of papers previously published by the first and the second authors of this article; the accuracy and validity of the method in modeling wave propagation problems in fractured media have been verified through several convergence and comparison studies (see [32, 36]).

4.5.1 Acoustic emission simulation due to shear failure of an interface

Simulation of acoustic signal

To have a better intuition about how local release of strain energy can trigger acoustic emission in a medium, a two-dimensional domain of $1m$ by $0.5m$ is considered. A sloping crack of length $0.36m$ orientated at the angle $\theta = 56^0$ with respect to the horizontal direction is embedded in the medium and frictional contact state is considered at the interface. The friction coefficient is assumed to be $\mu_f = 0.6$ along the embedded interface. The domain is discretized using 30×10 rectangular elements. The porous medium is subjected to a bilateral confining stress, imposed by compressive tractions of $\bar{t} = 10kN/m^2$ acting of the left and top edges of the domain.
The geometry of the medium and the fracture, boundary conditions and the imposed loads are shown in figure 4.2. All the edges are assumed to be hydraulically drained. The simulation starts by the release of the friction/tangential contact constraint at the interface to induce an acoustic response through the release of energy stored in the system due to the initial in-situ stresses. Damping coefficients of the solid phase are assumed to be $\mu_1 = 0.01, \mu_2 = 0.01$. The time steps size for the implicit time integration scheme is $\Delta T = 2 \times 10^{-4}s$. To investigate the dynamic response of the system, time histories of the problem variables at point $(x = 0.9667, y = 0.25)$ are recorded. Figure 4.3 shows the x-velocity signal due to the release of friction at the interface using regular PNM and enriched PNM-GFEM. The enriched model gives a more oscillation-free acoustic signal. As seen in Figure 4.3b, the non-physical oscillations that appear in regular PNM simulation of the velocity signal are effectively inhibited using the enriched model (i.e., PNM-GFEM-M model).

The pore pressure time signal of the acoustic emission is shown in figure 4.4 for regular and enriched finite element simulations. It is clear in this figure that using the enriched FE model results in acoustic data which is free of high-frequency oscillations at the signal's peak.

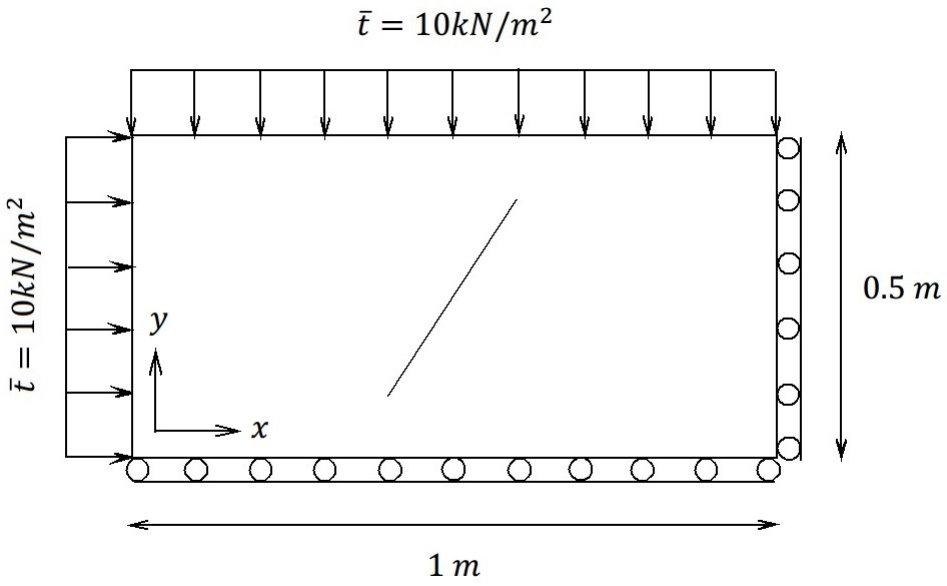

Fig. 4.2: A schematic figure of fractured porous media of section 4.5.1.

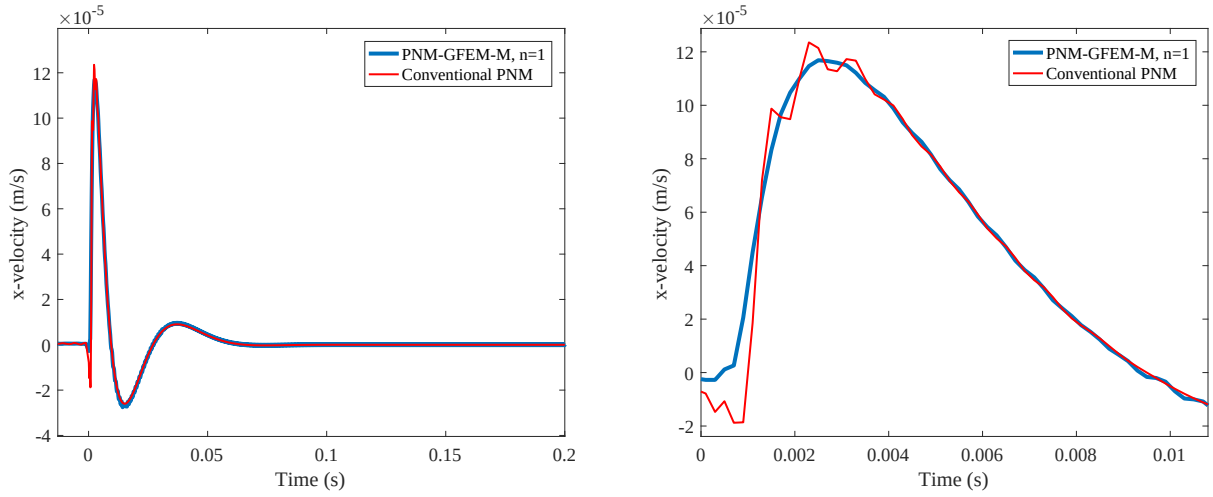

(a) (b)

Fig. 4.3: Time history of x-velocity at point $(x = 0.9667, y = 0.25)$ using regular and enriched PNM models.

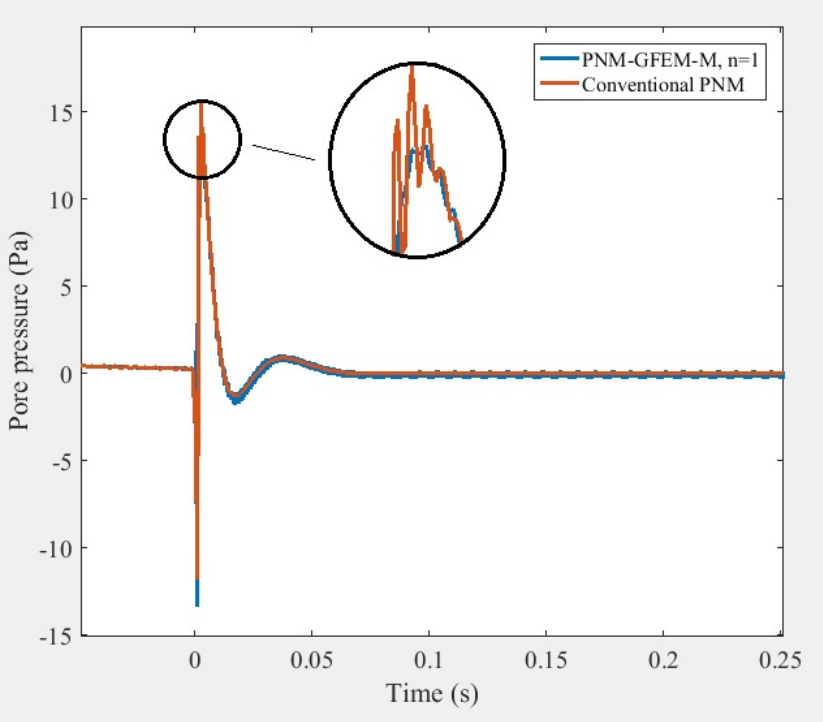

Fig. 4.4: Time history of pore pressure signal at point $(x = 0.9667, y = 0.25)$ using regular and enriched models.

Figure 4.5 illustrates the effect of damping coefficients on the acoustic response of the system. The results are obtained by changing the damping coefficients of the solid phase. Enriched models are used with $(n = 1)$. As seen in this figure, the high-frequency components of the signal are dissipated very quickly by increasing the physical damping of the solid skeleton.

To have a better understanding about the spectral/frequency contents, a Fast Fourier Transform (FFT) is employed to acquire the frequency spectrum of the signal, as shown in figure 4.6. The high-frequency components of the signal are dissipated by increasing the damping coefficients. However, unlike the magnitude spectrum, the peak frequencies of the spectrum (i.e., frequencies associated with peak magnitudes) do not seem to be significantly affected by the damping magnitudes of the solid skeleton.

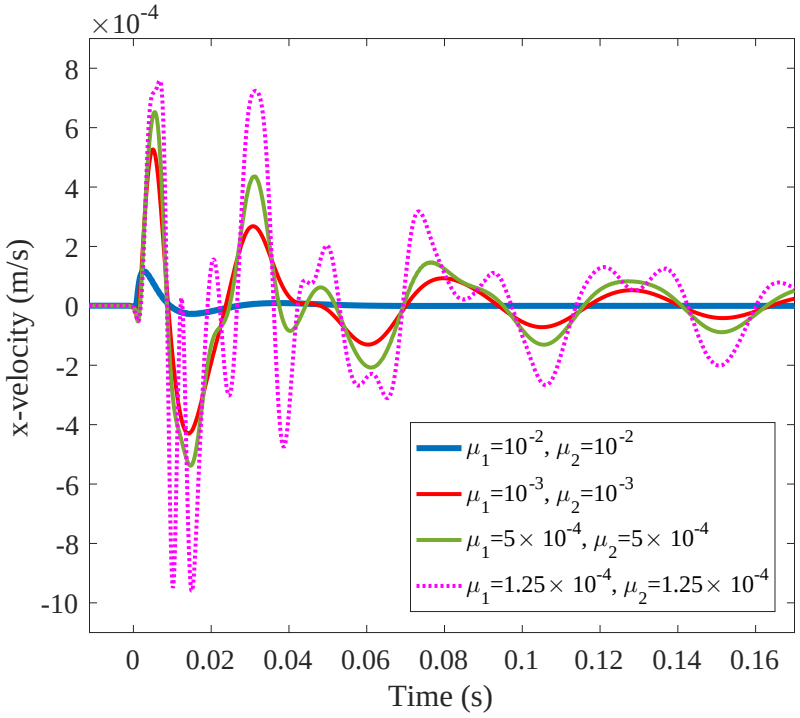

Fig. 4.5: Effect of the damping values on the time history of acoustic signal at point ($x = 0.9667, y = 0.25$).

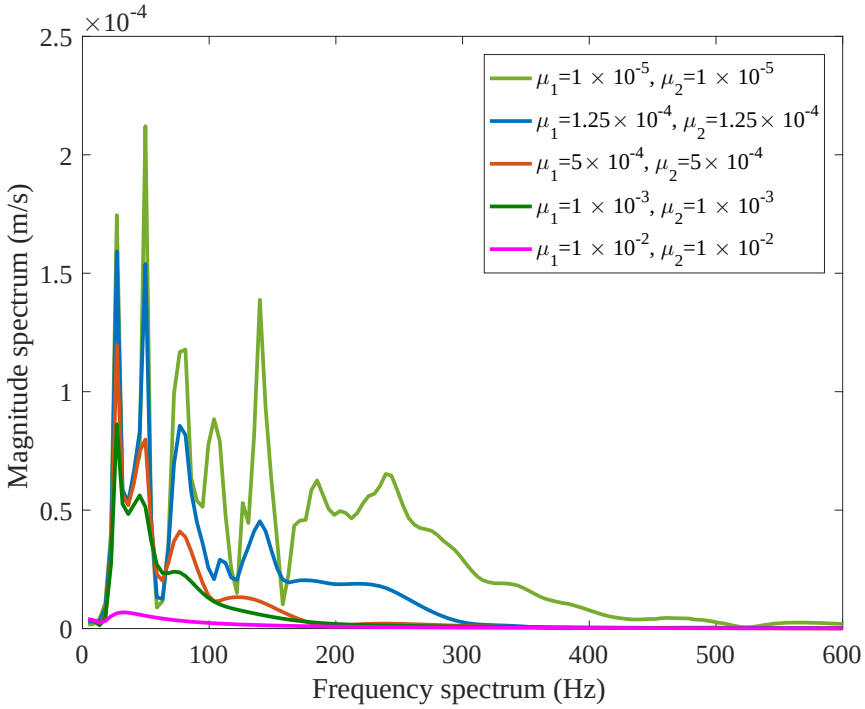

Fig. 4.6: Frequency domain response of the acoustic signal of figure 4.5.

Effect of permeability on the acoustic signal

To assess the effect of the permeability of porous media on acoustic response, the case study shown schematically in Figure 4.2 is considered. Figures 4.7 and 4.8a show, respectively, plots of x-displacement and x-velocity versus time at point $(x = 0.9667, y = 0.25)$ for various values of permeability. As seen in these figures, the lower the permeability the smaller the peak amplitudes of the acoustic signal. This behaviour can be attributed to the inversely proportional correlation between permeability and viscous damping in porous media which results in more energy dissipation in low-permeability materials. Also, as seen in the figures, the dynamic behaviour of lowest permeable domain cases exhibits the highest frequencies in the induced signal. This can be explained by the fact that the behaviour of the lower permeable domain is more undrained. Figure 4.8b gives a close-up of the time history presented in figure 4.8a. By decreasing the amount of permeability (i.e., getting close to material incompressibility condition) the time signal (mixed finite element solutions in general) gets more vulnerable to numerical dispersions and prone to showing spurious oscillations. As observed in figure 4.8b, the non-physical oscillations that are stimulated in regular finite element simulation of the low-permeable case can be eliminated through the enriched finite element model (i.e., PNM-GEFM-M) with $(n = 1)$.

Acoustic wave pattern

To visualize the pattern of an acoustic wave propagation under shear failure, a porous domain of size $3m \times 3m$ is considered. A single fracture is embedded at the center of the domain which is $0.1m$ in length and is orientated at the angle of 45^o with respect to the horizontal direction. The friction coefficient of the interface is assumed to be $\mu_f = 0.6$ and the damping coefficients of the solid phase are $\mu_1 = \mu_2 = 0.001$. Confining tractions of $\bar{t} = 10kN/m^2$ and $\bar{t} = 5kN/m^2$ are imposed at the left and top surfaces, respectively. The domain is discretized using 90×90 rectangular elements. Simulation starts at $t = 0.0s$ by releasing the friction condition at the interface. Figure 4.9 demonstrates consecutive snapshots of x-velocity contours at some time

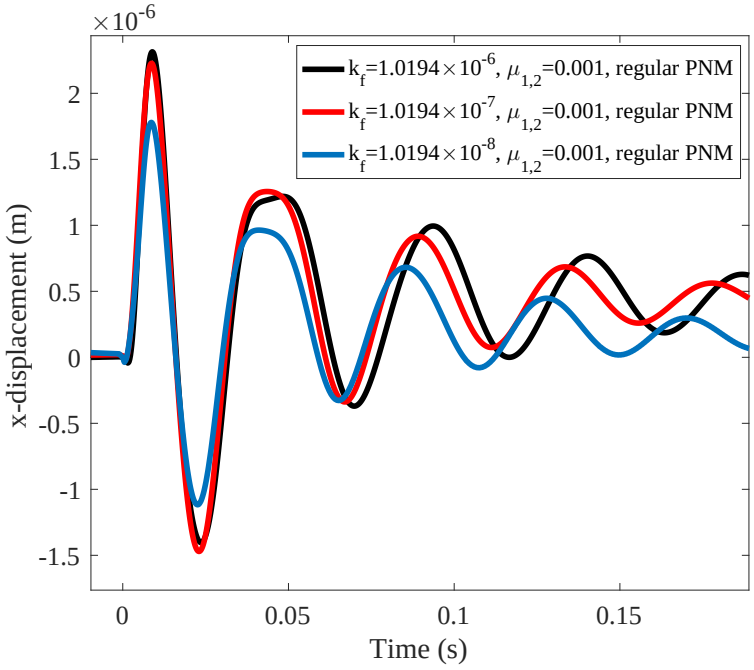

Fig. 4.7: Time history of x-displacement for various values of permeability.

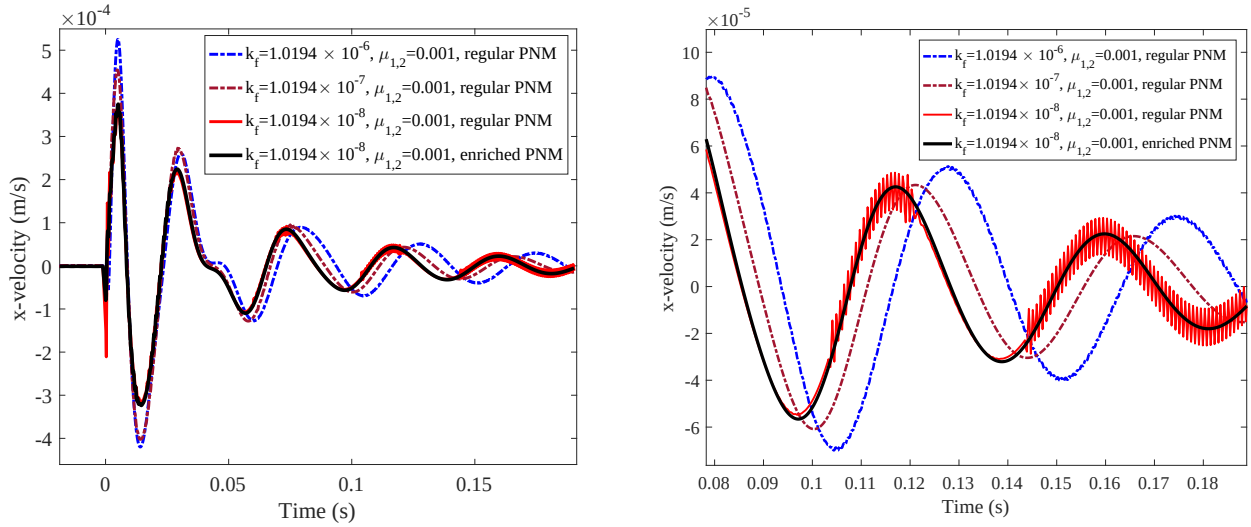

Fig. 4.8: Time history of x-velocity acoustic signal for various values of permeability.

steps. Transient propagation pattern of the acoustic wave emission due to the induced abrupt slip at the interface (which is followed by a sudden release of accumulated-strain-energy) is transparent in the figures.

To have a better visual intuition about the wave propagation pattern, figure 4.10 shows the absolute velocity (i.e., $\sqrt{(\dot{u}_x)^2 + (\dot{u}_y)^2}$) contours of the same problem at several time steps after the acoustic emission is triggered, using a 180×180 mesh resolution. Symmetric pattern of the wave propagation with respect to the shear failure (fracture) direction is apparent in the snapshots. Due to the attenuation of the porous media (in both phases), the velocity magnitude decays as the wave travels in the medium. Figure 4.11 shows the wave pattern at time $t = 0.0047s$ in a three-dimensional perspective from a different (angled) view.

Role of material damping

To investigate the effect of material viscous damping on the microseismic response in porous media, figure 4.12 illustrates acoustic wave propagation pattern in a $6m \times 6m$ domain with a fracture of length $0.2m$ located at the center of the domain and with an orientation of 45^o from the horizontal direction. Confining tractions of $\bar{t} = 10kN/m^2$ and $\bar{t} = 5kN/m^2$ are applied at the left and top surfaces, respectively. In this case, lower damping coefficients ($\mu_1 = \mu_2 = 0.00005$) are considered for the analysis compared to those assumed in the previous example. Comparing the results obtained for $\mu_1 = \mu_2 = 0.001$ in figure 4.10 and $\mu_1 = \mu_2 = 0.00005$ in figure 4.12 shows that in the case with higher viscous damping the wave contours are overly-diffusive with very smoothly varying front. Unlike the case with high attenuation, the wave impulse in the low viscosity domain has a highly-transient pattern with a sharp wave front due to the high-frequency components of the dynamic response. It is noted that the high-frequency contents get dissipated by increasing the physical damping of the system which contributes to more diffusive wave patterns and results in losing the highly-transient behaviour and the sharp wave front.

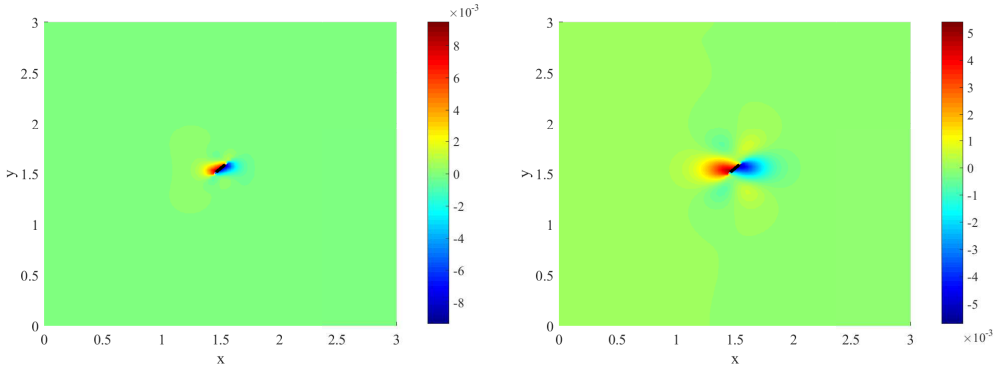

(a) $t = 0.0008s$ (b) $t = 0.0023s$

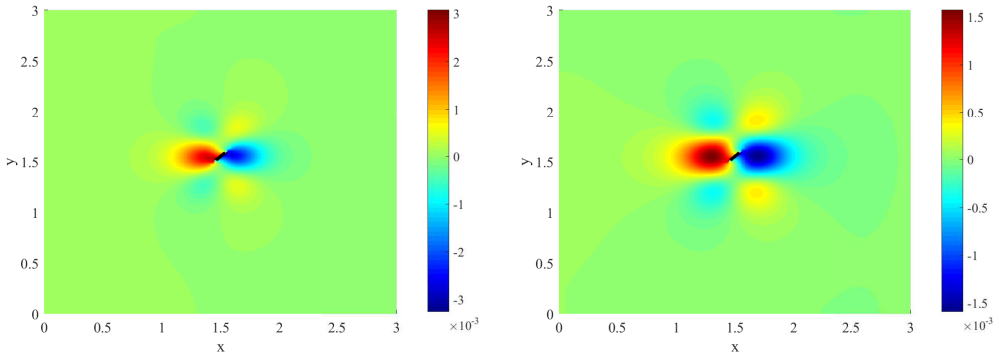

(c) $t = 0.0030s$ (d) $t = 0.0038s$

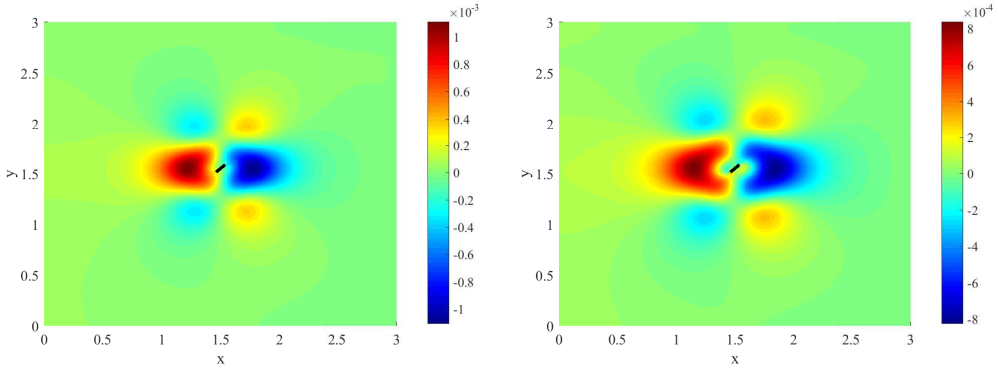

(e) $t = 0.0045s$ (f) $t = 0.0053s$

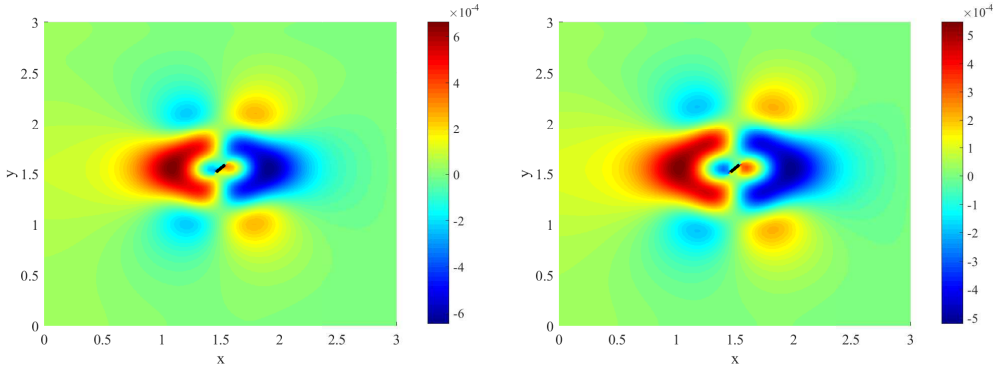

(g) $t = 0.0060s$ (h) $t = 0.0068s$

Fig. 4.9: x-velocity contour of acoustic wave propagation under shear failure.

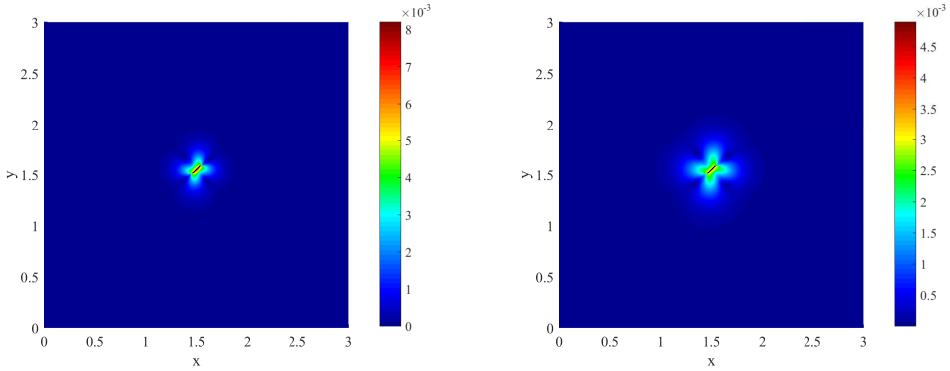

(a) $t = 0.0015s$ (b) $t = 0.0022s$

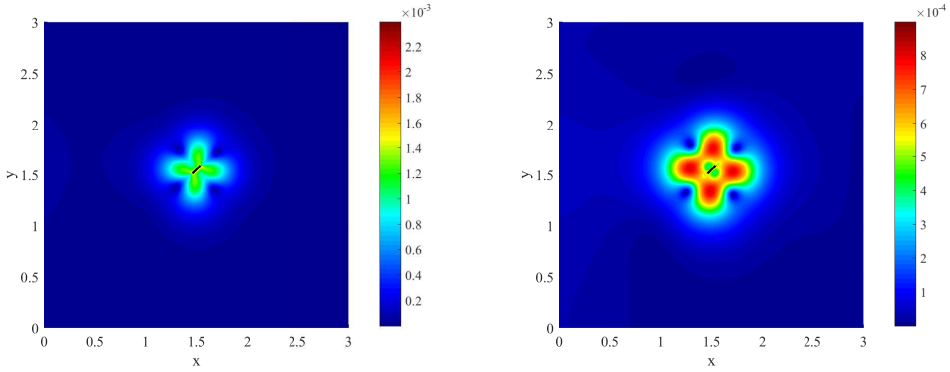

(c) $t = 0.0030s$ (d) $t = 0.0037s$

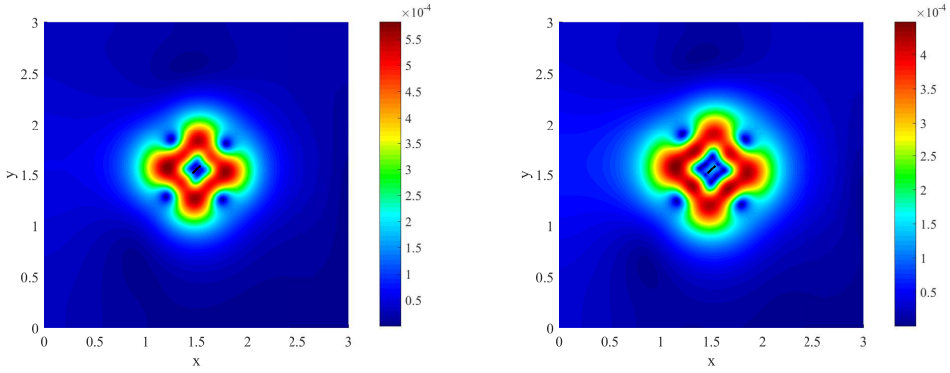

(e) $t = 0.0045s$ (f) $t = 0.0052s$

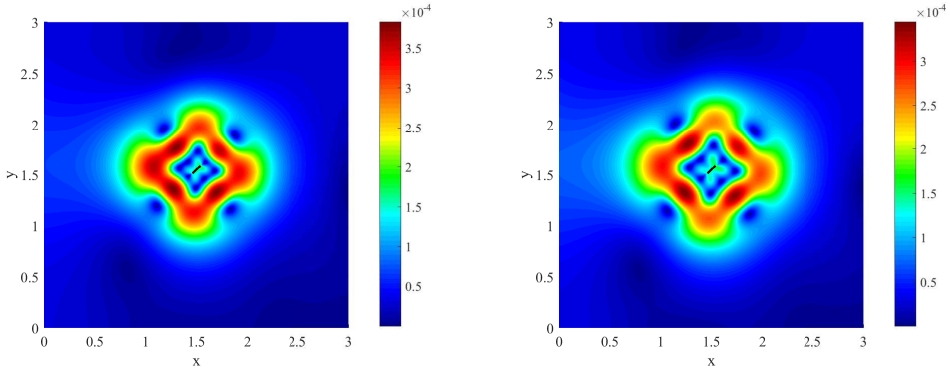

(g) $t = 0.0060s$ (h) $t = 0.0067s$

Fig. 4.10: Absolute velocity contours of acoustic wave propagation under shear failure with viscous damping coefficients $\mu_1 = \mu_2 = 0.001$.

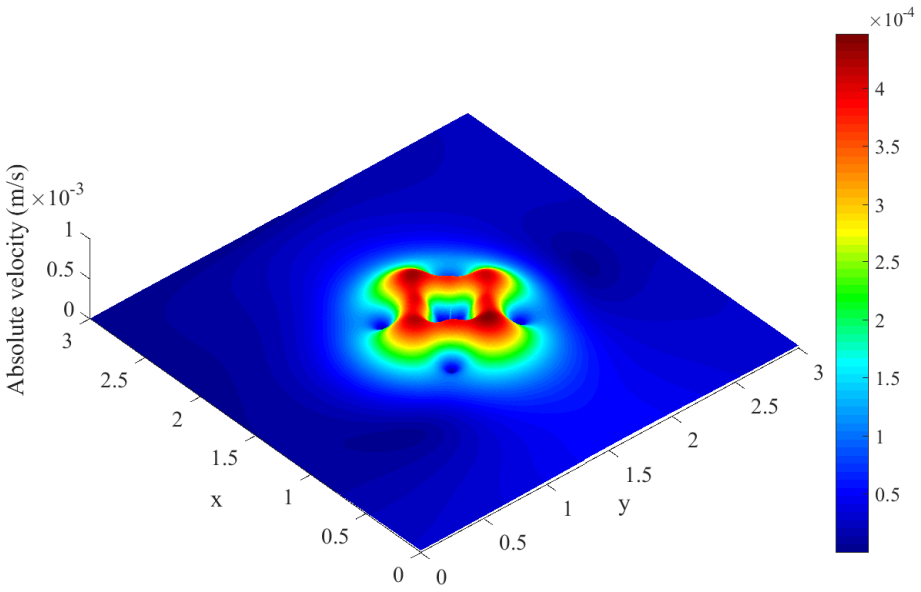

Fig. 4.11: Absolute velocity wave pattern of acoustic emission at $t = 0.0047s$.

Microseismic emission from multiple cracks and coalescence of waves

We consider the domain that was assumed in the previous example with the same loading condition and characteristics. In this case two identical sloping cracks (with the same length and direction as the previous example) are embedded in the medium as shown in figure 4.13. The process of concurrent acoustic emissions from the fractures, and interaction of the emitted waves are illustrated in figure 4.13 through snapshots of the velocity contours in some time steps.

To show the versatility of the method in modeling multiple randomly-distributed cracks, figure 4.14 illustrates the AE patterns induced by shear slip on discontinuities at $t = 0.005s$. The same in-situ stress and boundary conditions as the previous example are considered and the poroelastic domain is assumed to be $3 \times 3m$.

Discretization sensitivity

In this part the discretization-sensitivity of the developed model in simulation of induced AEs is assessed. To this end, a porous media of size $3 \times 3m$ is considered with a single fracture of length $0.2m$ located at the center of the domain. The same in-situ stress and boundary conditions

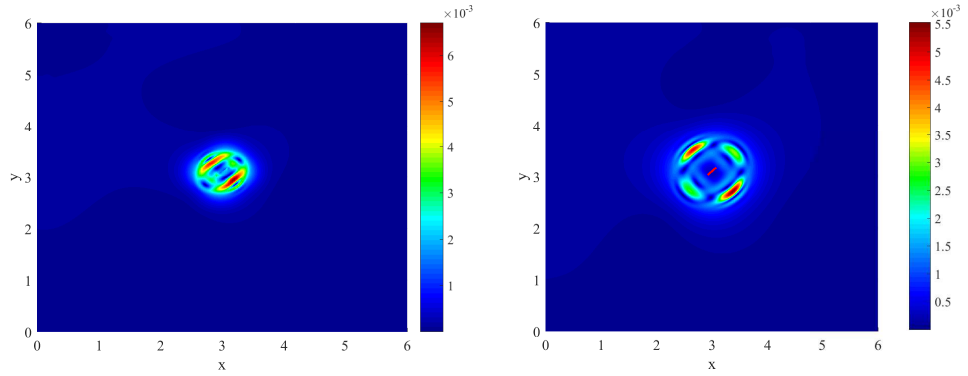

(a) $t = 0.0050s$ (b) $t = 0.0100s$

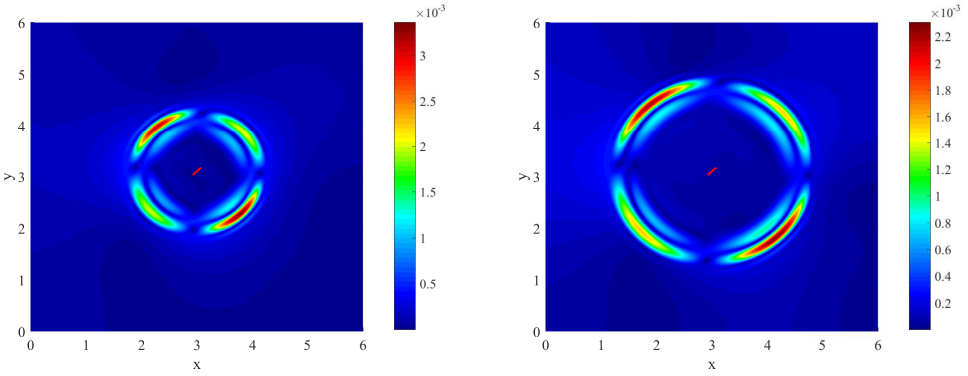

(c) $t = 0.0200s$ (d) $t = 0.0300s$

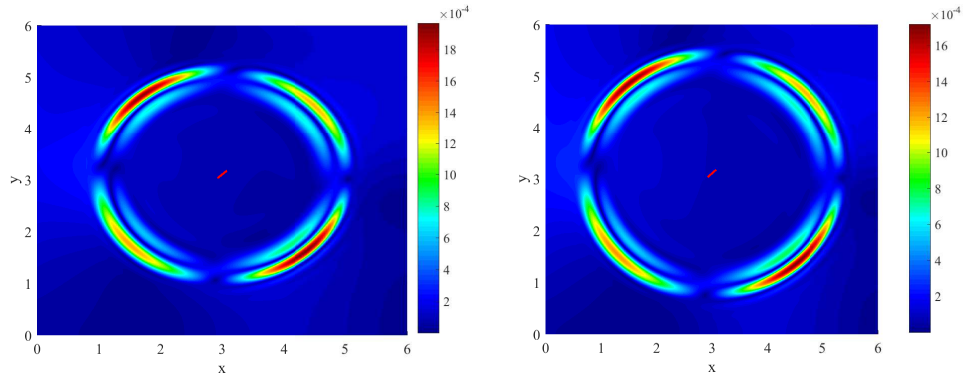

(e) $t = 0.03500s$ (f) $t = 0.0400s$

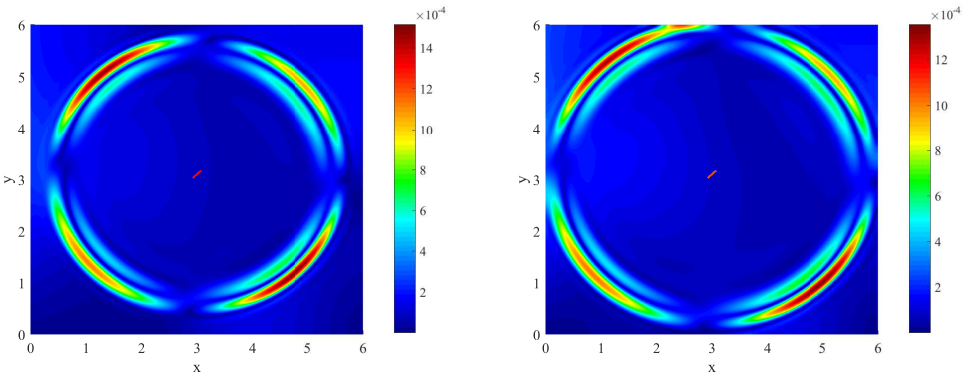

(g) $t = 0.0450s$ (h) $t = 0.0500s$

Fig. 4.12: Absolute velocity contours of acoustic wave propagation under shear failure with viscous damping coefficients $\mu_1 = \mu_2 = 0.00005$.

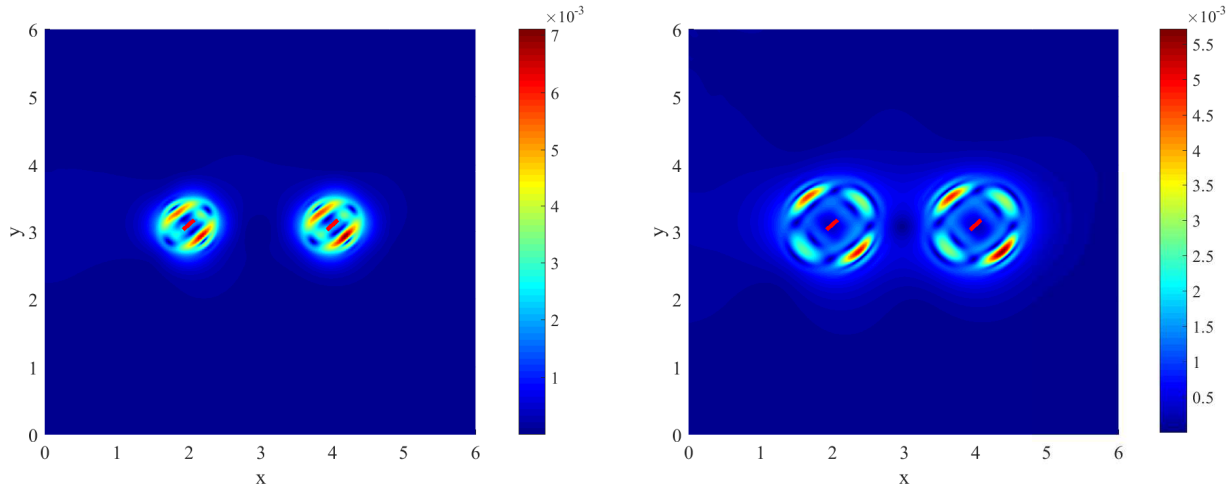

(a) $t = 0.0050s$ (b) $t = 0.0100s$

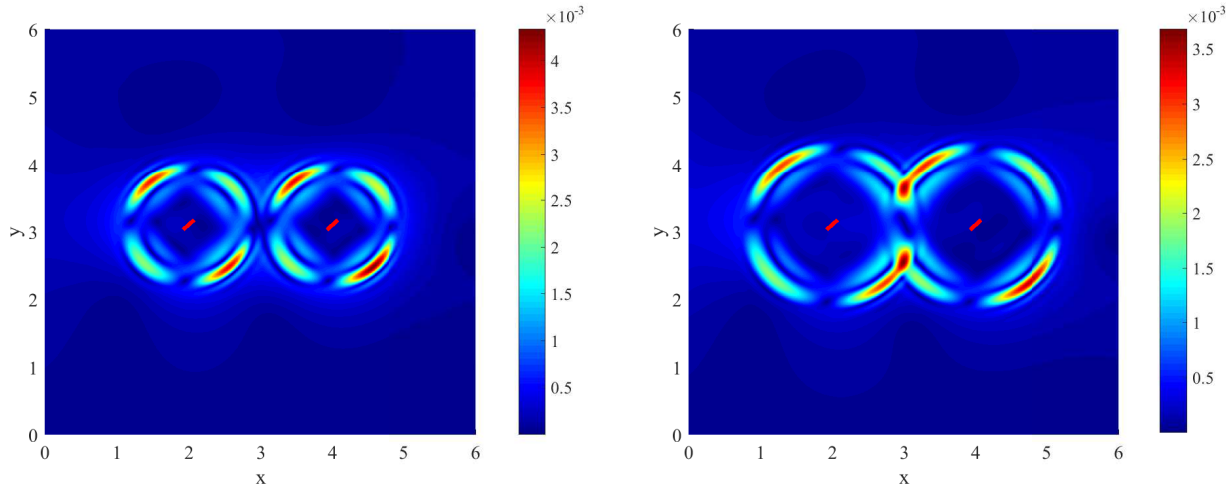

(c) $t = 0.0150s$ (d) $t = 0.0200s$

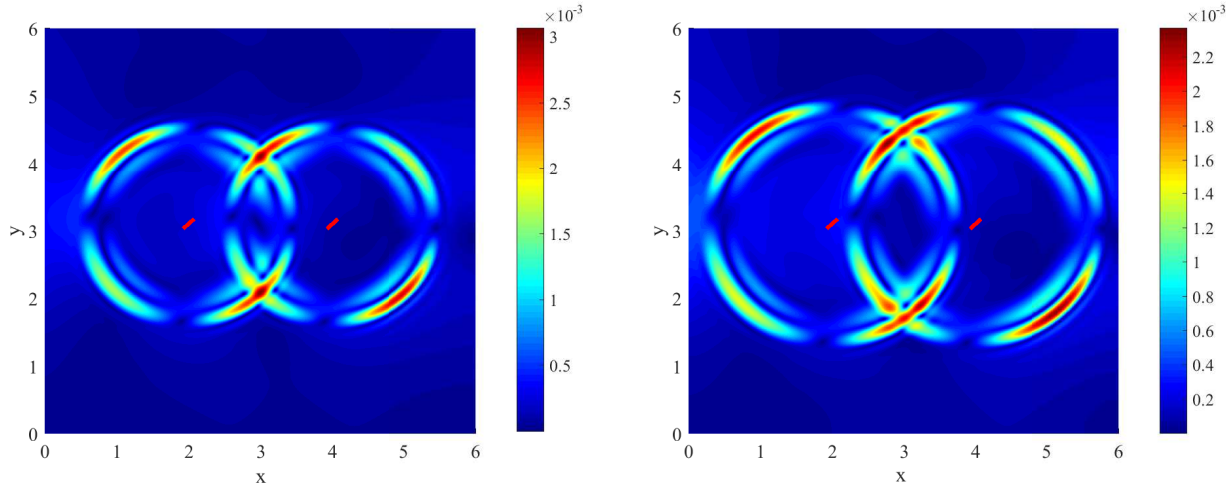

(e) $t = 0.0250s$ (f) $t = 0.0300s$

Fig. 4.13: Absolute velocity contours of acoustic wave propagation due to double shear failures and interaction of emitted waves.

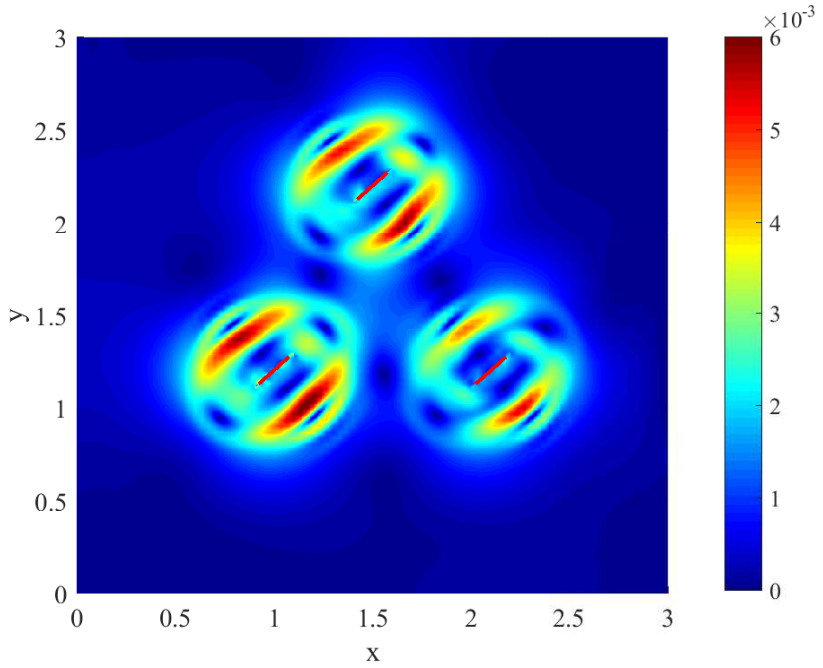

Fig. 4.14: AE wave pattern induced by shear slip instability of multiple randomly-distributed fractures at $t = 0.005s$.

and material properties as the previous example are assumed. Figure 4.15 demonstrates AE wave patterns at $t = 0.01s$ using different mesh sizes. As seen, the amplitude of the wave pulse is dependent on the mesh resolution, and the results are convergent by refining the mesh. It is important to note that in simulation of the shear slip instability (i.e., frictional contact behviour at the interface) and the corresponding acoustic wave propagation, sufficiently refined meshes ar required to obtain results with acceptable precision.

4.5.2 Acoustic emission due to injection-induced slip instability

A $1m$ by $0.5m$ porous medium discretized by 30×10 rectangular elements is considered. The domain is assumed to be under the effect of a bilateral confining tractions of $2kN/m^2$ on the left and top edges. A $0.36m$ long inclined crack is embedded at the angle of $\theta = 56^0$ with respect to the horizontal direction. The friction coefficient is assumed to be $\mu_f = 0.8$. Damping coefficients of the solid skeleton are considered as $\mu_1 = 0.1, \mu_2 = 0.1$. The domain, the fracture, and applied loads are depicted in figure 4.16. A PNM-GFEM-M model with $n = 1$ is used with

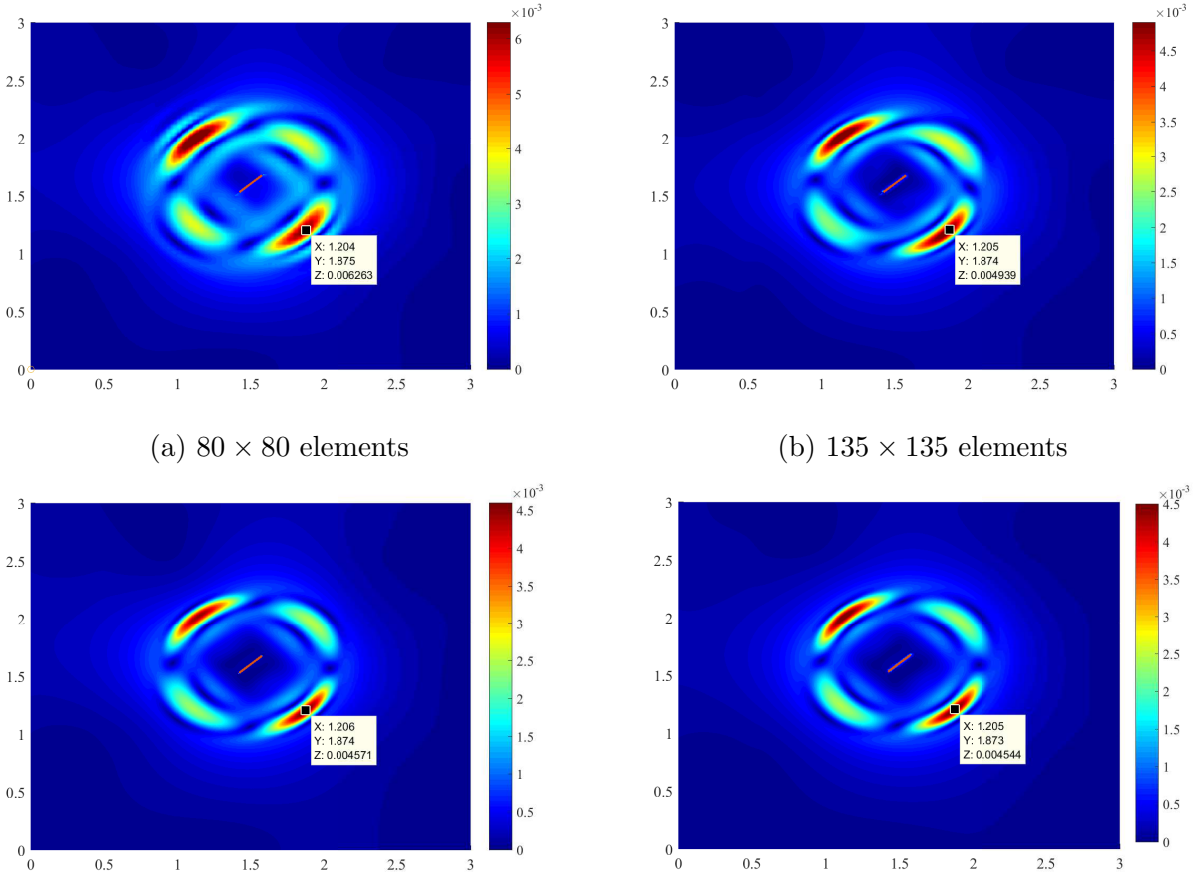

(a) 80 × 80 elements

(b) 135 × 135 elements

(c) 180 × 180 elements

(d) 200 × 200 elements

Fig. 4.15: Mesh-sensitivity study of an AE wave pattern.

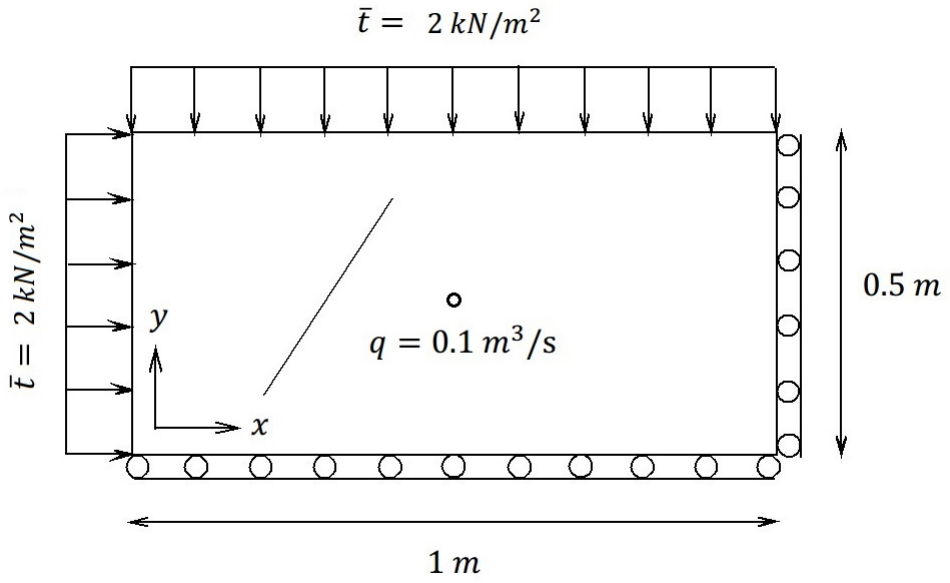

Fig. 4.16: A schematic figure of fractured porous media under confining tractions and point injection at the middle, considered in section 4.5.2.

time step size of $\Delta t = 1$ms.

The simulation commences by applying a constant fluid flux injection of $q = 0.1m^3/s$ at the center of the domain at $t = 0.0s$. Prior to applying the injection, strain energy is stored in the system due to the initial stress caused by confining tractions and the frictional contact at the interface of the fracture.

Due to injection of the fluid, a sudden slip between fracture faces occurs along the interface. This abrupt transition from a stick condition to a slip situation induces an AE response- the rapid release of strain energy results in the stimulation of inertia effects. Figure 4.17 depicts the acoustic signal at point $(x = 0.9667, y = 0.25)$ induced by the injection perturbation. As seen in this figure, in the case in which there is no frictional resistance/contact at the fracture interface (i.e., when $\mu_f = 0.0$), no acoustic behaviour is observed in the dynamic response of the system, which is quite rational and expected. In the case of $\mu_f = 0$ (no friction and therefore no stick condition under the in-situ stresses), unlike the frictional contact case, there is no sudden transition from a stick to a slip state. This is why no acoustic response is seen in the case of frictionless interface.

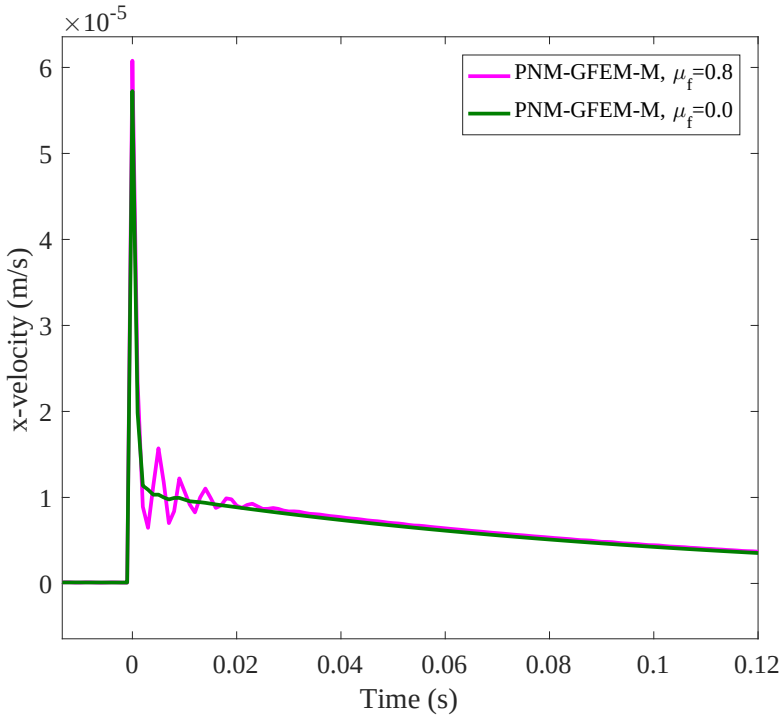

Fig. 4.17: Acoustic signal at point $(x = 0.9667, y = 0.25)$, induced due to a sharp switch from stick to slip condition at the fracture interface under injection.

4.6 Chapter Conclusions

Acoustic emission (AE) induced by shear failure and slip along fractures in porous media is simulated and the role of permeability, interface friction and other system characteristics on the AE are studied. To model interface (e.g., fracture or fault) in continua, Phantom Node Method (PNM) is used in conjunction with global Generalized Finite Element Method (GFEM) harmonic enrichment functions to solve dynamic/wave propagation problem. A seismic emission is triggered by the sudden release of strain energy, which occurs due to an abrupt switch from a stick to a slip condition (localization) in the form of interface snap-through instability/bifurcation. The required perturbation for instability stimulation at the interface is provided through an external excitation such as fluid injection in the vicinity of the fracture under confining stresses and frictional contact conditions.

Effects of mechanical characteristics such as viscous damping parameters of the solid phase,

permeability of porous media, and interface friction on AE are assessed based on the numerical simulations performed using the proposed computational model. It should be noted that there was no available data in the literature to use for conducting comparison studies over the results obtained for AEs by the developed method of the present paper. Therefore, further research studies (numerical and experimental) should be carried out as scientific supports for the conclusions of this paper. Based upon the simulation results of the method introduced in this paper, it is found that the acoustic response in lower permeability cases shows higher frequency and lower amplitude signals. Increasing the damping magnitude significantly affects the spectral contents of the acoustic signal by attenuating the high-frequency components and decreasing the corresponding magnitudes. By increasing damping, the acoustic emission pattern changes from the state of very transient wave propagation to overly-diffusive (diffusion-dominated) response. Also, it is shown that the magnitude of induced acoustic signal is directly dependent on the friction coefficient at the interface. The superiority of the enriched mixed finite element model in simulation of acoustic waves and suppressing the spurious oscillations in pore pressure and velocity time signals that appear in acoustic simulation using regular finite element approach is also demonstrated.

As shown throughout the article, the proposed PNM-GFEM-M numerical model is a very promising computational approach for simulation of localization-induced acoustic/seismic waves in fractured porous media. However, many items need to be tackled in future studies to move towards more practical acoustic emission simulations. In this study we mostly focused on showing the capability of the numerical scheme in simulation of acoustic waves induced by local abrupt release of energy in porous media and did not concentrate on interface constitutive modeling of failure and weakening. This article does not focus on the effectiveness of the methodology in terms of computational costs for large-scale problems. Hence, future research works should focus on solving large scale problems in practical applications like earthquakes and microseismic monitoring in hydraulic fracturing. Lastly, since in many practical applications AEs are triggered and propagated in three-dimensional spaces, the extension of the current 2D

model to 3D would be of great practical value.

Chapter 5

Conclusions, Publications, and Future works

5.1 Conclusions

In this PhD thesis a new computational method has been introduced, developed, and implemented in the context of the Partition-of-Unity Finite Element Method (PUFEM) to simulate the coupled problem of fracture instability/reactivation and induced acoustic/microseismic wave emission in porous media under frictional contact condition in applications like Hydraulic Fracturing (HF).

HF is a very common means of stimulation for unconventional reservoirs to increase the efficiency of oil and gas extraction from tight formations by increasing the permeability through creating networks of fractures by hydraulic pressurization via injection of fracturing fluid deep into the ground. HF is one of the most challenging engineering problems due to the complex and coupled physics involved and also very high level of uncertainties that exist around it because of the indeterministic features of the problem. Moreover, HF has remained poorly understood from the mechanics point of view and most of the research work reported on the related topics either suffer from very extensive simplifications and assumptions or focus on very specific tiny aspects of the problem without accounting for other coupled features involved.

Reactivation of natural faults and fractures (microseismicity and acoustic emission) and contamination of aquifers and underground water are two important environmental concerns about HF. An abrupt switch from stick to slip condition and shear/tensile rupturing may happen at the fracture interfaces due to the change in stress pattern under pressurizing through fracturing fluid injection in applications like HF. Also, the behaviour of formations and fractures can be probed by analyzing the acoustic emissions induced during hydraulic stimulations. The biggest challenge in simulation of acoustic emission due to fracture/material instability is to come up with a coupled numerical solution that can concurrently handle the localization and the resulting induced acoustic emission.

It is noteworthy that the dominant approach in accurate simulation of wave propagation is to use spectral methods in the context of the frequency domain solutions. However, the localization (or slip instability) aspect of the problem has to be solely and exclusively modeled in time domain as it physically has nothing to do with the frequency domain. To rectify and treat this difficulty, in this PhD research a new enriched finite element model has been developed and implemented based on a combination between the local and global PUFEMs. The local effect of shear failure or slip-instability is modeled using the Phantom Node Method (PNM) in the framework of the local PUFEM. Also, to more accurately model acoustic wave emission in time domain, fundamental harmonic basis functions that appear in spectral analysis and analytical solutions of waves are embedded in the finite element interpolations as enrichment functions in the context of the global PUFEM or Generalized Finite Element Method (GFEM).

Using the proposed approach, the coupled problem of discontinuity reactivation and acoustic wave emission and propagation can be simulated entirely and concurrently in the time domain. The developed numerical model is named mixed GFEM-enriched PNM or PNM-GFEM-M. The availability of accurate computational tools like the one developed in this research can help to improve understanding about the behaviour of naturally fractured formations under hydromechanical stimulations. Also, numerical models can be very effective in developing realistic correlations between the characteristics of the fracturing/damaging zone and acoustic signals recorded at specific locations of the field through inverse analysis (or trained neural network algorithms) which can be of exceptional practical values in microseismic monitoring and acoustic emission industry.

Being a coupled nonlinear mixed multi-physics problem, there are several mechanical and computational complexities and difficulties involved in this project in terms of accuracy, stability, and convergence issues. The numerical difficulties stem from the high-frequency transient feature of wave propagation and also the coupled physics and interface modeling aspects involved in the problem.

In Chapter 1 an introduction to the problem of interest has been given. Also, discussions have been provided about different solution methods and computational challenges and difficulties that arise in fracture, contact, and wave propagation simulation.

Chapter 2 describes a new enriched finite element model for simulation of wave propagation in fractured media. The method is based on a combined advantages of a local PUFEM (i.e., PNM) to model discontinuity and global PUFEM (using trigonometric enrichments) to model transient wave phenomena. Different numerical examples are used to illustrate the capability of the developed enriched finite element method in more accurate simulation of wave propagation in fractured media in comparison with conventional finite element models. The examples and the numerical methods provided in the chapter are identically published through a journal paper.

In Chapter 3 the computational method is extended to the case of multi-physics porous media. In this case the displacement fields as well as the pore pressure are interpolated using enrichment function. Moreover, the frictional contact condition at interfaces is modeled through an augmented Lagrange multiplier method. The developed mixed enriched finite element method is shown to be very effective in suppressing the spurious oscillations emerging from the Gibbs phenomenon and numerical dispersions that are attributed to the LBB condition in coupled problems. The methodology and numerical examples of the chapter are disseminated through a journal article.

Chapter 4 investigates the use of the developed enriched mixed finite element model (i.e., PNM-GFEM-M) in simulation of coupled problem of shear failure – acoustic emission wave propagation in fractured porous media. Through several numerical examples, velocity and pore pressure wave patterns induced by release of strain energy due to sudden change from stick to slip condition at interfaces are illustrated. Also, the effects of different system parameters such

as permeability, viscous damping coefficients, and friction coefficient of the interface on the induced acoustic signals are assessed. It is shown that the properties of the porous media and also the discontinuity have significant influences on the characteristics of the received acoustic signals and can drastically alter the frequency contents and the type of the AE response. The provided results of this chapter are identically reported through a journal article.

5.2 Publications

In this section the list of peer-reviewed journal papers and conference articles emanated from this PhD research is given.

5.2.1 Journal papers

• **Komijani M.**, Gracie R., Enriched Mixed Finite Element Models for Dynamic Analysis of Continuous and Fractured Porous Media, *Computer Methods in Applied Mechanics and Engineering*, 343: 74–99, 2019.

• **Komijani M.**, Gracie R., An Enriched Finite Element Model for Wave Propagation in Fractured Media, *Finite Elements in Analysis and Design*, 125: 14-23, 2017.

• **Komijani M.**, Gracie R., Sarvaramini E., Simulation of Induced Acoustic Emission in Fractured Porous Media, *Engineering Fracture Mechanics*, DOI: 10.1016/j.engfracmech.2018.07.028, 2018.

• **Komijani M.**, Gracie R., Nonlinear thermo-electro-mechanical dynamic behaviour of FGPM beams, *Composite Structures*, 150: 208-218, 2016.

• Sarvaramini E., Dusseault M., **Komijani M.**, Gracie R., A Non-local Plasticity Model of Stimulated Volume Evolution During Hydraulic Fracturing, *International Journal of Solids and Structures*, accepted for publication, 2018.

5.2.2 Conference presentations

• **Komijani M.**, Gracie R., Microseismic Wave Simulation using GFEM-enriched Phantom Node Method, 14^{th} *U.S. National Congress on Computational Mechanics*, Montreal, Canada,

2017.

• **Komijani M.**, Gracie R., An enriched finite element method for wave propagation analysis in discontinuous domain, 24^{th} *International Congress of Theoretical and Applied Mechanics*, Montreal, Canada, 2016.

• **Komijani M.**, Gracie R., Nonlinear Thermo-Electro-Mechanically Induced Vibration of FGPM Beams, 25^{th} *Canadian Congress of Applied Mechanics*, London, Ontario, Canada, 2015.

5.3 Future works

In this section several recommendations are provided as potential topics for extension and continuation of the research that has been reported in this PhD dissertation.

• Verification of the numerical results provided in this thesis with other analytical, semi-analytical, hybrid, and numerical methodologies that may be introduced in future for modeling of the problem.

• Validation of the numerical results with future field data. It is highly recommended to set up some experimental facilities and instruments to conduct real tests even in laboratory scale to study and record acoustic signals induced due to shear instability and failure.

• This research is mainly focused on developing a new computational scheme for simulation of acoustic wave emission induced by shear instability in porous media. However, more detailed investigations are required on improving the cost effectiveness of the approach and decreasing the computational expenses particularly in large scale domains.

• This thesis mostly concentrates on showing the capability of the numerical method in simulation of acoustic waves induced by local abrupt release of energy in multi-physics media and did not particularly and extensively deal with interface constitutive modeling of failure and weakening. It would be worthwhile to conduct substantial research works in future to include more elaborate models to account for the nonlinear complicated physics of localization/fracturing, and mechanics of the interface behaviour.

• Extending the current two-dimensional computer model to three-dimensional can be of great practical value.

Bibliography

[1] Gabriel Hattori, Jon Trevelyan, Charles E. Augarde, William M. Coombs, Andrew C. Aplin. Numerical Simulation of Fracking in Shale Rocks: Current State and Future Approaches. *Arch Computat Methods Eng* (2016).

[2] Daniel J. Soeder, Shikha Sharma, Natalie Pekney, Leslie Hopkinson, Robert Dilmore, Barbara Kutchko, Brian Stewart, Kimberly Carter, Alexandra Hakala, Rosemary Capo, An approach for assessing engineering risk from shale gas wells in the United States. *International Journal of Coal Geology*, 126, 419 (2014).

[3] US Energy Information Administration (EIA). Top 5 product states' combined marketed natural gas output rose in 2011. 2012.

[4] Energy Information Administration (EIA) and Lippman consulting. Shale gas and the outlook for US natural gas markets and global gas resources. 2011.

[5] Alberta Government and KPMG International. Industry and economy. 2011.

[6] Guo J., Liu Y., A comprehensive model for simulating fracturing fluid leakoff in natural fractures. *J. Nat. Gas Sci. Eng.*, 21, 977–985 (2014).

[7] T.K. Perkins, L.R. Kern., Widths of Hydraulic Fractures. *Journal of Petroleum Technology*, 13, 937949 (1961).

[8] J. Geertsma, F. De Klerk., A Rapid Method of Predicting Width and Extent of Hydraulically Induced Fractures. *Journal of Petroleum Technology* , 21, 15711581 (1969).

[9] S. H. Advani, T. S. Lee, J. K. Lee. Three-Dimensional Modeling of Hydraulic Fractures in Layered Media: Part I Finite Element Formulations. *Journal of Energy Resources Technology*, 112, 1 (1990).

[10] L. Vandamme, J. H. Curran. A three-dimensional hydraulic fracturing simulator. *International Journal for Numerical Methods in Engineering*, 28, 909927 (1989).

[11] Schrefler BA, Secchi S and Simoni L., On adaptive refinement techniques in multi-field problems including cohesive fracture. *Computer Methods in Applied Mechanics and Engineering*, 2006; 195: 444461.

[12] Secchi S, Simoni L, Schrefler BS. Mesh adaptation and transfer schemes for discrete fracture propagation in porous materials. *International Journal for Numerical and Analytical Methods in Geomechanics*, 2007; 31: 331345.

[13] T.A Cruse, F.J Rizzo. A direct formulation and numerical solution of the general transient elastodynamic problem. *I. Journal of Mathematical Analysis and Applications*,22, 244259 (1968).

[14] A. Portela, M.H. Aliabadi, D.P. Rooke. Dual boundary element incremental analysis of crack propagation. *Computers & Structures*, 46, 237247 (1993).

[15] M.H. Aliabadi, A.L. Saleh. Fracture mechanics analysis of cracking in plain and reinforced concrete using the boundary element method. *Engineering Fracture Mechanics*, 69, 267280 (2002).

(1998)

[16] Hallquist JO . LS-DYNA theory manual. Livemore software technology corporation, USA, 42, 239250 (1998).

[17] Jeong-Hoon Song, Hongwu Wang, Ted Belytschko. A comparative study on finite element methods for dynamic fracture. *Computational Mechanics*, 42, 239250 (2007).

[18] X.-P. Xu, A. Needleman. Numerical simulations of fast crack growth in brittle solids. *Journal of the Mechanics and Physics of Solids*, 42, 13971434 (1994).

[19] G.T. Camacho, M. Ortiz. Computational modelling of impact damage in brittle materials. *International Journal of Solids and Structures*, 33, 28992938 (1996).

[20] J.M. Melenk, I. Babuška. The partition of unity finite element method: Basic theory and applications. *Computer Methods in Applied Mechanics and Engineering*, 139, 289-314 (1996).

[21] Vamaraju J., Sen M., De Basabe J. and Wheeler M., A comparison of continuous, discontinuous, and enriched Galerkin finite-element methods for elastic wave-propagation simulation. *SEG Technical Program Expanded Abstracts*, 4063–4067 (2017).

[22] Lee S., Wheeler M.F., Adaptive enriched Galerkin methods for miscible displacement problems with entropy residual stabilization. *Journal of Computational Physics*, 331, 19–37 (2017).

[23] Lee S., Lee Y.J., Wheeler M.F., A locally conservative enriched Galerkin approximation and efficient solver for elliptic and parabolic problems. *SIAM Journal on Scientific Computing*, 38(3), A1404–A1429 (2016).

[24] Belytschko T, Black T. Elastic crack growth in finite elements with minimal remeshing. *International Journal for Numerical Methods in Engineering* , 1999; 45: 601620.

[25] Belytschko, T., Liu, W.K., Moran, B., Nonlinear finite elements for continua and structures. *John wiley & sons*. (2000).

[26] Nicolas Moës, John Dolbow, Ted Belytschko. A finite element method for crack growth without remeshing. *International Journal for Numerical Methods in Engineering*, 46, 131-150 (1999).

[27] Belytschko T., Gracie R., Ventura G., A review of extended/generalized finite element methods for material modeling. *Modelling and Simulation in Materials Science and Engineering*, 17, 043001 (2009).

[28] P. Gupta, J.P. Pereira, D.-J. Kim, C.A. Duarte, T. Eason, Analysis of three-dimensional fracture mechanics problems: A non-intrusive approach using a generalized finite element method. *Engineering Fracture Mechanics*, 90, 41-64 (2012).

[29] Jeong-Hoon Song, Pedro M. A. Areias, Ted Belytschko. A method for dynamic crack and shear band propagation with phantom nodes. *International Journal for Numerical Methods in Engineering*, 67, 868-893 (2006).

[30] Chau-Dinh T., Zi G., Lee P.S., Rabczuk T., Song J.H., Phantom-node method for shell models with arbitrary cracks. *Computers & Structures*, 92, 242–256 (2012).

[31] Anita Hansbo, Peter Hansbo. A finite element method for the simulation of strong and

weak discontinuities in solid mechanics.*Computer Methods in Applied Mechanics and Engineering* , 193, 3523-3540 (2004).

[32] M. Komijani, R. Gracie. An Enriched Finite Element Model for Wave Propagation in Discontinuous Media.*Finite Elements in Analysis and Design*, 125: 14-23, 2017.

[33] Yoon Y. C., Song J. H., Extended particle difference method for moving boundary problems. *Computational Mechanics*, 54, 723–743 (2014).

[34] Yoon Y. C., Song J. H., Extended particle difference method for weak and strong discontinuity problems: part I. Derivation of the extended particle derivative approximation for the representation of weak and strong discontinuities. *Computational Mechanics*, 53(6), 1087–1103 (2014).

[35] Yoon Y. C., Song J. H., Extended particle difference method for weak and strong discontinuity problems: part II. Formulations and applications for various interfacial singularity problems. *Computational Mechanics*, 53(6), 11051128 (2014).

[36] Komijani M, Gracie R., Enriched Mixed Finite Element Models for Dynamic Analysis of Continuous and Fractured Porous Media, *Computer Methods in Applied Mechanics and Engineering*, Under publication (2018).

[37] Komijani M, Gracie R., Sarvaramini E., Simulation of Induced Acoustic Emission in Fractured Porous Media, *Engineering Fracture Mechanics*, DOI: 10.1016/j.engfracmech.2018.07.028 (2018).

[38] P A. Cundall, R D. Hart. Numerical modeling of discontinua.*Engineering Computations*, 9, 101113 (1992).

[39] C. Miehe, M. Hofacker, F. Welschinger, A phase field model for rateindependent crack propagation: robust algorithmic implementation based on operator splits.*Computer Methods in Applied Mechanics and Engineering* , 199 (45-48), 2765–2778 (2010).

[40] C. Miehe, F. Welschinger, M. Hofacker, Thermodynamically consistent phasefield models of fracture: variational principles and multi-field fe implementations.*Int. J. Numer. Methods Engrg*, 83 (10), 1273–1311 (2010).

[41] Borden, M.J., Verhoosel, C.V., Scott, M.A., Hughes, T.J. and Landis, C.M., A phase-

field description of dynamic brittle fracture.*Computer Methods in Applied Mechanics and Engineering* , 217, 77-95 (2012).

[42] Boone TJ, Ingraffea AR. A numerical procedure for simulation of hydraulically-driven fracture propagation in poroelastic media. *International Journal for Numerical and Analytical Methods in Geomechanics*, 14: 2747 (1990).

[43] Khoei, A. R. (2014). Extended finite element method: theory and applications. John Wiley & Sons.

[44] Wang, X., Shi, F., Liu, H., & Wu, H.A. Numerical simulation of hydraulic fracturing in orthotropic formation based on the extended finite element method. *Journal of Natural Gas Science and Engineering*, 33, 56-69 (2016).

[45] Zhang Z, Ghassemi A. Simulation of hydraulic fracture propagation near a natural fracture using virtual multidimensional internal bonds. *International Journal for Numerical and Analytical Methods in Geomechanics* 2011; 35: 480495.

[46] Irwin GR. Analysis of stresses and strains near the end of a crack traversing a plate. *Journal Applied Mechanics*, 24:361-364 (1957).

[47] Williams ML. On the stress distribution at the base of a stationary crack. *Journal of Applied Mechanics*, 24:109114 (1957).

[48] Gordeliy, E. and Peirce, A., Enrichment strategies and convergence properties of the XFEM for hydraulic fracture problems. *Computer Methods in Applied Mechanics and Engineering*, 283:474-502 (2015).

[49] Erdogan F, Sih G. On the Crack Extension in Plates Under Plane Loading and Transverse Shear. *J. Basic Eng*, 85(4), 519-525 (1963).

[50] Saouma, V. E., Ayari, M. L., & Leavell, D. A. Mixed mode crack propagation in homogeneous anisotropic solids. *Engineering Fracture Mechanics*, 27(2), 171-184 (1987).

[51] Hussain M, Pu S, Underwood J. Strain energy release rate for a crack under combined mode I and mode II. *Fract Anal ASTM-STP*, 560:228 (1974).

[52] Hoek E., Bieniawski Z. T. Brittle fracture propagation in rock under compression. *International Journal of Fracture Mechanics*, 1(3), 137-155 (1965).

[53] NematNasser S., Horii H. Compressioninduced nonplanar crack extension with application to splitting, exfoliation, and rockburst. *Journal of Geophysical Research*, 87(B8), 6805-6821 (1982).

[54] Peric D, Owen DRJ. Computational model for 3D contact problems with friction based on the penalty method. *International Journal for Numerical Methods in Engineering*, 35: 12891309. (1992).

[55] Wriggers P., Computational contact mechanics. *Springer*. (2006).

[56] Simo JC, Laursen T. An augmented Lagrangian treatment of contact problems involving friction. *Computers and Structures* , 42: 97116. (1992).

[57] Wriggers P. Computational Contact Mechanics. New York: Springer, 2006.

[58] Bazant Z.P., Planas J., Fracture and size effect in concrete and other quasibrittle materials. Boca Raton: CRC Press, 1998.

[59] Dugdale D. S., Yielding of steel sheets containing slits. *Journal of the Mechanics and Physics of Solids*, 8(2): 100-104. (1960).

[60] Barenblatt G. I., The mathematical theory of equilibrium cracks in brittle fracture. *Advances in applied mechanics*, 7(1): 55-129. (1962).

[61] Moës N. and Belytschko T., Extended finite element method for cohesive crack growth. *Engineering fracture mechanics*, 69 (7): 813-833. (2002).

[62] Zi G. and Belytschko T., New crack-tip elements for XFEM and applications to cohesive cracks. *International Journal for Numerical Methods in Engineering*, 57: 22212240. (2003).

[63] Lockner D., The role of acoustic emission in the study of rock fracture. *International Journal of Rock Mechanics and Mining Sciences & Geomechanics Abstracts*, 30(7): 883-899. (1993).

[64] Carpinteri A. , Xu J., Lacidogna G., Manuello A., Reliable onset time determination and source location of acoustic emissions in concrete structures. *Cement & Concrete Composites*, 34, 529–537 (2012).

[65] Xu J., Fu Z., Han Q., Lacidogna G., Carpinteri A. , Micro-cracking monitoring and fracture evaluation for crumb rubber concrete based on acoustic emission techniques. *Structural*

Health Monitoring, 1475921717730538 (2017).

[66] Han Q. , Xu J., Carpinteri A., Lacidogna G., Localization of acoustic emission sources in structural health monitoring of masonry bridge. *Structural Control and Health Monitoring*, 22, 314–329 (2015).

[67] Obert L., Duvall W., Micro-seismic method of determining the stability of underground openings. *Technical report, U.S. Bureau of Mines*, (1957).

[68] Pearson C., The relationship between microseismicity and high pore pressures during hydraulic stimulation experiments in low permeability granitic rocks. *J. geophys. Res.*, 86(B9): 78557864. (1981).

[69] Iturrioz I., Lacidogna G., Carpinteri A., Experimental analysis and truss-like discrete element model simulation of concrete specimens under uniaxial compression. *Engineering Fracture Mechanics*, 110, 81–98 (2013).

[70] Birck G., Iturrioz I., Lacidogna G., Carpinteri A., Damage process in heterogeneous materials analyzed by a lattice model simulation. *Engineering Failure Analysis*, 70, 157–176 (2016).

[71] Lisjak A., Liu Q., Zhao Q., Mahabadi O. K., Grasselli G., Numerical simulation of acoustic emission in brittle rocks by two-dimensional finite-discrete element analysis. *Geophysical Journal International* , 195(1): 423-443. (2013).

[72] Hazzard J., Young R., Simulating acoustic emissions in bondedparticle models of rock. *Int. J. Rock Mech. Min. Sci.*, 37(5): 867872. (2000).

[73] Gutenberg B., The energy of earthquakes. *Q. J. geol. Soc.*, 112: 114. (1956)

[74] Bathe KJ., Finite element procedures. *Prentice Hall.* (1996).

[75] Gottlieb D., Orszag S.A., Numerical analysis of spectral methods: Theory and applications. *Capital City Press.* (1993).

[76] Gopalakrishnan S, Chakraborty A, Roy Mahapatra D, Spectral finite element method. *Springer-Verlag.* (2008).

[77] Chakraborty A., Gopalakrishnan S., A spectral finite element model for wave propagation analysis in laminated composite plate. *J Vib Acoust.* 128: 47788. (2006).

[78] Kohno H., Bathe K.J., Wright J.C., A finite element procedure for multiscale wave equations with application to plasma waves. *Comput Struct*. 88: 8794. (2010).

[79] Ham S., Bathe K.J., A finite element method enriched for wave propagation problems. *Comput Struct*. 94-95: 1-12. (2012).

[80] Newmark N. M., A method of computation for structural dynamics. *Journal of the engineering mechanics division ASCE*. 85(3): 67-94. (1959).

[81] Chung J., Lee J. M., A new family of explicit time integration methods for linear and nonlinear structural dynamics. *International Journal for Numerical Methods in Engineering*. 37(23): 3961-3976. (1994).

[82] Chung J, Lee JM, A new family of explicit time integration methods for linear and nonlinear structural dynamics. *Int J Numer Methods Eng*. 37: 3961–76. (1994).

[83] Noh G., Bathe K. J., An explicit time integration scheme for the analysis of wave propagations. *Computers & structures*. 129: 178-193. (2013).

[84] Zi G., and Belytschko T., New cracktip elements for XFEM and applications to cohesive cracks. *International Journal for Numerical Methods in Engineering*. 57(15): 2221-2240. (2003).

[85] T. Menouillard, J. Rthor, A. Combescure, H. Bung. Efficient explicit time stepping for the eXtended Finite Element Method (X-FEM). *International Journal for Numerical Methods in Engineering*, 68, 911939 (2006).

[86] T. Strouboulis, I. Babuška, K. Copps. The design and analysis of the Generalized Finite Element Method. *Computer Methods in Applied Mechanics and Engineering* , 181, 4369 (2000).

[87] O. C. Zienkiewicz, The Finite Element Method, third edition. *Mc-Graw-Hill*, London (1977).

[88] Newmark N. M., A method for computation of structural dynamics *Journal of Engineering Mechanics*, 85, 67-94 (1959).

[89] Biot M.A., Theory of propagation of elastic waves in a fluidsaturated porous solid. I. Lowfrequency range. *The Journal of the acoustical Society of america*, 28(2), 168-178

(1956).

[90] Bouzidi Y., Schmitt D.R., Measurement of the speed and attenuation of the Biot slow wave using a large ultrasonic transmitter. *Journal of Geophysical Research: Solid Earth*, 114(B8) (2009).

[91] Wang X., Shi F., Liu H. and Wu H., Numerical simulation of hydraulic fracturing in orthotropic formation based on the extended finite element method. *Journal of Natural Gas Science and Engineering*, 33, 56-69 (2016).

[92] Adachi J., Siebrits E., Peirce A. and Desroches J., Computer simulation of hydraulic fractures. *International Journal of Rock Mechanics and Mining Sciences*, 44(5), 739-757 (2007).

[93] Bazant ZP, Planas J. Fracture and Size Effect in Concrete and Other Quasibrittle Materials. *Boca Raton, FL, CRC Press*. 1998.

[94] Bocca P., Carpinteri A., Valente S., Mixed mode fracture of concrete. *International Journal of Solids and Structures*, 27(9), 1139-53 (1991).

[95] Jeong-Hoon Song, Ted Belytschko, Dynamic Fracture of Shells Subjected to Impulsive Loads. *Journal of Applied Mechanics*, 76, 051301 (2009).

[96] Thomas Menouillard, Ted Belytschko. Dynamic fracture with meshfree enriched XFEM. *Acta Mechanica* , 213, 53–69 (2010).

[97] Thomas-Peter Fries, Ted Belytschko. The extended/generalized finite element method: An overview of the method and its applications. *International Journal for Numerical Methods in Engineering* , 84, 253–304 (1010).

[98] Anthony T Patera. A spectral element method for fluid dynamics: Laminar flow in a channel expansion. *Journal of Computational Physics*, 54, 468488 (1984).

[99] Dimitri Komatitsch, Jeroen Tromp, Jean-Pierre Vilotte. The spectral element method for elastic wave equations: Application to 2D and 3D seismic problems. *SEG Technical Program Expanded Abstracts*, 54, 1460-1463 (1998).

[100] A. Chakraborty, S. Gopalakrishnan. A Spectral Finite Element Model for Wave Propagation Analysis in Laminated Composite Plate. *J. Vib. Acoust.*, 128, 477 (2006).

[101] Dulip Samaratunga, Ratneshwar Jha, S. Gopalakrishnan. Wave propagation analysis in laminated composite plates with transverse cracks using the wavelet spectral finite element method. *Finite Elements in Analysis and Design*, 89, 1932 (2014).

[102] Jha B, Juanes R, A locally conservative finite element framework for the simulation of coupled flow and reservoir geomechanics. *Acta Geotechnica*, 2(3), 139–153 (2007).

[103] Simon B, Wu J, Carlton M, Kazarian L, France E, Evans J, Zienkiewicz O, Poroelastic dynamic structural models of rhesus spinal motion segments. *Spine*, 10(6), 494–507 (1985).

[104] Levenston M, Frank E, Grodzinsky A, Variationally derived 3-field finite element formulations for quasistatic poroelastic analysis of hydrated biological tissues. *Computer Methods in Applied Mechanics and Engineering*, 156(1), 231246 (1998).

[105] Cowin SC, Bone poroelasticity. *Journal of Biomechanics*, 32(3), 217–238 (1999).

[106] Moeendarbary E, Valon L, Fritzsche M, Harris AR, Moulding DA, Thrasher AJ, Stride E, Mahadevan L, Charras GT, The cytoplasm of living cells behaves as a poroelastic material. *Nat Mater*, 12(3), 253261 (2013).

[107] Terzaghi K., Theoretical soil mechanics. *Wiley: New York*, (1943).

[108] Biot M.A., Mechanics of incremental deformations. *Wiley: Chichester*, (1965).

[109] Lotfian Z, Sivaselvan M.V., A topology-motivated mixed finite element method for dynamic response of porous media. *Int. J. Numer. Meth. Engng* , 00, 135 (2014).

[110] Dai N, Vafidis A, Kanasewich E. R., Wave propagation in heterogeneous porous media: A velocity-stress finite-difference method. *Geophysics* , 60(2), 327–340 (1995).

[111] Li C, Borja RI, Regueiro RA, Dynamics of porous media at finite strain. *Computer methods in applied mechanics and engineering* , 193(36), 3837–3870 (2004).

[112] Zienkiewicz O, Shiomi T, Dynamic behavior of saturated porous media; the generalized Biot formulation and its numerical solution. *International journal for numerical and analytical methods in geomechanics*, 8(1), 71–96 (1984).

[113] Suh JK, Spilker R, Holmes M, A penalty finite element analysis for nonlinear mechanics of biphasic hydrated soft tissue under large deformation. *International Journal for Numerical Methods in Engineering*, 32(7), 1411– 1439 (1991).

[114] Zienkiewicz OC, Chan AHC, Pastor M, et al, Computational Geomechanics with Special Reference to Earthquake Engineering, *John Wiley & Sons, Inc, New York* (1999).

[115] Camacho-Tauta, J., Hassan, A., Cascante, G. and Viana da Fonseca, A., Experimental and Numerical Observations of the Frequency-Domain Method in Bender-Element Testing, *Journal of Geotechnical and Geoenvironmental Engineering*, 143:2:04016096 (2016).

[116] Remij E.W., Remmers J.J.C., Huyghe J.M., Smeulders D.M.J., The enhanced local pressure model for the accurate analysis of uid pressure driven fracture in porous materials, *Computer Methods in Applied Mechanics and Engineering*, 286, 293312 (2015).

[117] Nikolic M., Ibrahimbegovic A., Miscevic P., Discrete element model for the analysis of uid-saturated fractured poro-plastic medium based on sharp crack representation with embedded strong discontinuities, *Computer Methods in Applied Mechanics and Engineering*, 298, 407427 (2016).

[118] Réthoré J., De Borst R., Abella M.A., A discrete model for the dynamic propagation of shear bands in a fluidsaturated medium. *International journal for numerical and analytical methods in geomechanics*, 31(2), 347–370 (2007).

[119] Armero F., Callari C., An analysis of strong discontinuities in a saturated poroplastic solid. *International journal for numerical methods in engineering*, 46(10), 1673–1698 (1999).

[120] Miehe C., Mauthe S., Phase field modeling of fracture in multi-physics problems. Part III. Crack driving forces in hydro-poro-elasticity and hydraulic fracturing of uid-saturated porous media, *Computer Methods in Applied Mechanics and Engineering*, 304, 619655 (2016).

[121] Lee S., Mikelic A., Wheeler M. F., Wick T., Phase-field modeling of proppant-filled fractures in a poroelastic medium, *Computer Methods in Applied Mechanics and Engineering*, 312, 509541 (2016).

[122] Mobasher M.E., Berger-Vergiat L., Waisman H., Non-local formulation for transport and damage in porous media, *Computer Methods in Applied Mechanics and Engineering*, 324, 654688 (2017).

[123] Ji H., Dolbow J. E., On strategies for enforcing interfacial constraints and evaluating jump conditions with the extended finite element method. *International Journal for Numerical Methods in Engineering*, 61(14), 2508–2535 (2004).

[124] Moës N., Béchet E., Tourbier M., Imposing Dirichlet boundary conditions in the extended finite element method. *International Journal for Numerical Methods in Engineering*, 67(12), 1641–1669 (2006).

[125] Hautefeuille M., Annavarapu C., Dolbow J.E., Robust imposition of Dirichlet boundary conditions on embedded surfaces. *International Journal for Numerical Methods in Engineering*, 90(1), 40–64 (2012).

[126] Pettitt S., Baker C., Young R., Dahlstrom L.-O. & Ramqvist, G., The assessment of damage around critical engineering structures using induced seismicity and ultrasonic techniques. *Pure appl. Geophys.*, 159(13), 179–195 (2002).

[127] Smith M. B., Montgomery C., Hydraulic fracturing, *CRC Press* (2015).

[128] Warpinski N.R., Mayerhofer M., Agarwal K., Du J., Hydraulic-fracture geomechanics and microseismic-source mechanisms. *SPE Journal*, 18(04), 766–780 (2013).

[129] Warpinski N.R., Mayerhofer M., Agarwal K., Du J., Hydraulic-fracture geomechanics and microseismic-source mechanisms. *SPE Journal*, 18(04), 766–780 (2013).

[130] Invernizzi S., Lacidogna G. and Carpinteri A., Scaling of fracture and acoustic emission in concrete. *Magazine of Concrete Research*, 65(9), 529–534 (2013).

[131] Invernizzi, S., Lacidogna, G. and Carpinteri, A., Particle-based numerical modeling of AE statistics in disordered materials. *Magazine of Concrete Research*, 48(1), 211–220 (2013).

[132] Invernizzi S., Lacidogna G. and Carpinteri A., Numerical Models for the Assessment of Historical Masonry Structures and Materials, Monitored by Acoustic Emission. *Applied Sciences*, 6(4), 102 (2016).

[133] Carpinteri A., Lacidogna G., Corrado M. and Di Battista E., Cracking and crackling in concrete-like materials: A dynamic energy balance. *Engineering Fracture Mechanics*, 155, 130–144 (2016).

[134] Tang C., Numerical simulation of progressive rock failure and associated seismicity. *Int.*

J. Rock Mech. Min. Sci., 34(2), 249–261 (1997).

[135] Tang C.A., Kaiser P.K., Numerical simulation of cumulative damage and seismic energy release during brittle rock failurepart I: fundamentals. *Int. J. Rock Mech. Min. Sci.*, 35(2), 113–121 (1998).

[136] Andreykiv O.Y., Lysak M.V., Serhiyenko O.M., Skalsky V.R., Analysis of acoustic emission caused by internal cracks. *Eng. Fract. Mech.*, 68(11), 1317–1333 (2001).

[137] Andreykiv O., Skalsky V., Serhiyenko O., Rudavskyy D., Acoustic emission estimation of crack formation in aluminium alloys. *Eng. Fract. Mech.*, 77(5), 759–767 (1010).

[138] Nazarchuk Z., Skalskyi V. and Serhiyenko O., Acoustic Emission: Methodology and Application, *Springer* (2017).

[139] Bizzarri A., On the deterministic description of earthquakes. *Review of Geophysics*, 49, RG3002, doi:10.1029/2011RG000356 (2011).

[140] Barenblatt G., The formation of equilibrium cracks during brittle fracture, general ideas and hypotheses: Axially symmetric cracks. *Appl. Math. Mech.*, 23, 622–636 (1959).

[141] Fraldi M, Carotenuto A R, Cells competition in tumor growth poroelasticity. *Journal of the Mechanics and Physics of Solids*, 112(3), 345–367 (2018).

[142] Cao T. D., Hussain F., Schrefler B. A., Porous media fracturing dynamics: stepwise crack advancement and fluid pressure oscillations, *Journal of the Mechanics and Physics of Solids*, 111, 113–133 (2018).

Appendices

Appendix A

$$[M^e]^{11}_{IJ} = \int_{A_e} \rho(\boldsymbol{\psi}^1_I)^\top \boldsymbol{\psi}^1_J d\Omega, \quad [M^e]^{31}_{IJ} = \int_{A_e} \rho_f k_f (\boldsymbol{\psi}^3_I)^\top_{,x} \boldsymbol{\psi}^1_J d\Omega \tag{5.1}$$

$$[M^e]^{22}_{IJ} = \int_{A_e} \rho(\boldsymbol{\psi}^2_I)^\top \boldsymbol{\psi}^2_J d\Omega, \quad [M^e]^{32}_{IJ} = \int_{A_e} \rho_f k_f (\boldsymbol{\psi}^3_I)^\top_{,y} \boldsymbol{\psi}^2_J d\Omega \tag{5.2}$$

$$[K^e]^{11}_{IJ} = \int_{A_e} \Big(C_{11} (\boldsymbol{\psi}^1_I)^\top_{,x} (\boldsymbol{\psi}^1_J)_{,x} + C_{33} (\boldsymbol{\psi}^1_I)^\top_{,y} (\boldsymbol{\psi}^1_J)_{,y} \Big) d\Omega, \tag{5.3}$$

$$[K^e]^{12}_{IJ} = \int_{A_e} \Big(C_{12} (\boldsymbol{\psi}^1_I)^\top_{,x} (\boldsymbol{\psi}^2_J)_{,y} + C_{33} (\boldsymbol{\psi}^1_I)^\top_{,y} (\boldsymbol{\psi}^2_J)_{,x} \Big) d\Omega, \tag{5.4}$$

$$[K^e]^{13}_{IJ} = \int_{A_e} -\alpha_p (\boldsymbol{\psi}^1_I)^\top_{,x} (\boldsymbol{\psi}^3_J) d\Omega, \tag{5.5}$$

$$[K^e]^{21}_{IJ} = \int_{A_e} \Big(C_{21} (\boldsymbol{\psi}^2_I)^\top_{,y} (\boldsymbol{\psi}^1_J)_{,x} + C_{33} (\boldsymbol{\psi}^2_I)^\top_{,x} (\boldsymbol{\psi}^1_J)_{,y} \Big) d\Omega, \tag{5.6}$$

$$[K^e]^{22}_{IJ} = \int_{A_e} \Big(C_{22} (\boldsymbol{\psi}^2_I)^\top_{,y} (\boldsymbol{\psi}^2_J)_{,y} + C_{33} (\boldsymbol{\psi}^2_I)^\top_{,x} (\boldsymbol{\psi}^2_J)_{,x} \Big) d\Omega, \tag{5.7}$$

$$[K^e]^{23}_{IJ} = \int_{A_e} -\alpha_p (\boldsymbol{\psi}^2_I)^\top_{,y} (\boldsymbol{\psi}^3_J) d\Omega, \tag{5.8}$$

$$[K^e]^{33}_{IJ} = \int_{A_e} k_f \Big((\boldsymbol{\psi}^3_I)^\top_{,x} (\boldsymbol{\psi}^3_J)_{,x} + (\boldsymbol{\psi}^3_I)^\top_{,y} (\boldsymbol{\psi}^3_J)_{,y} \Big) d\Omega, \tag{5.9}$$

$$[C^e]^{31}_{IJ} = \int_{A_e} \alpha_p (\boldsymbol{\psi}^3_I)^\top (\boldsymbol{\psi}^1_J)_{,x} d\Omega, \tag{5.10}$$

$$[C^e]^{32}_{IJ} = \int_{A_e} \alpha_p (\boldsymbol{\psi}^3_I)^\top (\boldsymbol{\psi}^2_J)_{,y} d\Omega, \tag{5.11}$$

$$[C^e]^{33}_{IJ} = \int_{A_e} (\boldsymbol{\psi}^3_I)^\top (\boldsymbol{\psi}^3_J) \frac{1}{Q} d\Omega, \tag{5.12}$$

$$\mathbf{F}^e_{Iu_x} = \int_{A_e} \Big(\rho(b_x) (\boldsymbol{\psi}^1_I)^\top \Big) d\Omega + \int_{s^t_e} \Big(\bar{t}_x (\boldsymbol{\psi}^1_I)^\top \Big) d\Gamma_t + \int_{s^d_e} \Big(\bar{t}_{d_x} (\boldsymbol{\psi}^1_I)^\top \Big) d\Gamma_d, \tag{5.13}$$

$$\mathbf{F}^e_{Iu_y} = \int_{A_e} \Big(\rho(b_y) (\boldsymbol{\psi}^2_I)^\top \Big) d\Omega + \int_{s^t_e} \Big(\bar{t}_y (\boldsymbol{\psi}^2_I)^\top \Big) d\Gamma_t + \int_{s^d_e} \Big(\bar{t}_{d_y} (\boldsymbol{\psi}^2_I)^\top \Big) d\Gamma_d, \tag{5.14}$$

$$\mathbf{F}^e_{Ip} = \int_{A_e} k_f \rho_f \Big((\boldsymbol{\psi}^3_I)^\top_{,x} b_x + (\boldsymbol{\psi}^3_I)^\top_{,y} b_y \Big) d\Omega - \int_{s^w_e} \Big(\dot{w} \cdot n_{\Gamma w} (\boldsymbol{\psi}^3_I)^\top \Big) d\Gamma_w \tag{5.15}$$

in which e is either 1 or 2 for the superimposed elements one and two, respectively, and s^t_e, s^d_e, and s^w_e are the portions of superimposed element e on the traction boundary Γ_t, discontinuity surface Γ_d, and fluid flux boundary Γ_w, respectively. $\bar{t}_{d_x}$ and $\bar{t}_{d_y}$ are the components of contact tractions in x and y directions, respectively.